



AFRL-RX-WP-TP-2010-4148

**DAMAGE MECHANICS MODEL DEVELOPMENT FOR
MONOCRYSTALLINE SUPERALLOYS (PREPRINT)**

Mark A. Tschopp

Mississippi State University

FEBRUARY 2010

Approved for public release; distribution unlimited.

See additional restrictions described on inside pages

STINFO COPY

**AIR FORCE RESEARCH LABORATORY
MATERIALS AND MANUFACTURING DIRECTORATE
WRIGHT-PATTERSON AIR FORCE BASE, OH 45433-7750
AIR FORCE MATERIEL COMMAND
UNITED STATES AIR FORCE**

REPORT DOCUMENTATION PAGE				Form Approved OMB No. 0704-0188	
<p>The public reporting burden for this collection of information is estimated to average 1 hour per response, including the time for reviewing instructions, searching existing data sources, gathering and maintaining the data needed, and completing and reviewing the collection of information. Send comments regarding this burden estimate or any other aspect of this collection of information, including suggestions for reducing this burden, to Department of Defense, Washington Headquarters Services, Directorate for Information Operations and Reports (0704-0188), 1215 Jefferson Davis Highway, Suite 1204, Arlington, VA 22202-4302. Respondents should be aware that notwithstanding any other provision of law, no person shall be subject to any penalty for failing to comply with a collection of information if it does not display a currently valid OMB control number. PLEASE DO NOT RETURN YOUR FORM TO THE ABOVE ADDRESS.</p>					
1. REPORT DATE (DD-MM-YY) February 2010		2. REPORT TYPE Technical Paper Preprint		3. DATES COVERED (From - To) 01 August 2007 – 15 October 2009	
4. TITLE AND SUBTITLE DAMAGE MECHANICS MODEL DEVELOPMENT FOR MONOCRYSTALLINE SUPERALLOYS (PREPRINT)				5a. CONTRACT NUMBER FA8650-07-D-5800-0004	
				5b. GRANT NUMBER	
				5c. PROGRAM ELEMENT NUMBER 62102F	
6. AUTHOR(S) Mark A. Tschopp				5d. PROJECT NUMBER 4347	
				5e. TASK NUMBER RG	
				5f. WORK UNIT NUMBER M02R1000	
7. PERFORMING ORGANIZATION NAME(S) AND ADDRESS(ES) Mississippi State University Center for Advanced Vehicular Systems 200 Research Boulevard Starkville, MS 39759				8. PERFORMING ORGANIZATION REPORT NUMBER	
9. SPONSORING/MONITORING AGENCY NAME(S) AND ADDRESS(ES) Air Force Research Laboratory Materials and Manufacturing Directorate Wright-Patterson Air Force Base, OH 45433-7750 Air Force Materiel Command United States Air Force				10. SPONSORING/MONITORING AGENCY ACRONYM(S) AFRL/RXLMD	
				11. SPONSORING/MONITORING AGENCY REPORT NUMBER(S) AFRL-RX-WP-TP-2010-4148	
12. DISTRIBUTION/AVAILABILITY STATEMENT Approved for public release; distribution unlimited.					
13. SUPPLEMENTARY NOTES Technical paper for general release. PAO Case Number: 88ABW-2009-4645; Clearance Date: 04 Nov 2009. This work was funded in whole or in part by Department of the Air Force Contract FA8650-07-D-5800-0004. The U.S. Government has for itself and others acting on its behalf an unlimited, paid-up, nonexclusive, irrevocable worldwide license to use, modify, reproduce, release, perform, display, or disclose the work by or on behalf of the U.S. Government. Paper contains color.					
14. ABSTRACT This research in support of the Air Force Research Laboratory Materials and Manufacturing Directorate was conducted at Wright-Patterson AFB, Ohio from 1 August 2007 through 15 October 2009. The objective of this task was to develop methods to better predict damage initiation, such as cracking, in superalloys under engine representative conditions. This report details work that focuses on characterizing the material microstructure of single crystal nickel-based superalloys, which is important for damage initiation in these materials. Additionally, this report details work that involves in-situ mechanical testing of miniature specimens within the SEM as well as the setup of a miniature test specimen apparatus.					
15. SUBJECT TERMS mechanics, single crystal Ni-based superalloys, microstructure, characterization, image processing, digital image correlation					
16. SECURITY CLASSIFICATION OF:			17. LIMITATION OF ABSTRACT: SAR	18. NUMBER OF PAGES 90	19a. NAME OF RESPONSIBLE PERSON (Monitor) Christopher F. Woodward 19b. TELEPHONE NUMBER (Include Area Code) N/A
a. REPORT Unclassified	b. ABSTRACT Unclassified	c. THIS PAGE Unclassified			

1 Contract Summary

1.1 Objective

Develop a method to predict damage initiation, such as cracking, in superalloys under engine representative conditions.

1.2 Description of Work

The proposed research program shall formulate and develop damage mechanics models for monocrystalline turbine blade materials under engine representative conditions. Continuum mechanics models shall be developed to describe / predict cyclic deformation under a variety of isothermal and thermomechanical load spectra. These models shall specifically account for the multiple levels of microstructural constituents in this class of materials and their evolution. Later efforts shall focus on formulating criteria for the damage (crack) initiation in this class of materials.

Experimental techniques shall be used to aid model formulation and validation. Special emphasis shall be placed on characterizing materials that are extracted from new and retired turbine airfoils. Techniques shall be developed to test small samples having a cross sectional area ranging from 1 to 4 mm² with a gage length on the order of 10 mm. This technique shall allow characterization of the actual monotonic and cyclic behavior of the material in the critical, part-specific microstructural condition and assess changes in that material behavior after microstructural modification due to high temperature service. Initially isothermal conditions up to 1200°C shall be simulated with a goal of developing thermomechanical and thermal gradient test capabilities. Techniques shall be also developed to test actual turbine airfoil geometries, such as transpiration cooling holes and dead end ribs, to elucidate the interplay between the microstructure, its evolution and component geometry.

2 Introduction

High temperature mechanical behavior plays a crucial role in determining the total life of fracture critical turbine engine components. The Air Force Research Laboratory's Engine Rotor Life Extension and Materials Damage Prognosis programs have examined life-limiting factors in fatigue in an effort to extend the lives of service components. Various material-specific mechanisms contribute to fatigue variability and high temperature mechanical behavior. For example, in fatigue, fatigue variability has been associated with competing failure mechanisms in

Ti-6246, René 88DT and IN-100. The ability to predict high temperature mechanical behavior, fatigue variability, and the minimum life of critical components significantly affects the sustainability of an aircraft fleet.

To accurately predict high temperature mechanical behavior, it is vital to understand what the fatigue-critical microstructural features are and exactly how these may couple with loads and temperatures to nucleate damage in these critical components. This report focuses on two research areas critical to better understanding high temperature mechanical behavior in single crystal nickel-based superalloys, which are commonly used materials for turbine blades that lie within the hot section (1200°C) of the engine. The first research area detailed in this report is the high temperature mechanical properties (creep, fatigue) of single crystal nickel-based superalloys. The second research area detailed in this report is the detection and characterization of microstructural features that may be important for models that aim to describe how damage progresses in single crystal Ni-based superalloys. The ability to use the information stemming from these research areas in concurrent multiscale damage mechanics models may greatly enhance the engineering of single crystal Ni-based superalloys.

3 Results

This section contains multiple journal papers that comprise completed elements that relate to the mechanics of nickel-based superalloys and the characterization of key microstructural features that relate to high temperature creep and fatigue of these superalloys. Section 3.1 discusses digital image correlation of laser-ablated platinum nanoparticles on the surface of a polycrystalline metal (nickel-based superalloy René 88DT), which was used to obtain the local strain behavior from an *in situ* scanning electron microscope tensile experiment at room temperature. Section 3.2 discusses a methodology for automated detection and 3D characterization of eutectic particles taken from serial images of a production turbine blade made of a heat-treated single crystal Ni-based superalloy. Section 3.3 discusses a methodology for automated detection and 3D characterization of dendrite cores from images taken from slices of a production turbine blade made of a heat-treated single crystal Ni-based superalloy. The dendrite core locations are detected using an automated segmentation technique that exploits the four-fold symmetry of the dendrites when viewed down the $\langle 001 \rangle$ growth direction. Section 3.4 discusses a computational methodology for automated detection of secondary and tertiary γ' precipitates in EFTEM images. Section 3.5 discusses a technique used to assess the key microstructural length scales based on synthetic microstructures of varying area fraction, orientation, and aspect ratio. Last, Section 3.6 briefly discusses the setup of a tensile apparatus capable of testing miniature specimens at temperatures up to 1200°C.

These papers would not have come together if not for the help of numerous co-authors. I would like to acknowledge the following co-authors (their subsection contribution in parentheses): B.B. Bartha (3.1), S. Fairchild (3.1), W.J. Porter (3.1), P.T. Murray (3.1), M.A. Groeber (3.2, 3.3), J.P. Simmons (3.2, 3.3), A.H. Rosenberger (3.2, 3.3, 3.6), C. Woodward (3.2, 3.3), J.S. Tiley (3.4), G.B. Viswanathan (3.4), G.B. Wilks (3.5), and J.E. Spowart (3.5).

3.1. Microstructure-dependent local strain behavior in polycrystals through *in situ* scanning electron microscope tensile experiments

This subsection details digital image correlation of laser-ablated platinum nanoparticles on the surface of a polycrystalline metal (nickel-based superalloy René 88DT), which was used to obtain the local strain behavior from an *in situ* scanning electron microscope tensile experiment at room temperature. By fusing this information with crystallographic orientations from EBSD, a subsequent analysis shows that the average maximum shear strain tends to increase with increasing Schmid factor. Additionally, the range of the extreme values for the maximum shear strain also increases closer to the grain boundary, signifying that grain boundaries and triple junctions accumulate plasticity at strains just beyond yield in polycrystalline René 88DT. *In situ* experiments illuminating microstructure-property relationships of this ilk may be important for understanding damage nucleation in polycrystalline metals at high temperatures.

Fatigue variability plays a crucial role in determining the total life of fracture critical turbine engine components. The Air Force Research Laboratory's Engine Rotor Life Extension and Materials Damage Prognosis programs have examined life-limiting factors in an effort to extend the lives of service components. Various material-specific mechanisms contribute to fatigue variability (1). For example, fatigue variability has been associated with competing failure mechanisms in Ti-6246, René 88DT and IN-100 (2-4). The ability to predict fatigue variability and the minimum life of critical components significantly affects the sustainability of an aircraft fleet.

To accurately predict fatigue variability, it is vital to understand what the fatigue-critical microstructural features are and exactly how these may couple with loads and temperatures to nucleate damage in these critical components. It is a commonly held notion that damage nucleates in locations of large strain concentrations or where substantial inelastic deformation exists. Digital image correlation (DIC) is a technique often used to investigate how strain localizes around part geometric features, such as cracks, holes, and notches. Recently, this technique has been applied at increasingly smaller scales, *i.e.*, *in situ* scanning electron microscope (SEM) (5-8) and atomic force microscope (9-10) studies are now on the order of the underlying microstructural features. Similar *in situ* studies are also used to understand how microstructure evolves with deformation (*e.g.*, in Ti alloys 11-12). The ability to combine these studies and understand how specific microstructure features evolve and couple with local strains can greatly enhance our ability to predict fatigue and, perhaps, engineer better materials for fatigue.

In this subsection, we present an *in situ* SEM technique that can be used to obtain the local deformation behavior of polycrystalline materials at room and elevated temperatures. René 88DT, a forged polycrystalline Ni-based superalloy used in aircraft engine components, was chosen as a novel material for this work. The results correlate the local strain behavior obtained from DIC to grain boundaries and grain orientations using electron backscatter diffraction (EBSD). Ultimately, the objective of this research is to understand how the microstructural variability of polycrystalline materials influences fatigue variability. This subsection highlights a

novel methodology that couples local strains with crystallographic orientations to analyze microstructural factors that may influence damage nucleation and fatigue.

The experimental setup consisted of a screw-driven 1000 lb capacity tensile stage (Ernest F. Fullam, Inc.) placed inside a Quanta 600 FEG SEM. The tensile specimen was a flat dog bone-shaped specimen with gage dimensions of 2.794 mm wide x 0.720 mm thick x 10 mm long.

Digital image correlation often uses a speckle pattern to track displacements. Here, the specimen surface was coated with Pt nanoparticles (Figure 3.1.1) using a laser ablation process termed **through thin film ablation** (TTFA) (13). The specimen surfaces were mechanically polished to a 1 μm finish prior to deposition; a clean polished surface is essential for optimal imaging and deposition. The TTFA technique used a 10 nm Pt thin film deposited onto a fused silica plate transparent to the laser wavelength (wavelength = 248 nm, energy density = 0.5 J/cm²). The chamber was filled with Ar at a pressure of 5 torr. The laser irradiates the Pt thin film from the backside, propelling Pt nanoparticles at the intended target, *i.e.*, in this case, the tensile specimen. The high density of the Pt nanoparticles compared to the René 88DT provided sufficient contrast in the secondary electron images for DIC. The TTFA nanoparticles are deposited in a random speckle pattern that allows sub-pixel resolution of displacement. Platinum nanoparticles enable DIC at higher temperatures than Au patterns (*e.g.*, Ref. 5), *i.e.*, into the temperature range where nickel-based superalloys are typically used. Similar nanoparticle speckle patterns have also been applied to surfaces through spin-casting (14-15) or lithography techniques (16).

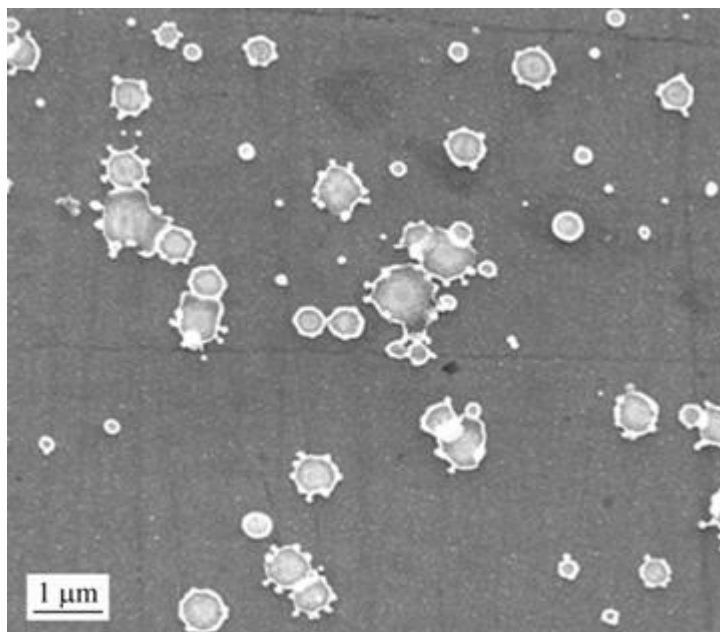


Figure 3.1.1. BSE images of nanoparticles on the surface of the tensile specimen.

The specimen was then mounted into the tensile stage grip fixture and preloaded to help align the specimen. Both secondary electron (SE) and backscatter electron (BSE) images were collected at 16 bit depth at a pixel resolution of 4096 by 3773 pixels. The SE images were used for digital image correlation while the BSE images provided sufficient detail for aligning the in-situ images with post-processed EBSD images. At each load step, the stage controller was turned off while acquiring the images to minimize any potential distortion effects due to the motor operating the stage. Each image was focused by adjusting the stage fixture to keep the same working distance; this minimizes any additional artifacts due to focusing with the beam only.

The tensile specimen was loaded in 12 steps to 1381 MPa (yield regime) with larger (smaller) step sizes in the elastic (plastic) regime. The present analysis was conducted at room temperature. After unloading the specimen, fiducial marks were applied through nanoindentation to identify the DIC region and the Pt nanoparticles were removed from the surface through a fine polishing step. Then, EBSD was used to measure the crystallographic orientations of the underlying microstructure. Digital Image Correlation was performed on each image with ViC-2D (Correlated Solutions, Inc.) to calculate the displacement field for each load increment. The image at the 0 MPa unloaded condition was used as a reference image for the displacement calculation. A subset size of 99 pixels was used for each calculation with a 5 pixel step size and cubic B-spline interpolation. The displacement maps were then converted to maximum shear strain maps for the remainder of the analysis.

Figure 3.1.2 shows the result of digital image correlation for a nominal stress of 1280 MPa. Fig. 2(a) shows the reference image, while Fig. 2(b) shows the deformed image with evidence of slip bands in some grains; the loading axis is horizontal. The digital image correlation software uses Fourier transforms of multiple subsets of these images to calculate the sub-pixel displacements and strains, as shown in Fig. 2(c). The average strain in the loading axis direction for the 274 μm by 230 μm region of interest is 0.02. The high strain concentrations are localized in bands oriented approximately 45 degrees from the tensile direction, as would be expected. The bands present in Fig. 2(c) do not necessarily correlate with the observed slip bands in Fig. 2(b); grain boundaries also play an important role in the high local maximum shear strain bands.

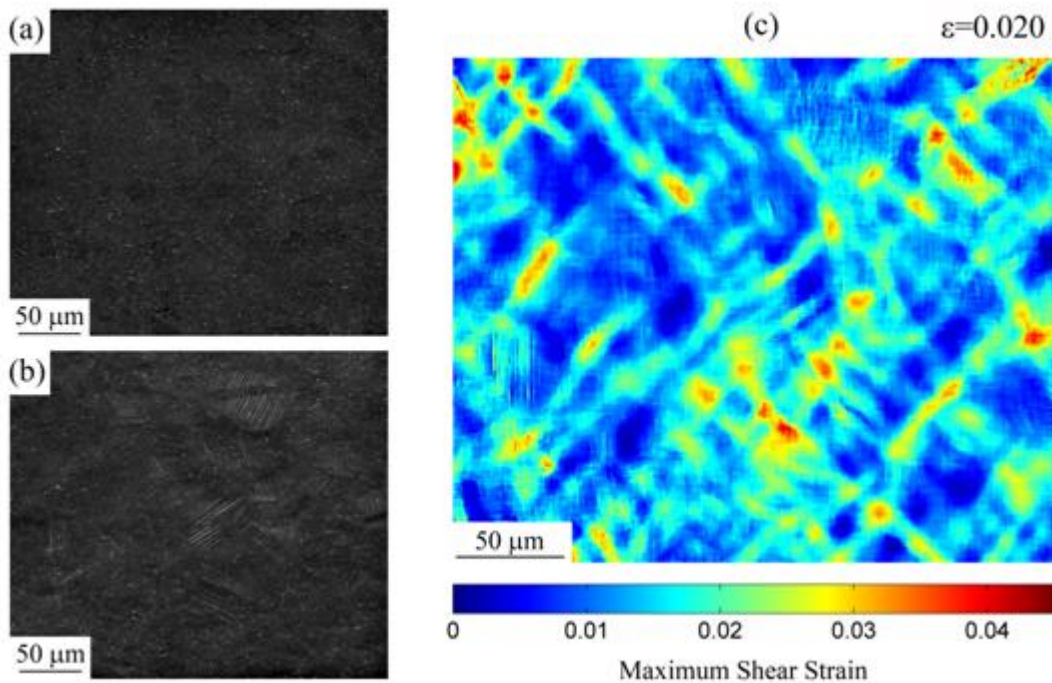


Figure 3.1.2. (a,b) SE images of René 88DT with nanoparticles (bright spots throughout image) at no load and after yield. (c) Digital image correlation was used to generate the maximum shear strains within the 274 μm by 230 μm region of interest.

Further analysis requires the maximum shear strain maps to overlap the crystallographic information obtained from the EBSD scan. By aligning the inverse pole figure in Figure 3.1.3(a) with the BSE image in Figure 3.1.3(b), the strain maps can be correlated with information obtained from crystal orientations, *e.g.*, Schmid factor, Taylor factor, etc. The image quality (IQ) map (Fig. 3c) is a quantitative measure of the fit of the Kikuchi pattern from the EBSD scan. The grain boundaries have a lower IQ value than the grain interiors, which allows for a better alignment with the BSE image. The IQ map image is then aligned with the BSE image through rotation, translation, and rescaling, as shown in Figure 3.1.3(d). However, the pixels and their spacing may still be different between the two datasets. Therefore, a nearest neighbor interpolation is used to match the pixels in the IQ map with the pixels in the BSE image. All subsequent analyses are related to correlating the shear strain behavior in Figure 3.1.2 with quantitative information relating to the crystallographic grain orientation.

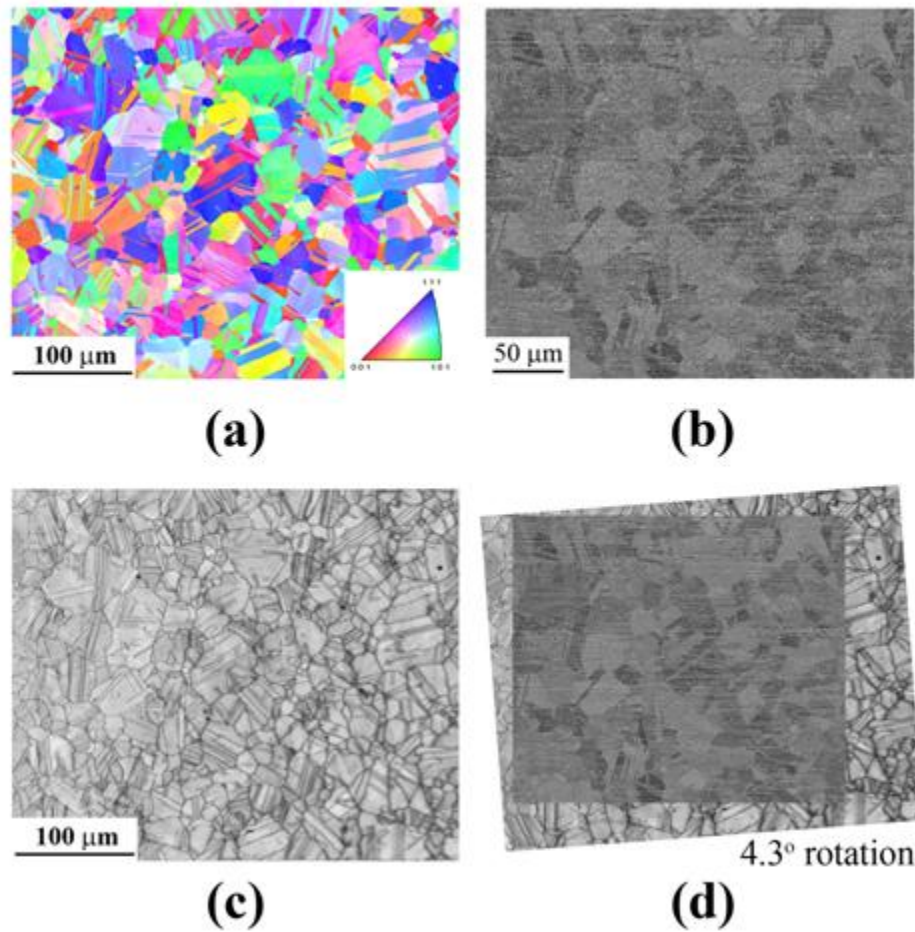


Figure 3.1.3. Image alignment process: (a) Inverse pole figure showing crystal orientations from EBSD scan, (b) BSE image of René 88DT prior to deformation, (c) IQ map of microstructure, and (d) aligned images.

Figure 3.1.4 shows the correlation between the Schmid factor and the maximum shear strain. Each data point represents 1 pixel from the strain map of Figure 3.1.2, *i.e.*, over 460,000 data points total. Figure 3.1.4(a) shows the distribution of Schmid factors within the René 88DT grain structure over the same area as Fig. 2(c). The Schmid factor resolves the tensile stress onto the $\{111\}$ slip plane in the $\langle 110 \rangle$ slip direction, *i.e.*, a higher Schmid factor should coincide with a higher shear stress in the direction of slip. Fig. 4(b) shows the relation between the maximum shear strain and the Schmid factor. At low Schmid factors, the range of the extreme values of maximum shear strain (*i.e.*, the low and high values) is not as large as for higher Schmid factors. There appears to be no decisive relationship between the Schmid factor and extreme values of the maximum shear strain, since high maximum shear strains are observed in regions with Schmid factors of approximately 0.35. The high extreme values of maximum shear strain are of particular interest because they indicate regions of damage accumulation, which is important

under fatigue conditions. The average maximum shear strain also shows a net increasing trend in maximum shear strain with increasing Schmid factor, although this trend is minimal.

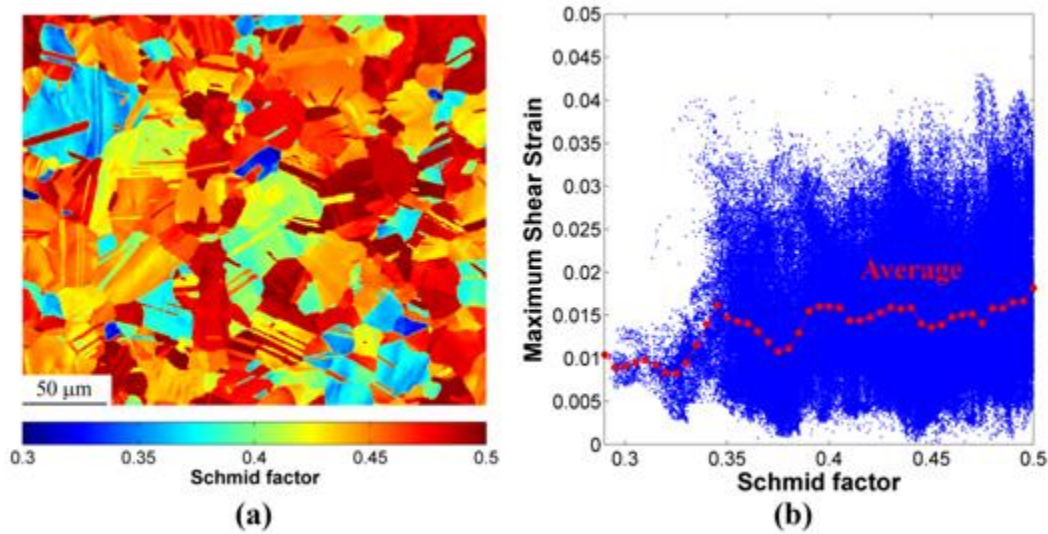


Figure 3.1.4. (a) Schmid factor map of the region of interest and (b) maximum shear strain vs. Schmid factor at a nominal stress of 1280 MPa.

The grain boundary network may also be associated with the localization in strain within the region of interest. Figure 3.1.5 shows the correlation between the distance from the grain boundary and the maximum shear strain. The grain boundary pixels were identified by determining if there were two or more grains present in adjacent pixels (4-neighborhood). Fig. 5(a) shows the maximum shear strain map with the grain boundary pixels in black. The distance from the boundary was calculated using a Euclidean distance transform. Interestingly, Fig. 5(b) shows that the upper (lower) extreme values for maximum shear strain decreases (increases) as the distance from the grain boundary increases. This indicates that the grain boundary has a greater propensity to accommodate strain than the grain interiors --- both lower and higher shear strains. The strain behavior at large distances (approximately 8 microns and greater) from the boundary is related to the few large grains within the region of interest. The strain behavior at intermediate distances from the GB encompasses a large number of grains, yet the strain range is not as large as at the boundary. The average shear strain behavior is equivalent for the first 6 μm from the boundary; the deviation at larger distances is affected by the few large grains. These results indicate that shear strains are much more likely to localize at high values at the grain boundary regions rather than the grain interiors.

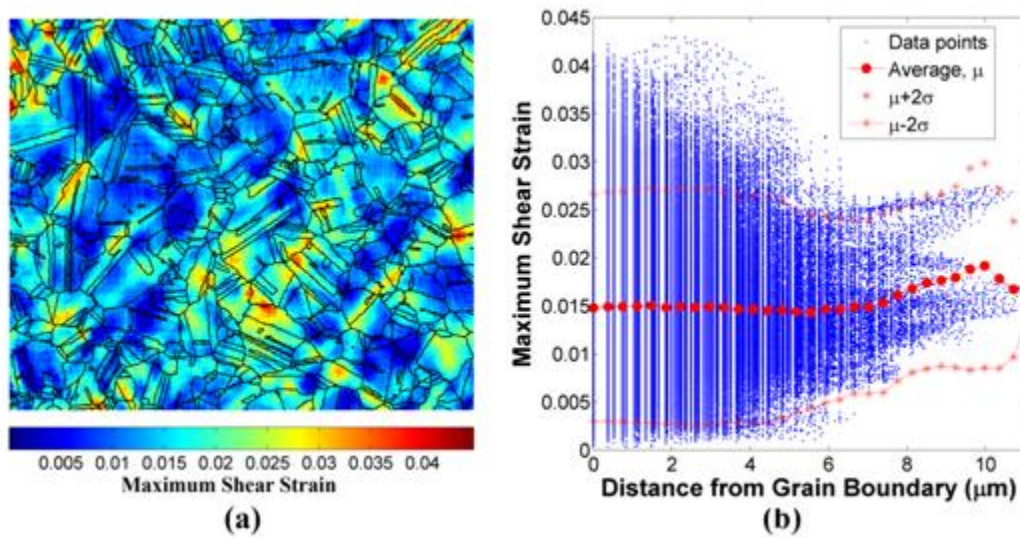


Figure 3.1.5. (a) Maximum shear strain map with the grain boundaries overlaid and (b) maximum shear strain with respect to distance from grain boundary.

These trends may not appear as strong because the strain localization after yield is not merely a function of the crystallographic orientation of the underlying lattice, but may also depend on the grain boundary structure, triple junctions, the grain size, and the neighboring grains, *i.e.*, due to multiple factor interactions. In this analysis, the trends apparent in Figs. 4 and 5 indicate that the factors examined in this subsection may be significant, though. Additionally, the maximum shear strains and grain orientations obtained are also a two-dimensional representation of a three-dimensional problem, which may further complicate correlating strains with the underlying microstructure. Ideally, having a specimen thickness on the order of the grain size may better elucidate some of these trends. In this work, however, the properties of interest correspond to Rene 88DT grain sizes analyzed. Last, OIM maps *after* deformation were used to supply the grain orientation information. Future work focuses on modifying this methodology to obtain EBSD crystallographic orientation *before* the in situ tensile experiment as well. This is important for high uniaxial strains, which could lead to grain rotation and grain boundary sliding at high temperatures.

In summary, this subsection presents a novel methodology for preparing tensile specimens for *in situ* SEM digital image correlation through a laser ablation process, through thin film ablation. By combining deformation strain maps from DIC with EBSD data, the correlation between the maximum shear strain and a number of microstructure-dependent parameters can be ascertained, *e.g.*, Schmid factor (Fig. 4) and distance from grain boundary (Fig. 5) in this analysis. On average, the maximum shear strain tends to increase with increasing Schmid factor. The range of the extreme values for the maximum shear strain also increases closer to the grain boundary, signifying that grain boundaries and triple junctions accumulate plasticity at strains just beyond yield within polycrystalline René 88DT.

This analysis shows that the strain localization in polycrystalline superalloys, which is important to plasticity, fatigue, and fracture, is a combination of a number of factors related to grain orientation and the grain boundary network. This will require coupling between further experiments and computational approaches to fully understand, and is vital to understanding how damage nucleates in fatigue-critical polycrystalline components. Furthermore, results of this ilk may also be used to estimate constitutive parameters with inverse computational methods based on full-field measurements (cf. 17-18). Future work aims to extend this approach to higher temperatures.

REFERENCES

- [1] S.K. Jha, M.J. Caton, J.M. Larsen, *MSE A* 468–470 (2007) 23–32.
- [2] S.K. Jha, M.J. Caton, J.M. Larsen, A.H. Rosenberger, K. Li, W.J. Porter, in: *Materials Damage Prognosis*, TMS publications (2004) 343-350
- [3] S.K. Jha, J.M. Larsen, A.H. Rosenberger, *JOM* Sept 2005 50-54.
- [4] S.K. Jha, M.J. Caton, J.M. Larsen, *Superalloys 2008*, 565-572.
- [5] M.A. Sutton, N. Li, D.C. Joy, A.P. Reynolds, X. Li, *Experimental Mech.* 47 (2007) 775-788.
- [6] M.A. Sutton, N. Li, D. Garcia, N. Cornille, J.J. Orteu, S.R. McNeill, H.W. Schreier, X. Li, A.P. Reynolds, *Experimental Mech.* 47 (2007) 789-804.
- [7] A. Soula, Y. Renollet, D. Boivin, J.L. Pouchou, D. Locq, P. Caron, Y. Bréchet, *Superalloys 2008*, 387-394.
- [8] J. Kang, Y. Ososkov, J.D. Embury, D.S. Wilkinson, *Scr Mater* 56 (2007) 999-1002.
- [9] W.G. Knauss, I. Chasiotis, Y. Huang, *Mech of Mater* 35 (2003) 217-231.
- [10] I. Chasiotis, W.G. Knauss, *Experimental Mech.* 42 (2002) 51-57.
- [11] C.J. Boehlert, C.J. Cowen, S. Tamirisakandala, D.J. McEldowney, D.B. Miracle, *Scripta Mat.* 55 (2006) 465-468.
- [12] C.J. Cowen, C.J. Boehlert, *Met Trans A* 38A (2007) 26-34.
- [13] P.T. Murray, E. Shin, *Mater. Lett.* 62 (2008) 4336-4338.
- [14] T.A. Berfield, J.K. Patel, R.G. Shimmin, P.V. Braun, J. Lambros, N.R. Sottos, *Small* 2 (2006) 631-635.
- [15] T.A. Berfield, J.K. Patel, R.G. Shimmin, P.V. Braun, J. Lambros, N.R. Sottos, *Experimental Mech.* 47 (2007) 51-62.
- [16] W.A. Scrivens, Y. Luo, M.A. Sutton, S.A. Collette, M.L. Myrick, P. Miney, P.E. Colavita, A.P. Reynolds, X. Li, *Experimental Mech.* 47 (2007) 63-77.
- [17] S. Avril, M. Bonnet, A.S. Bretelle, M. Grédiac, F. Hild, P. Ienny, F. Latourte, D. Lemosse, S. Pagano, E. Pagnacco, F. Pierron, *Experimental Mechanics* 48 (2008) 381-402.
- [18] T. Hoc, J. Crépin, L. Gélébart, A. Zaoui, *Acta Mater* 51 (2003) 5477-5488.

3.2. Automated Detection and 3D Characterization of Eutectic Particles in Single Crystal Ni-Based Superalloys

Serial sectioning methods continue to produce an abundant amount of image data used to quantify the three-dimensional nature of material microstructures. In this section, we discuss a methodology for automated detection and 3D characterization of eutectic particles taken from serial images of a production turbine blade made of a heat-treated single crystal Ni-based superalloy. This method includes two important steps for unassisted eutectic particle characterization: automated identification of the seed point within each particle and a region growing algorithm with an automated stop point. Once detected, the segmented eutectic particles are used to calculate microstructural statistics for characterizing and reconstructing statistically-representative synthetic microstructures for single crystal Ni-based superalloys. The significance of this work is its ability to automate characterization for analyzing the 3D nature of eutectic particles.

INTRODUCTION

Knowledge of the three-dimensional (3D) nature of particles may be important for ascertaining certain properties in many material systems. Serial sectioning is often a labor-intensive, but effective, tool that is used to provide datasets essential for characterizing three-dimensional (3D) microstructure. The ability to automate the removal of material at controlled rates through either mechanical polishing [1-3], microtome milling, or focused ion beam milling [4-8], has enabled researchers to obtain 3D microstructure datasets at a range of length scales. To further enhance the speed of collecting these datasets, the method of removal is often coupled with the imaging instrument, *e.g.*, mechanical polishing with optical imaging [1], or FIB with EBSD imaging [4-7]. This technique has helped to produce the 3D microstructure in a number of materials, *e.g.*,

- the polycrystalline grain structure in Ni-based superalloys (IN100) [5]
- the dendritic structure in single crystal nickel-based superalloys [9, 10], Al-Cu alloys [11, 12], and Pb-Sn alloys [13, 14]
- reinforcement particle for particle-reinforced metal-matrix composites [15, 16]
- microstructure (cementite, ferrite, austenite, martensite, and pearlite) colonies in alloy steels [17-20]
- the structure of pitch-based carbon foams [21]
- the γ - γ' microstructure in Ni alloys [4, 22, 23]
- intermetallic particles in Sn-rich solder [24]
- pore morphology in die-cast magnesium alloys [25]

In this work, the 3D structure of eutectic particles in single crystal nickel-based superalloy turbine blade casting is investigated. Large montage images from the airfoil section were used to obtain the 3D structure of eutectic particles. Parallel work concentrates on identifying dendrite cores to reconstruct the three-dimensional dendritic structure of the blade [26]. Identifying both

of these features is important for obtaining a quantitative description of the structure of single crystal nickel-based superalloys used in turbine blade applications.

Successful efforts to automate serial sectioning techniques to produce large sets of microstructure images [1, 2, 9, 10] have led to overwhelming amounts of data resulting in a bottleneck at the image processing and analysis step. This statement is particularly true for the image segmentation step in complex multi-component microstructures, *e.g.*, the eutectic particles, pores, carbides, and dendrites in the single crystal microstructure investigated here. Manual identification of the large number of eutectic particles and pores in single crystal nickel-based superalloys is impractical. Automating the identification and reconstruction of microstructural features will be required for this approach to reach its full potential. Reliable assessment of microstructural statistics will require processing large datasets.

The rapid growth in 3D microstructure characterization is driven by the requirements of integrated computational models that link processing to properties and performance. From a properties perspective, 3D microstructure statistics can enhance the predictive capability of finite element models that take microstructure into account. Reconstructing the microstructure at the relevant length scale(s) for high temperature mechanical behavior can be used in concurrent multi-scale FE models that account for material microstructure. For instance, Ghosh and coworkers [27] have developed a concurrent multi-level model whereby multiple levels of refinement are used to simulate crack growth behavior. The level zero continuum approximation corresponds to a constitutive response consistent with a homogenization of microstructure and properties over the entire domain of the turbine blade. Level one would capture the variation in response produced by crystal rotations of different dendritic domains, and the density of primary dendrites (primary dendrite arm spacing). Finer details in the microstructure such as the secondary arm spacing, eutectic phase, carbide and void distribution would be captured in a level two representation. One objective of this research is to measure the statistics necessary to generate statistically representative volume elements for inclusion in these models.

In this subsection, we present an *automated* technique for detecting eutectic particles in optical microscopy montages on serial-sections through a turbine blade airfoil. First, the acquisition process for these images is described. Second, the technique used to identify the eutectic particles is described, which includes identifying seed points for a region growing algorithm with an automated stopping criterion. Third, this automated technique is used for a series of sixteen slices from a blade to measure a set of microstructure descriptor statistics. Ultimately, the objective of this research is to automate the technique used for identifying eutectic particles and to calculate the microstructure statistics.

IMAGE ACQUISITION:

Figure 3.2.1 shows an etched optical image montage for a slice perpendicular to the nominal growth direction of a single crystal nickel-based superalloy (PWA 1484) turbine blade. The turbine blade was filet cut through the interior cooling passage, *i.e.*, the lower blade geometry reflects ribs in the interior cooling passages and the upper blade geometry is the exterior surface. Further details of the experimental method for obtaining the images are given in Groeber *et al.*

[28]. The pixel spacing is approximately 2 μm per pixel. The red box delineates a 3000 x 3000 pixel ($\sim 36 \text{ mm}^2$) subset of the turbine blade that is used for eutectic particle statistics later.

There are several problems associated with manual or standard image processing methods to segment eutectic particles from these images.

1. The large size (17544 x 4244 pixels, *i.e.*, 35 mm x 8 mm) of the images and the large number of eutectic particles make it difficult to segment eutectic particles manually.
2. The etchant used to highlight dendrite cores may etch material at different rates within the same slice, varying the contrast in intensity for different areas. Occasionally, the image contrast may change slightly from stitching images together for the image montage as well. Standard methods for leveling the contrast within the blade region to correct this do not account for the mount material, which would incorrectly skew intensity values near the edges of the blade.
3. Simple threshold methods for segmenting eutectic particles do not work well. First, segmenting the particles with a global threshold parameter applied to the entire image is adversely affected by the intensity contrast differences due to the etchant. Second, the dendrites (in particular, the dendrite core regions) have similar intensities to the eutectic particles of interest.

Therefore, an automated technique for processing these large images is required to address these problems. A standard region growing technique was augmented to segment eutectic particles in a single crystal nickel-based superalloy microstructure in an automated manner.

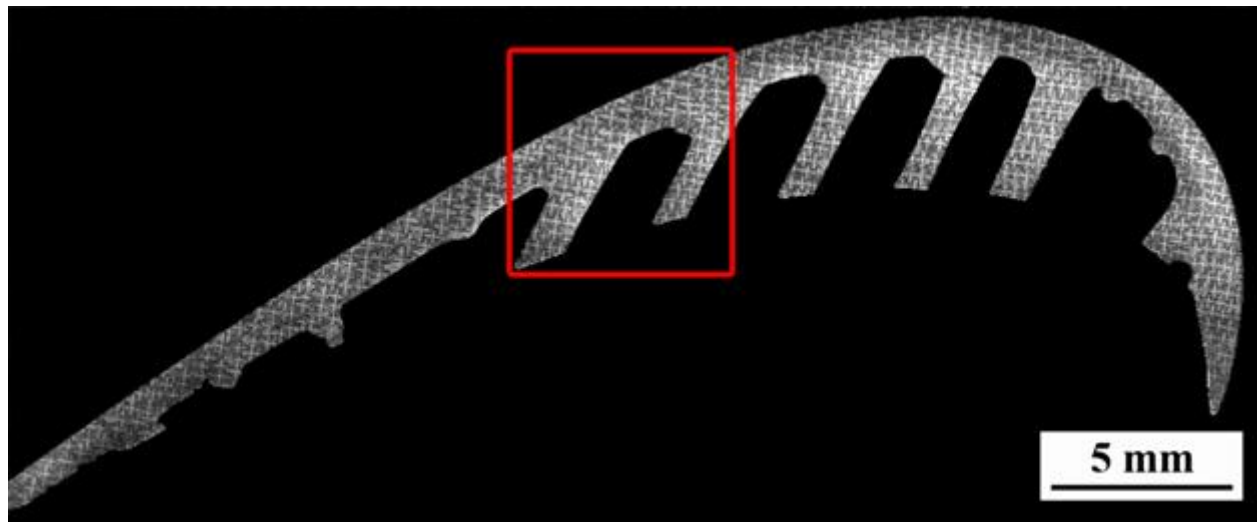


Figure 3.2.1. This image montage shows the microstructure of a cross-section of a single crystal nickel-based superalloy turbine blade embedded in mount material (in black).

AUTOMATED REGION GROWING TECHNIQUE FOR EUTECTIC PARTICLE IDENTIFICATION

A typical region growing technique works by selecting a seed point within a region (*e.g.*, a precipitate), growing the region by iteratively adding the neighboring pixel with the closest intensity value to the average intensity of the region, and stopping growth of the region when the neighboring pixel with the closest intensity value exceeds a threshold parameter for the intensity difference. This standard method can be used to segment the eutectic particles. The difficulty with this technique is that it requires the user to specify the seed point from which to start growing and it requires a user-specified threshold parameter, which may be different for different particles. The following pages describe how these steps were augmented to automate the eutectic particle detection.

Seed Point Detection

The first step required for automating the region growing technique to detect eutectic particles is to identify seed points within each eutectic particle. Figure 3.2.2 shows images at various stages of the seed point detection algorithm. Figure 3.2.2(a) shows the microstructure a 500- μm by 500- μm etched optical image taken from a turbine blade slice. Starting with this microstructure image, detecting the seed points requires a series of image processing steps, *i.e.*,

1. An edge detection filter, the Sobel filter, is cross-correlated with the original image. The absolute value of the resulting image shows the magnitude of the intensity gradients for each pixel in both the vertical (Figure 3.2.2(b)) and the horizontal directions (Figure 3.2.2(c)).
2. These two images are then multiplied ($A_{ij} = B_{ij} * C_{ij}$) to produce an image (Figure 3.2.2(d)) that further accentuates the eutectic particle boundary, while minimizing intensity gradients due to noise in the dendritic or interdendritic areas. At this point, the image's intensity is a double integer and was rescaled to an 8-bit image.
3. A threshold parameter of 50 was used to identify particle edges with high intensity gradients (Figure 3.2.2(e)). The boundaries of the eutectic particles are incomplete, showing the difficulty of methods that attempt to segment the boundary for identifying particles.
4. For each segmented boundary pixel, the neighboring pixel (8 pixel connectivity) with the highest intensity value is selected as a seed point for region growing. Figure 3.2.2(f) shows the original image with seed points in red. Notice that this technique defines at least one seed point within each eutectic particle and multiple seed points in the larger particles.

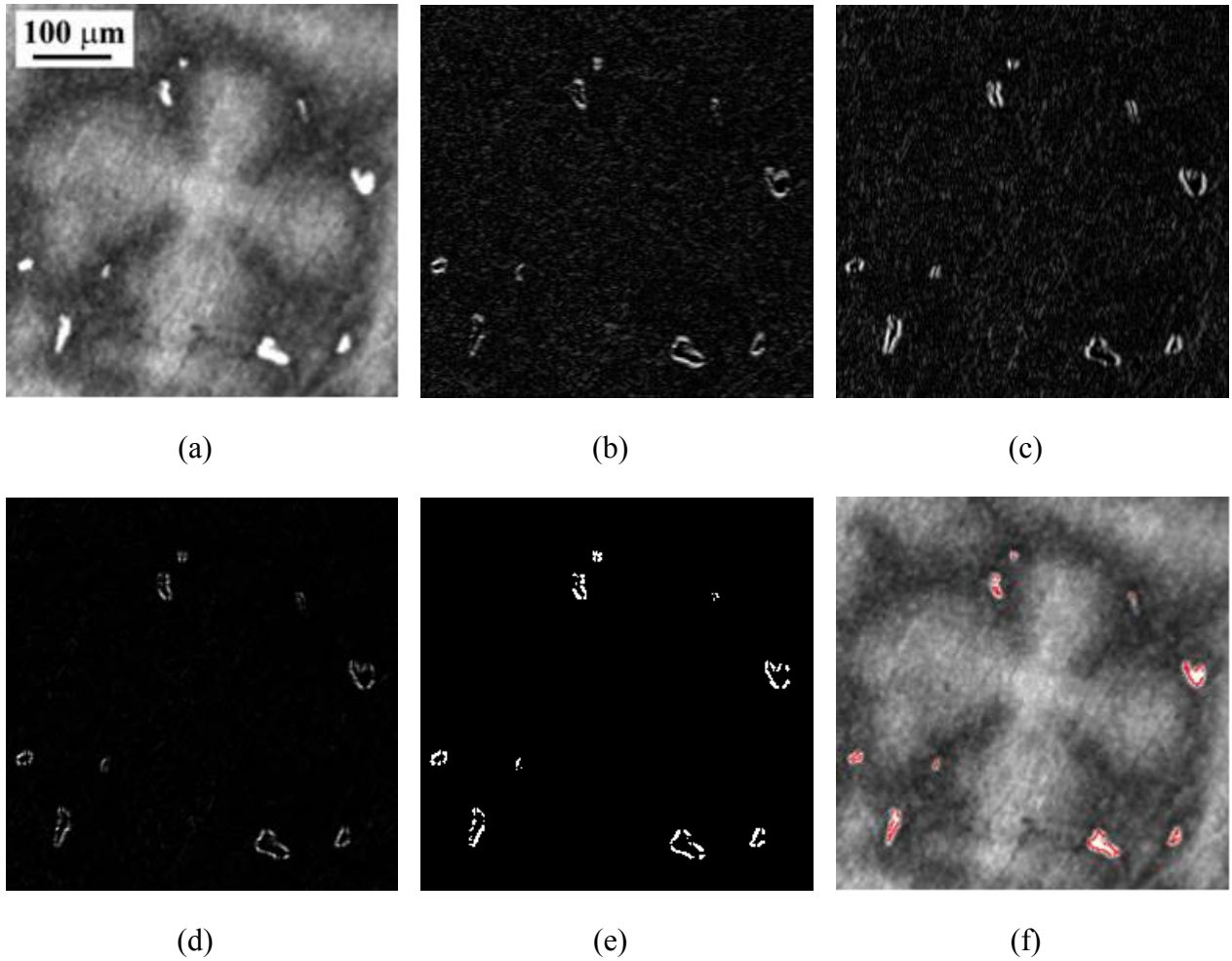


Figure 3.2.2. This series of images illustrates the various steps required in the seed point detection algorithm. (a) Original image, (b,c) Sobel edge detection filter in vertical direction (b) and horizontal (c) directions, (d) multiplication of Sobel edge detection images (b, c), (e) segmented seed points using threshold parameter of 50, and (f) seed point locations (red) superimposed on the original image.

This technique was repeated on the 3000 x 3000 pixel microstructural regions with good results. The threshold parameter for generating the particle edges can be optimized to minimize the amount of time devoted to the manual identification of incorrectly identified particles and undetected eutectic particles. In this work, the threshold parameter of 50 minimized the incorrectly identified particles associated with scratches and dendritic areas, leaving the user to mainly identify seed points for undetected eutectic particles manually (<10% of identified particles).

Automated stopping feature

Second, to eliminate the necessity of a user-specified threshold parameter for a stopping criterion, we automated the stopping feature of a typical region growing algorithm. To accomplish this, the threshold parameter for the region growing algorithm is incrementally increased and a penalty function is calculated for each threshold parameter. In this case, the penalty function is the difference between the mean intensity of the region and the mean intensity of the neighboring pixels just outside the region. The threshold parameter that optimizes the intensity difference is the critical threshold parameter for segmenting the eutectic particle. The advantage of this method over a global user-specified threshold parameter is that this method will change the threshold parameter to maximize the intensity difference in *each* particle. Therefore, this method can account for any changes in intensity with the eutectic particles and the surrounding interdendritic area.

Figure 3.2.3(a) shows the region pixel size as a function of the `_stopping` threshold parameter chosen for a seed point along a large eutectic particle. For small threshold parameters, the region is contained within the boundary region of the eutectic particle as shown in the accompanying image. The abrupt increase in the region size at an intensity threshold of 54 corresponds to the region growing into the eutectic particle. After this point, increases in the intensity threshold result in only minor increases to the region size. This is the difficulty with choosing a threshold parameter based on visual observation. With only minimal changes to the region size for higher threshold parameters, at what threshold is the particle accurately segmented?

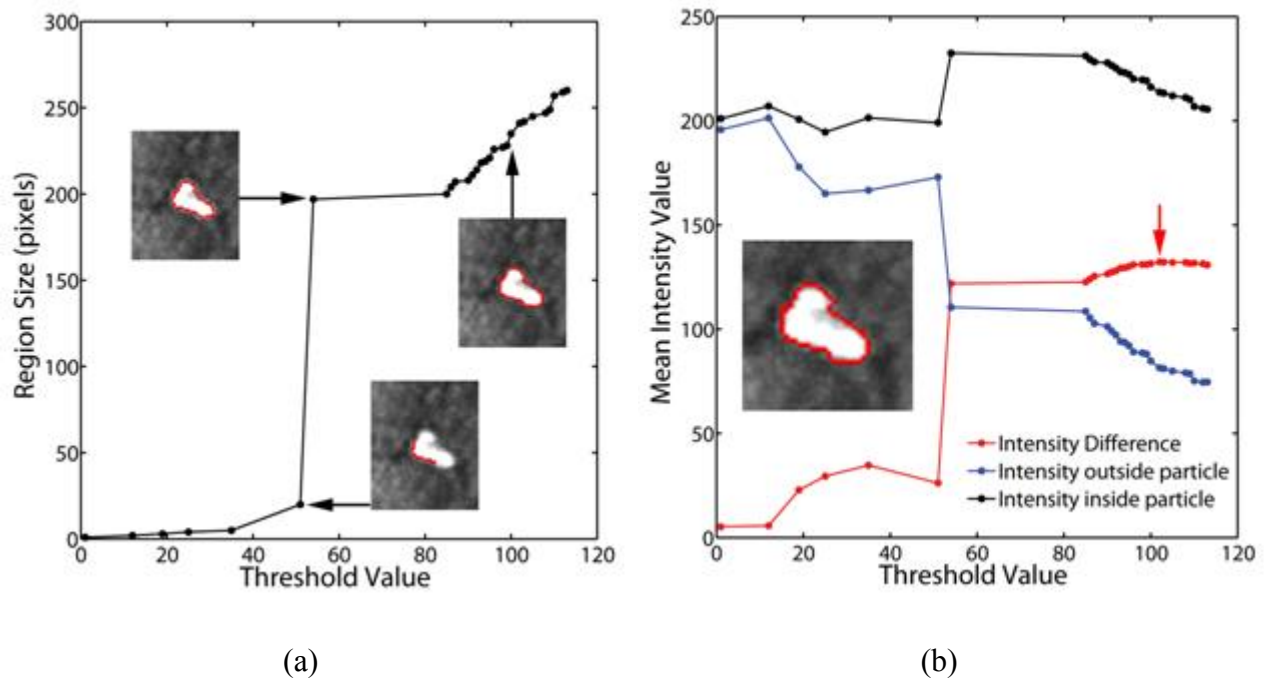


Figure 3.2.3. (a) Plot showing the region size as a function of the stopping threshold value. (b) Plot showing the mean intensity for the region, the area just outside the region, and the intensity difference between the two areas as a function of the stopping threshold value. The arrow and

image correspond to the region with the maximum intensity difference, which is used for the automated region growing stopping criterion.

To answer this question, Figure 3.2.3(b) shows the mean intensity of the region, the mean intensity of the neighboring pixels, and the intensity difference between these two areas as a function of the threshold parameter for the same eutectic particle. Recall that the maximum intensity difference (red) is used here for the automated stopping criterion for the region growing technique. For small threshold parameters, the seed point's intensity is much lower than the remainder of the eutectic particle. This is due to selecting a seed point near the boundary of the particle, instead of at the interior of the particle. At this point, the intensity of the area outside the region is approximately equivalent to the intensity of the area inside the region, *i.e.*, many of the pixels outside the region also lie within the eutectic particle. Again, the abrupt increase in the intensity difference at an intensity threshold of 54 is due to the region growing into the eutectic particle, as shown in Figure 3.2.3(a). The optimum segmentation of the eutectic particle is defined as the threshold parameter that yields the maximum intensity difference between these two areas, as denoted by the red arrow. The routine quantitatively identifies the eutectic particle boundary in an automated manner based on the intensity gradient across the interface. The image in Figure 3.2.3(b) shows the original image with the perimeter pixels for the segmented eutectic particle in red. Visual observation of various microstructural areas throughout the turbine blade (*e.g.*, Figure 3.2.4) confirms that the automated segmentation is satisfactory.

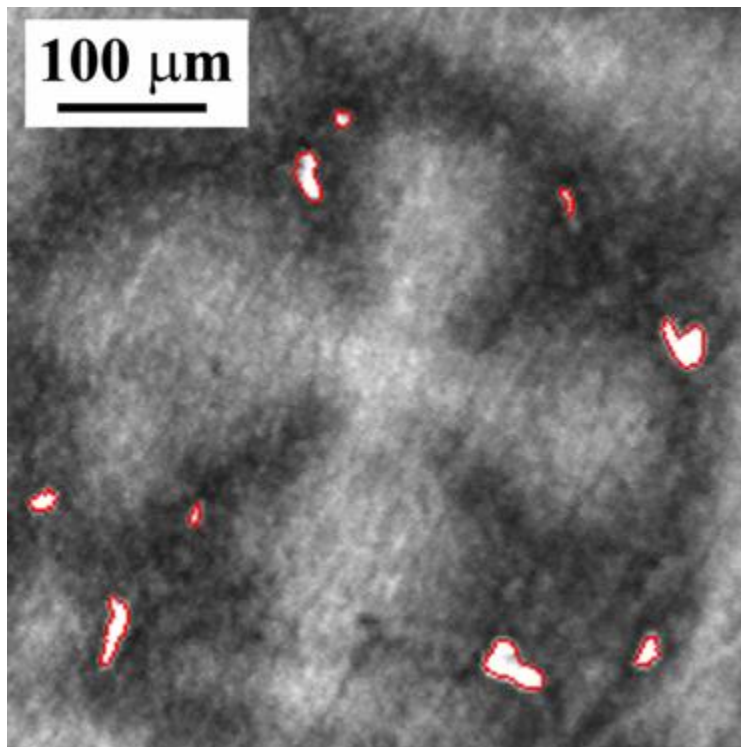


Figure 3.2.4. The perimeter of the segmented eutectic particles (red) is superimposed on the original image to show the visual agreement of the region growing algorithm.

While the objective of this work was to entirely automate the eutectic particle detection, there were still complications due to the mount material and scratches produced during the polishing process. Both the mount material and scratches can also cause problems with identifying seed points for the region growing technique. To remove the influence of the mount, the mount region was segmented manually using a combination of operations: thresholds, size filters, and morphological open/close operations. Seed points within 25 pixels ($\sim 50\text{ }\mu\text{m}$) of the mount material were removed. Visual observation was performed to identify regions that were incorrectly grown due to the mount material and scratches; these were manually removed prior to calculating microstructure statistics.

Eutectic particle statistics from a serial image was tracked to quantitatively assess the degree of manual post-processing for removing incorrect particles and adding unidentified eutectic particles. After removing particles with areas of 5 pixels or less ($20\text{ }\mu\text{m}^2$), the following technique identified 231 particles, of which 1 was manually removed (*i.e.*, 0.4% of initial particle count), and 8 particles were manually added (3.5%). These added particles tended to be small, though, with sizes just above the particle size threshold. As an additional step to insure correct segmentation of the eutectic particles, the maximum intensity of each of the correctly identified regions was used for a new seed point and the eutectic particles were grown again. Previous work using an automated region growing technique for γ' precipitate segmentation [29] has shown that seed points near the interface may lead to slightly different segmentation than interior seed points. However, this added step only decreased the average eutectic particle area by 0.3%. Afterwards, a final inspection of the segmented eutectic microstructure was performed with only a few small particles identified for addition.

MICROSTRUCTURAL STATISTICS OF EUTECTIC PARTICLES

The eutectic particles were segmented on sixteen successive slices spaced approximately $10\text{ }\mu\text{m}$ apart in the cropped section of the turbine blade image montage shown in Figure 3.2.1. The images on successive slices were roughly aligned; after the particles were identified, the sections were aligned using a cross-correlation technique that accounted for both translation and rotation.

2D statistics

Figure 3.2.5 shows the distribution of eutectic particle statistics for the sixteen slices. Figure 3.2.5(a) shows a histogram of the 2D size distribution for 3836 eutectic particles. Figure 3.2.5(b) shows a histogram of the 2D major axis length for these same eutectic particles. The major axis length is a scalar value that is equal to the length of the major axis of the ellipse that has the same normalized second central moments as the eutectic particle [30]. On average, eutectic particles on 2D slices aligned perpendicular to the nominal growth direction have a major axis length of $23\text{ }\mu\text{m}$ with an average particle area of $208\text{ }\mu\text{m}^2$. Perhaps just as important for fatigue considerations are the extreme value statistics of the eutectic particles, *i.e.*, the maximum major axis length was $120\text{ }\mu\text{m}$ and the maximum particle area was $1500\text{ }\mu\text{m}^2$.

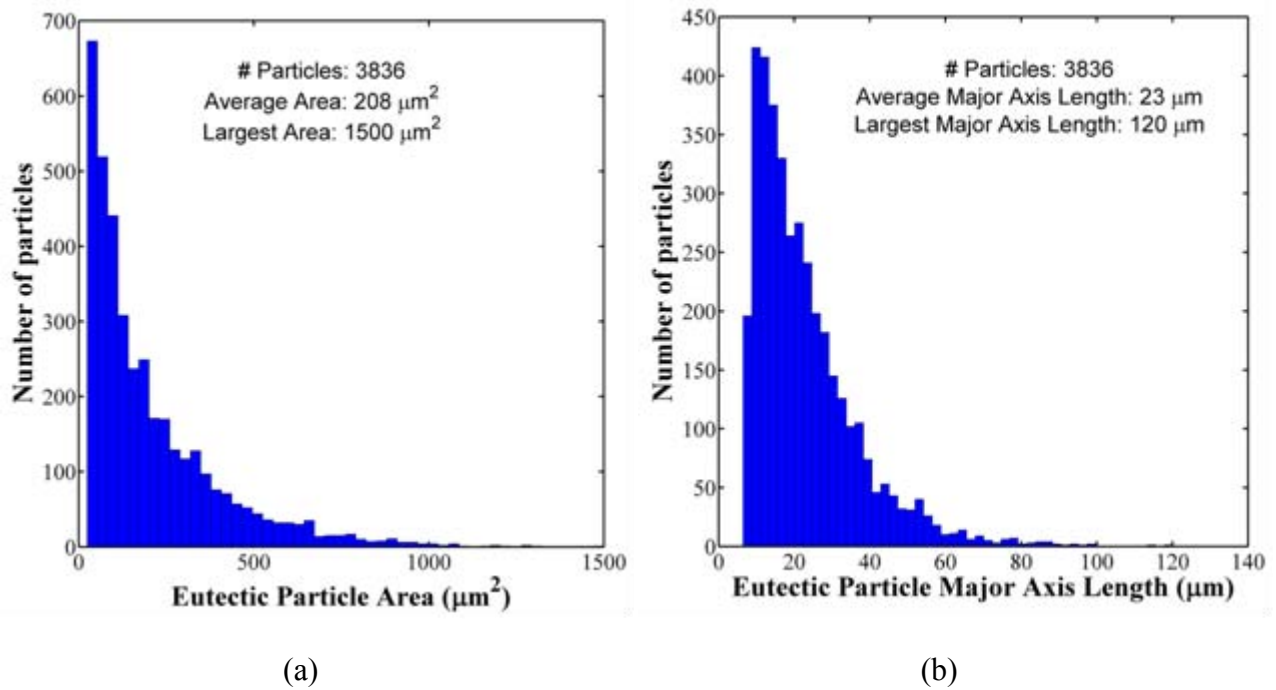


Figure 3.2.5. Histograms showing the (a) size distribution and (b) major axis length distribution for the 3836 eutectic particles on the 2D slices.

Figure 3.2.6(a) shows the nearest neighbor distance distribution for the eutectic particles on the 2D slices. The nearest neighbor distance is based on the centroid coordinates for each eutectic particle. As with the particle statistics, the nearest neighbor distance is calculated for each particle in each slice and the data from the separate slices are combined, *i.e.*, this distance does not incorporate particles from adjacent slices. Figure 3.2.6(b) normalizes the nearest neighbor distance by the equivalent particle diameter. On average, the nearest eutectic particle is approximately $132 \mu\text{m}$, or 8 times the equivalent particle diameter, away.

Eutectic particles near the surface of the blade may help initiate cracks within Ni-based superalloys. Relative occurrence at the free surface compared to that in the interior may change due to the presence of temperature gradients during solidification near the free surfaces (*i.e.*, cast walls). Figure 3.2.7 shows the two-point correlation function between the free surface (FS) of the cast turbine blade and eutectic particle pixels (E) as a function of distance from the surface (d). First, the Euclidean distance between each microstructure pixel and the mount material is calculated. The distances are divided into bins spaced approximately $50 \mu\text{m}$ apart. Then, the total number of eutectic and microstructure pixels is summed in each bin to give the probability of a eutectic pixel lying within a certain distance from the cast surface. This plot shows that for the data collected there is seemingly no correlation between the cast surface and the occurrence of eutectic particles. For reconstructing microstructures, this allows the microstructure to be constructed without needing to account for the effect at free surfaces, *i.e.*, a bulk 3D microstructure can be generated and trimmed to the blade geometry.

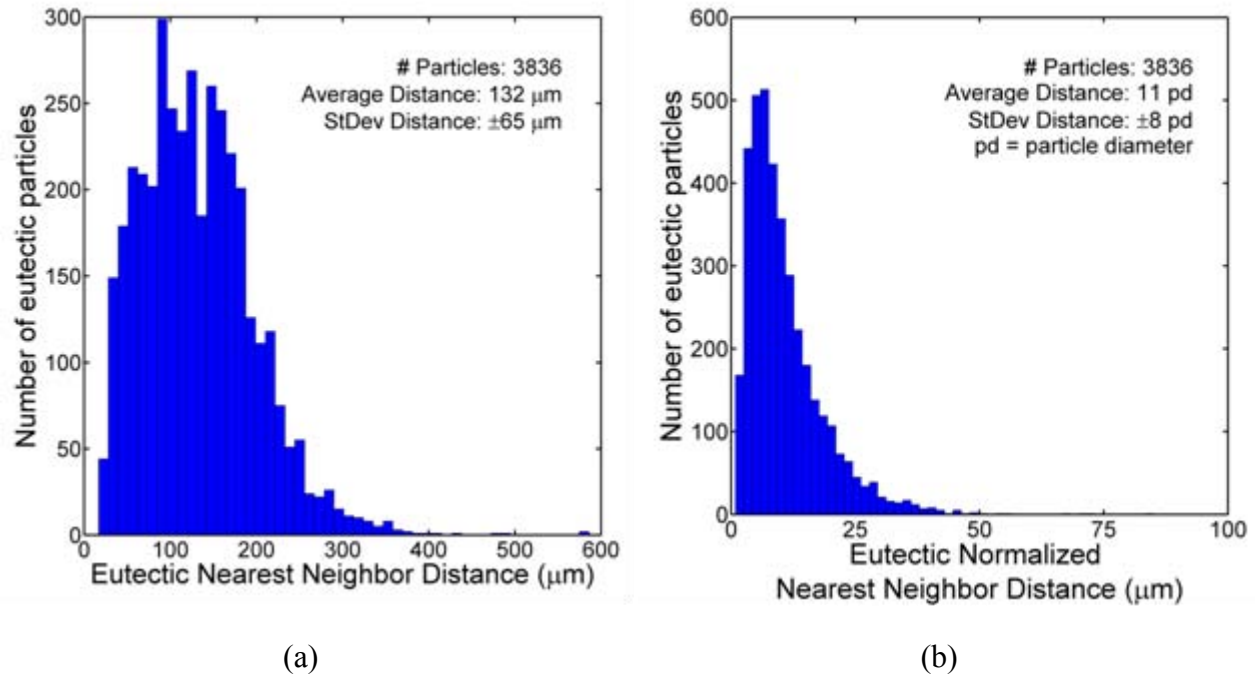


Figure 3.2.6. (a) Histogram showing the nearest neighbor distance distribution for the 3836 eutectic particles on the 2D slices. (b) Histogram showing the nearest neighbor distance normalized by the size of the eutectic particle, *i.e.*, the average distance between eutectic particles is 11 times the particle equivalent diameter.

The eutectic particles' 2D statistics on successive slices can also be useful for examining the slice-to-slice variability. Table 3.2.1 summarizes the variability in eutectic particle statistics from slice-to-slice in order of increasing coefficient of variation, *i.e.*, the standard deviation normalized by the mean of each statistic. The values in this table are found by first calculating the statistics for each slice and then applying the various operations to that data, *i.e.*, the average particle size was calculated for all sixteen slices and then the average of those sixteen values was inserted in the column Average. The statistics with the highest variability are the extreme value statistics, such as the maximum particle size or maximum major axis length of the particles in each slice. This trend is shown visually in Figure 3.2.8. Figure 3.2.8 is a 3D histogram plot of the probability distribution function for the eutectic particle sizes as a function of increasing slice number (each neighboring slice is separated by 10 μm). The extreme values of the eutectic particle sizes show noticeable change, while the PDF distribution (and its corresponding mean value) does not change as much. The large variability in the extreme value statistics, which may be important for high temperature mechanical properties such as high cycle fatigue [31].

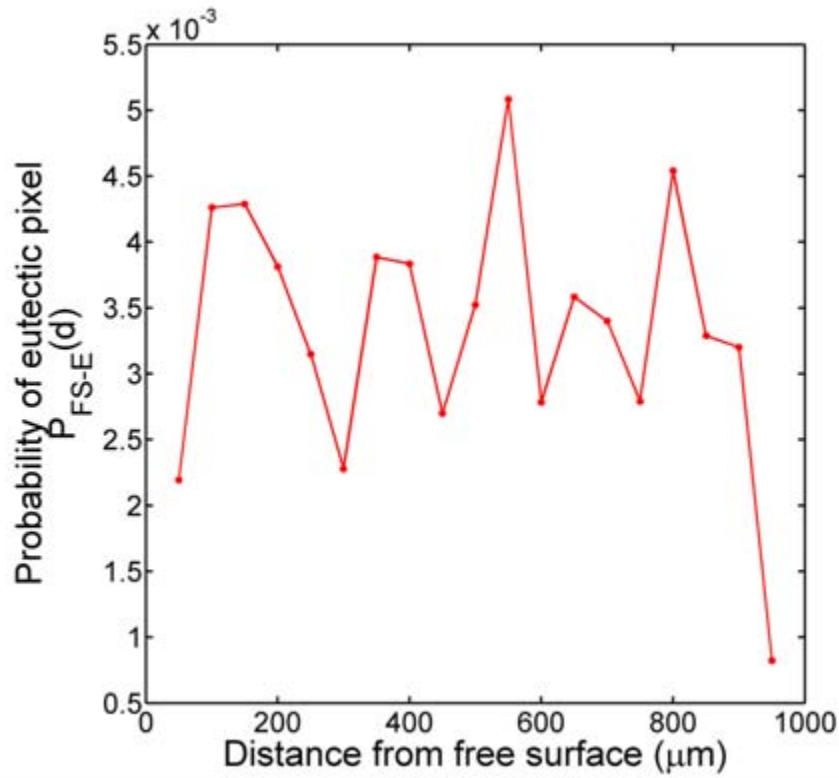


Figure 3.2.7. Graph showing the two-point correlation between the free surface (FS) and eutectic particles (E) as a function of distance from the surface (d).

Table 3.2.1. Slice to slice variation in eutectic particle 2D statistics based on sixteen successive slices spaced approximately 10 μm apart.

<i>Eutectic Particle 2D Statistic</i>	<i>Coefficient of Variation</i>	<i>Average</i>	<i>Standard Deviation</i>	<i>Maximum Value</i>
NND ¹ (μm)	0.0519	131.98	6.85	146.25
Average Major Axis Length (μm)	0.0522	22.93	1.20	24.78
Normalized NND ¹	0.0769	10.86	0.84	12.90
Average Particle Area (μm ²)	0.0849	207.41	17.60	230.3
Number of Particles	0.0917	239.75	21.99	272
Area fraction (%)	0.1399	0.34%	0.05%	0.42%
Maximum Particle Area (μm ²)	0.1416	1107.5	156.9	1500
Maximum Major Axis Length (μm)	0.1574	90.47	14.24	120.13

¹ NND is the nearest neighbour distance

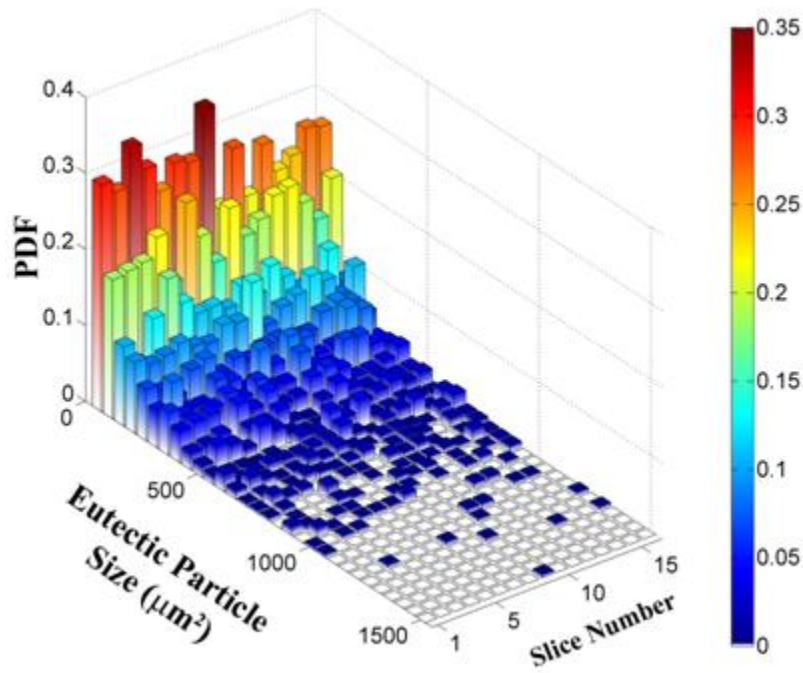


Figure 3.2.8. Bar graphs showing the discrete probability density functions of eutectic particle size for the sixteen slices, shown collectively in 3D to highlight slice-to-slice variation.

3D statistics

Figure 3.2.9 shows the particle volume distribution for the 3D reconstructed eutectic particles. First, eutectic particles which intersected the sides of the image regions or the top or bottom images were removed, *i.e.*, cases where all of the eutectic particle pixels may not have been captured. After this step, particle pixels that extended from one slice to another were connected to form one 3D eutectic particle – 1394 whole particles were captured. For each eutectic particle, the particle volume was calculated by multiplying the number of pixels in each eutectic particle by $40 \mu\text{m}^3$, *i.e.*, $2\text{-}\mu\text{m}$ pixel spacing in both directions of the images by the $10\text{-}\mu\text{m}$ slice spacing. On average, the 3D eutectic particles have a particle volume of $3751 \mu\text{m}^3$ (equivalent diameter of $19.3 \mu\text{m}$). Again, for properties controlled by extreme values, the maximum value of the eutectic particle volume was $38040 \mu\text{m}^3$, over ten times larger than the average particle volume. The four largest eutectic particles are rendered on the histogram plot to illustrate the eutectic morphology. The steps or ledges on the rendered particles correspond to the transition between eutectic particles on different slices. It is important to consider that the resolution of the dataset can significantly affect the average particle volumes, *i.e.*, these values may underestimate or overestimate volumes when compared to higher resolution images that are taken at a $2\text{-}\mu\text{m}$ slice interval to give a cubic voxel. Future work will attempt to improve both resolution and image quality to enhance particle morphology and statistics.

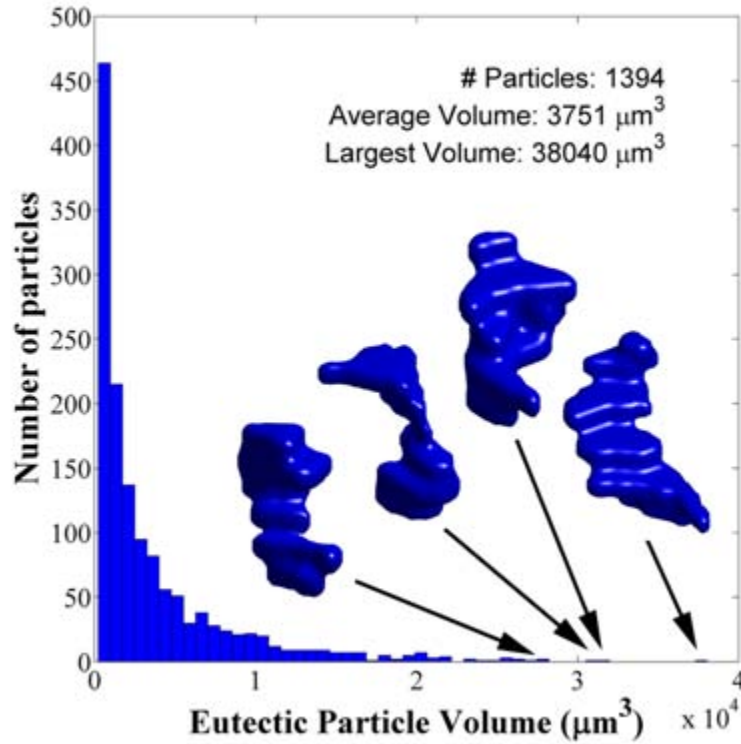


Figure 3.2.9. Histogram plot showing the volume distribution for the 1394 3D eutectic particles. The four largest particles are rendered.

Figure 3.2.10 shows particle length distribution in the dendrite growth direction for the 3D reconstructed eutectic particles with a rendering of the four largest particles. On average, in the dendritic growth direction, the eutectic particles' length is $19\text{ }\mu\text{m}$, *i.e.*, approximately 2 slices. There were 674 particles (of 1394, approximately 48%) that only appeared on one slice; a finer spacing of slices is needed to accurately capture the 3D morphology of these smaller particles. On the other hand, the maximum length of the eutectic particles in the growth direction was $90\text{ }\mu\text{m}$ with multiple particles having lengths of $70\text{ }\mu\text{m}$ (3 particles), $60\text{ }\mu\text{m}$ (13 particles), and $50\text{ }\mu\text{m}$ (42 particles). The upper bound for lengths in the growth direction can be influenced by the secondary dendrite arm spacing, which is on the order of the maximum lengths found here [32]. Interestingly, the curvature observed in the longest particle may indicate that some particles tend to grow around the secondary dendrite arms as well. The four largest eutectic particles by volume had lengths in the growth direction of 50 and $60\text{ }\mu\text{m}$ and the four longest particles had volumes greater than $1500\text{ }\mu\text{m}^3$, indicating some degree of correlation between the eutectic particle volume and the length in the growth direction.

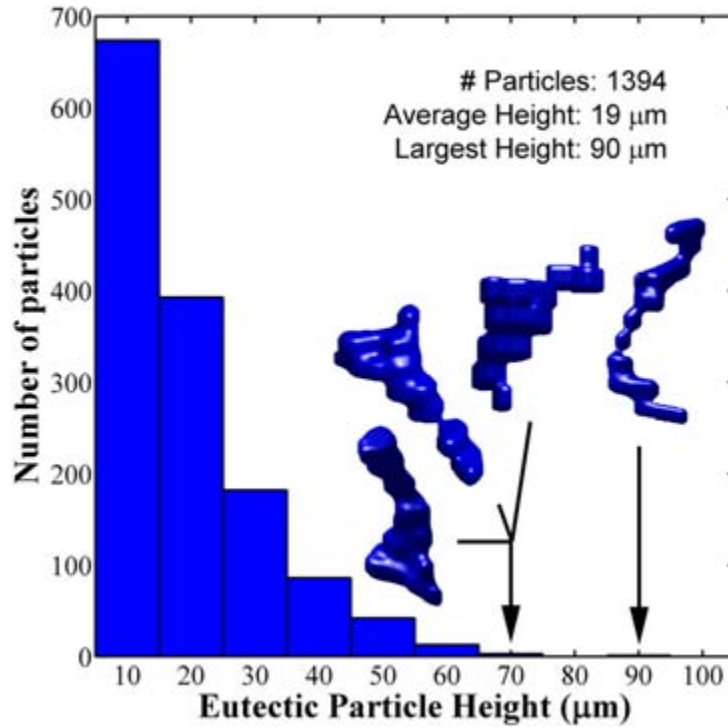


Figure 3.2.10. Histogram plot showing the eutectic particle length distribution for the 1394 3D eutectic particles. The four largest particles are rendered.

Figure 3.2.11(a) shows the nearest neighbor distance distribution for the eutectic particles. As with the 2D nearest neighbor distances, the nearest neighbor distance is based on the x/y/z centroid coordinates for each eutectic particle. Figure 3.2.6(b) normalizes the nearest neighbor distance by the equivalent particle diameter. On average, the nearest eutectic particle is approximately 61 μm , or 4 times the equivalent particle diameter, away. Note that these average nearest neighbor distances are approximately half of those calculated from the 2D images, reinforcing the necessity of collecting 3D particle statistics for reconstructing 3D synthetic volumes.

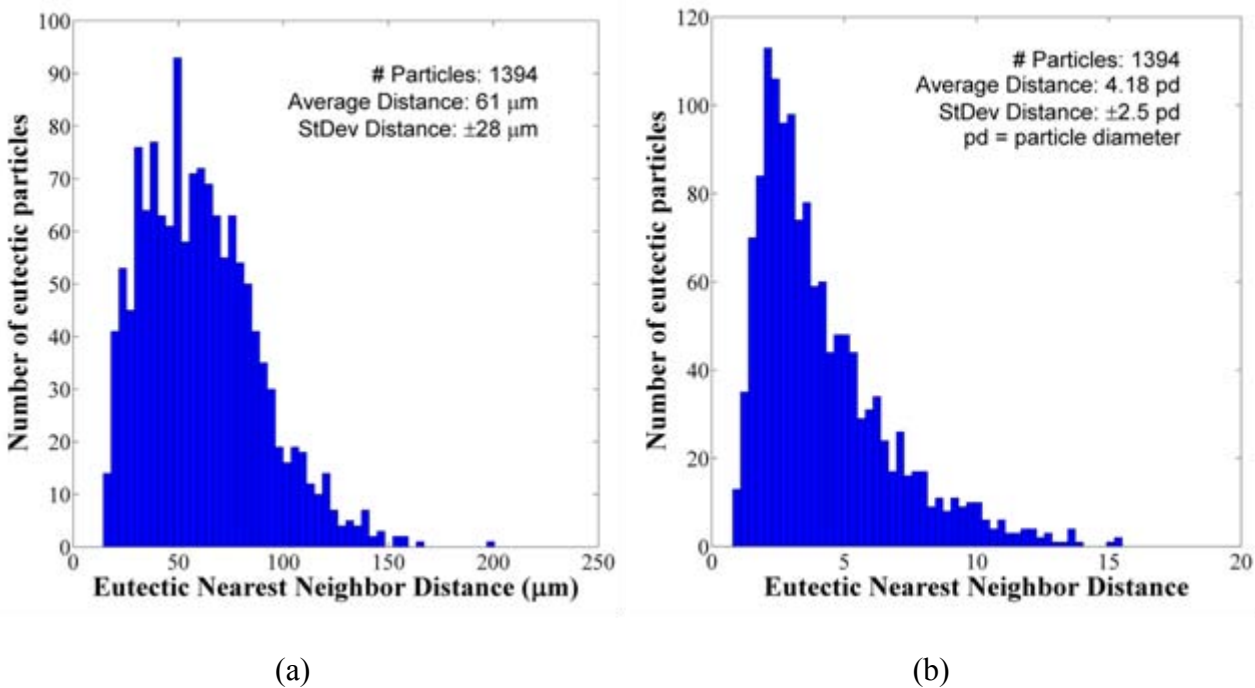


Figure 3.2.11. (a) Histogram showing the nearest neighbor distance distribution for the 1394 3D eutectic particles. (b) Histogram showing the nearest neighbor distance normalized by the size of the eutectic particle, *i.e.*, the average distance between eutectic particles is approximately 4 times the particle equivalent diameter.

While this technique considerably reduces the amount of time that would be spent manually identifying all eutectic particles, this technique still requires some manual intervention. There are still opportunities for improving the technique to reduce the amount of manual intervention. One opportunity is to refine the seed detection algorithm. At this point, the seed detection algorithm is based upon Sobel edge detection filters, which tend to define seeds in some incorrect regions (*e.g.*, around scratches in the material). Image processing techniques that can reduce seeds in incorrect regions and capture seeds in small eutectic particles that are missed would certainly help reduce manual intervention. Additionally, improvements in image quality through image processing beforehand or through improving experimental methodology for capturing the images may further reduce manual intervention. These are left for future work, but are essential for automating this process to fully reconstruct the 3D eutectic particle structure in single crystal nickel-based alloys.

CONCLUSION

In this work, we discuss a methodology for automated detection of eutectic particles in optical images taken on serial sections through a production turbine blade made of a heat-treated single crystal Ni-based superalloy. The two important steps for region growing are the automated identification of the seed point within each particle and the automated stop point for the region

growing algorithm. The seed points for the region growing algorithm are identified using edge detection filters, while the region growing stops when the intensity difference between the particle and the surrounding interdendritic region is maximized. These image processing steps are suitable for segmenting eutectic particles in etched optical images with large contrast variability.

Once detected, the segmented eutectic particles can be used to calculate microstructural statistics for characterization of single crystal Ni-based superalloys. In addition to histograms of eutectic particle size and their spatial arrangement, two-point correlation functions show that their occurrence is not impacted by the free surface of the blade. Also, the slice-to-slice variability is much greater for extreme values of particle size and particle major axis length. The significance of this work is its ability to automate characterization for analyzing the 3D morphology and statistics of eutectic particles.

REFERENCES

- [1] J.E. Spowart, *Scripta Materialia* 55 (2006) 5-10.
- [2] J.E. Spowart, H.M. Mullens, B.T. Pachula, *JOM* 55(10) (2003) 35-37.
- [3] J. Alkemper, P.W. Voorhees, *Journal of Microscopy* 201 (2001) 388-394.
- [4] M.D. Uchic, M. De Graef, R. Wheeler, D.M. Dimiduk, *Ultramicroscopy*, in press.
- [5] Groeber, Ghosh, Haley, Uchic, Dimiduk, *Materials Characterization* 57 (2006) 259-273.
- [6] W. Xu, M. Ferry, N. Mateescu, J.M. Cairney, F.J. Humphreys, *Materials Characterization* 58 (2007) 961-967.
- [7] W. Xu, M. Ferry, J.M. Cairney, F.J. Humphreys, *Acta Materialia* 55 (2007) 5157-5167.
- [8] B.J. Inkson, M. Mulvihill, G. Mobus, *Scripta Materialia* 45 (2001) 753-758.
- [9] J. Madison, J.E. Spowart, D.J. Rowenhorst, T.M. Pollock, *JOM* July (2008) 26-30.
- [10] J. Madison, J.E. Spowart, D.J. Rowenhorst, J. Fiedler, T.M. Pollock, *Superalloys Conference Proceedings* (2008) 881-888.
- [11] J.L. Fife, P.W. Voorhees, *Acta Materialia* 57 (2009) 2418-2428.
- [12] R. Mendoza, J. Alkemper, P.W. Voorhees, *Metallurgical and Materials Transactions A* 34 (2003) 481-489.
- [13] D. Kammer, P.W. Voorhees, *Acta Materialia* 54 (2006) 1549-1558.
- [14] D. Kammer, R. Mendoza, P.W. Voorhees, *Scripta Materialia* 55 (2006) 17-22.
- [15] M. Li, S. Ghosh, T.N. Rouns, H. Weiland, O. Richmond, W. Hunt, *Materials Characterization* 41 (1998) 81-95.
- [16] M. Li, S. Ghosh, O. Richmond, H. Weiland, T.N. Rouns, *MSE* 265 (1999) 153-173.
- [17] M.V. Kral, G. Spanos, *Acta Materialia* 47 (1999) 711-724.
- [18] M.V. Kral, M.A. Mangan, G. Spanos, R.O. Rosenberg, *Materials Characterization* 45 (2000) 17-23.
- [19] A.C. Lewis, J.F. Bingert, D.J. Rowenhorst, A. Gupta, A.B. Geltmacher, G. Spanos, *MSE* 418 (2006) 11-18.
- [20] D.J. Rowenhorst, A. Gupta, C.R. Feng, G. Spanos, *Scripta Materialia* 55 (2006) 11-16.
- [21] B. Maruyama, J.E. Spowart, D.J. Hooper, H.M. Mullens, A.M. Druma, C. Druma, *et al.*, *Scripta Materialia* 54 (2006) 1709-1713.
- [22] A.C. Lund, P.W. Voorhees, *Philosophical Magazine* 83 (2003) 1719-1733.
- [23] A.C. Lund, P.W. Voorhees, *Acta Materialia* 50 (2002) 2085-2098.
- [24] R.S. Sidhu, N. Chawla, *Materials Characterization* 52 (2004) 225-230.

- [25] S.G. Lee, A.M. Gokhale, A. Sreeranganathan, MSE A 427 (2006) 92-98.
- [26] M.A. Tschopp, M.A. Groeber, R. Farringier, J.P. Simmons, A.H. Rosenberger, C. Woodward, Scripta Materialia, in review.
- [27] S. Ghosh, J. Bai, P. Raghavan, Mechanics of Materials 39 (2007) 241-266.
- [28] M. Groeber, R. Farringier, D. Dimiduk, C. Woodward, *et al.*, unpublished research.
- [29] M.A. Tschopp, J.S. Tiley, G.B. Viswanathan, submitted, Materials Science & Technology.
- [30] MATLAB (2009a, The MathWorks, Natick, MA).
- [31] C. Przybyla, D. McDowell, IJP, *in press*.
- [32] M. Groeber, personal communication, 2009.

3.3. Symmetry-based Technique for Automated Extraction of Microstructural Features: Application to Dendritic Cores in Single Crystal Ni-Based Superalloys

Serial sectioning methods continue to produce a wealth of image data for quantifying the three-dimensional nature of material microstructures. In this subsection, we discuss a computational methodology for automated detection and 3D characterization of dendrite cores from images taken from slices of a production turbine blade made of a heat-treated single crystal Ni-based superalloy. The dendrite core locations are detected using an automated segmentation technique that incorporates information over multiple length scales and exploits the four-fold symmetry of the dendrites when viewed down the $\langle 001 \rangle$ growth direction. Additional rules that take advantage of the continuity of the dendrites from slice to slice help to exclude segmentation artifacts and improve dendrite core segmentation. The significance of this technique is that it can be extended to include any symmetry features such as mirror planes, improper rotations, or color symmetry, by using suitable matrix representations of these operations. For simplicity, only the four-fold rotation is included in this work.

INTRODUCTION

Knowledge of the three-dimensional (3D) nature of microstructural features may be important for ascertaining certain properties in many material systems. Serial sectioning is a labor-intensive, but effective, tool that is often used to provide datasets essential for characterizing the three-dimensional (3D) microstructure in many material systems. The ability to automate the removal of material at controlled rates through either mechanical polishing [1-3], microtome milling, or focused ion beam milling [4-8], has enabled researchers to obtain 3D microstructure datasets at a range of length scales. To further enhance the speed of collecting these datasets, the method of removal is often coupled with the imaging instrument, *e.g.*, mechanical polishing with optical imaging [1], or FIB with EBSD imaging [4-7]. This technique has helped to produce the 3D microstructure in a number of materials, *e.g.*,

- the polycrystalline grain structure in Ni-based superalloys (IN100) [5]
- the dendritic structure in single crystal nickel-based superalloys [9, 10], Al-Cu alloys [11, 12], and Pb-Sn alloys [13, 14]
- reinforcement particle for particle-reinforced metal-matrix composites [15, 16]
- microstructure (cementite, ferrite, austenite, martensite, and pearlite) colonies in alloy steels [17-20]
- the structure of pitch-based carbon foams [21]
- the γ - γ' microstructure in Ni alloys [4, 22, 23]
- intermetallic particles in Sn-rich solder [24]
- pore morphology in die-cast magnesium alloys [25]

In this work, the 3D dendritic microstructure in single crystal nickel-based superalloys is investigated. Large montage images from the airfoil section of a turbine blade were used to obtain the 3D dendritic structure. In single crystal nickel-based superalloys, the dendritic structure is the most striking feature of the microstructure as this is the first region to solidify. In addition to providing insight into its growth within the turbine blade, the 3D dendritic structure may also provide insight into the occurrence and spatial relationship of pores and eutectic particles, which may be important to consider for fatigue simulations. Parallel work concentrates on automated detection and 3D characterization of eutectic particles to reconstruct the interdendritic structure of the blade [26]. Identifying both of these features is important for obtaining a quantitative description of the structure of single crystal nickel-based superalloys used in turbine blade applications.

Successful efforts to automate serial sectioning techniques to produce large sets of microstructure images [1, 2, 9, 10] have led to overwhelming amounts of data resulting in a bottleneck at the image processing and analysis step. This statement is particularly true for the image segmentation step in complex multi-component microstructures, *e.g.*, the eutectic particles, pores, carbides, and dendrites in the single crystal microstructure investigated here. While manual identification of dendrites in single crystal nickel-based superalloys can be done for tens to a few hundred dendrites, this process is very time-consuming for larger numbers of dendrites. Typical data sets can contain 50 or more serial slices with at least 250 dendrite cores per slice, so the time required to manually identify these features is substantial. Automating the identification and reconstruction of microstructural features will be required for this approach to reach its full potential. Reliable assessment of microstructural statistics will require processing large datasets.

The rapid growth in 3D microstructure characterization is driven by the requirements of integrated computational models that link processing to properties and performance. From a properties perspective, 3D microstructure statistics can enhance the predictive capability of finite element models that take microstructure into account. Reconstructing the microstructure at the relevant length scale(s) for high temperature mechanical behavior can be used in concurrent multi-scale FE models that account for material microstructure. For instance, Ghosh and coworkers [27] have developed a concurrent multi-level model whereby multiple levels of refinement are used to simulate crack growth behavior. The level zero continuum approximation corresponds to a constitutive response consistent with a homogenization of microstructure and properties over the entire domain of the turbine blade. Level one would capture the variation in response produced by crystal rotations of different dendritic domains, and the density of primary dendrites (primary dendrite arm spacing). Finer details in the microstructure such as the secondary arm spacing, eutectic phase, carbide and void distribution would be captured in a level two representation. One objective of this research is to measure the statistics necessary to generate statistically representative volume elements for inclusion in these models.

The present article discusses an automated image processing technique for extracting *symmetric* features in microstructural images. In materials science applications, symmetry often plays a role in the development of microstructure (especially in crystallography), yet symmetry is seldom used for image processing techniques. Subsequently, this technique is applied to a single

crystal nickel-based superalloy to identify dendrite core locations by using their four-fold symmetry as viewed along the $\langle 100 \rangle$ growth direction. First, we show the acquired serial images and describe the difficulties encountered with extracting dendrite core locations from these serial images. Second, we describe the automated symmetry-based technique and its application to images that contain both microstructure and mount material, its use of slice continuity for improved segmentation, and its current problems and potential areas of improvements. The significance of this technique is that it can be extended to include any symmetry features such as mirror planes, improper rotations, or color symmetry, by using suitable matrix representations of these operations. For simplicity, only the four-fold rotation is included in this work.

IMAGE ACQUISITION

Figure 3.3.1 shows an etched optical image montage for a serial slice perpendicular to the nominal growth direction of a single crystal nickel-based superalloy (PWA 1484) turbine blade, which was filet cut through the interior passage. Further details of the experimental method for obtaining the images are given in Groeber *et al.* [28]. The green (small) box is an image showing a single dendrite as viewed from the $\langle 100 \rangle$ growth direction and is used for describing the algorithm in Figure 3.3.2. The blue (intermediate) box is an image of a group of dendrites along with eutectic particles (bright particles within the interdendritic area), which is used to assess the symmetry-based technique (Figure 3.3.3). Last, the red (large) box delineates a 6-mm x 6-mm (3000 x 3000 pixels) subset of the turbine blade that is subsequently used to test the technique on a microstructural area with a large number of features that can bias the calculation (*i.e.*, both the mount material and eutectic particles).

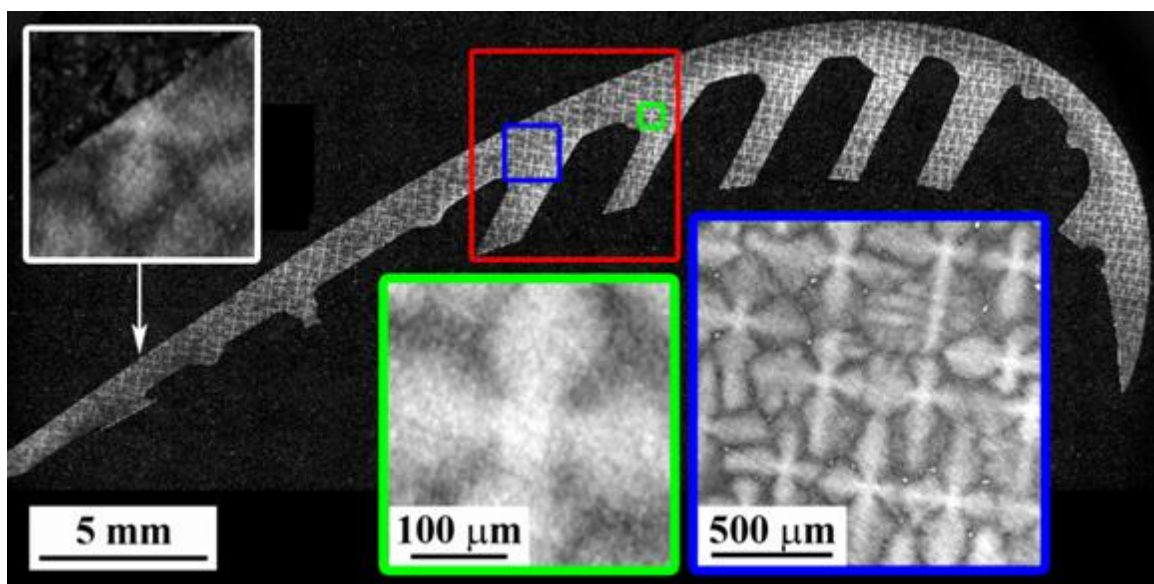


Figure 3.3.1. This image montage shows the microstructure of a cross-section of a single crystal nickel-based superalloy turbine blade. The red, blue, and green boxes highlight microstructural areas used for the symmetry-based technique.

There are several problems associated with manual or standard image processing methods to identify dendrite cores.

1. **Large amount of image information.** The large size of the images and the potential number of slices required to reconstruct the dendritic structure for a large amount of material make it difficult to manually identify the dendrite cores in each slice. For instance, the pixel spacing for the optical images is approximately 2- μm and the image size shown in Figure 3.3.1 is 35 mm x 8 mm (17544 x 4244 pixels). The number of dendrite cores manually identified routinely approaches 500 or more in some slices.
2. **Intensity changes within image.** The etchant used to highlight dendrite cores can etch material at different rates within the same slice, varying the contrast in intensity for the dendrite cores and arms. Additionally, each montage image is the result of stitching a 2D array of individual images together. Occasionally, an individual image may be out-of-focus or the image contrast may change slightly in the region where two individual images were stitched together. Standard methods for leveling the contrast within the blade region to correct this do not account for the mount material, which would incorrectly skew intensity values near the edges of the blade.
3. **3D dendrite morphology.** The 2D shape of the 3D dendrite structure is continually changing on successive images. Additionally, the dendrite arms within a serial slice may not all be similarly oriented, *i.e.*, there may be a range of dendrite arm orientation angles with respect their respective dendrite cores. Both of these can be problematic for cross correlation techniques [29, 30], which typically use a template (a particular object or region, *e.g.*, a typical dendrite shape in this case) to determine the locations of similar features within a larger image.

Therefore, a technique other than manual identification is required for processing these large images. To address these problems, the automated symmetry-based technique presented is almost entirely automated, requiring very little operator intervention. Also, this technique uses image information from the local region around each pixel to offset any potential intensity contrast over the serial montage image due to the image acquisition process. Moreover, by using the four-fold symmetry of the dendrite arms as viewed from the $\langle 001 \rangle$ growth direction, the problematic element of the potential variability in the dendrite arm orientations for cross correlation techniques is eliminated.

FOUR-FOLD SYMMETRY FILTER

Methodology and Application to Simple Image

Conventional image processing uses only the intensity information in the image, which is conventionally known as “observation information.” This work builds on conventional methods by including the “prior information” that the cores should, on average, have four-fold symmetry, when viewed along the $\langle 100 \rangle$ growth direction (*i.e.*, see the green box in Figure 3.3.1). The observation information would be the differences in intensity and textures for the different

constituents of the image: the mount material, the dendrites, the eutectic particles and the interdendritic region. Combining this observation information with the prior information of the symmetry allows automatic identification of the cores.

By calculating a quantitative symmetry parameter for each pixel in an intensity image, those pixels in local neighborhoods with a high four-fold symmetry parameter can be detected using a simple threshold. Figure 3.3.2 shows a schematic of how the symmetry parameter is evaluated for a single pixel without accounting for mount material or eutectic particles. The red (large) image from Figure 3.3.1 is shown in Figure 3.3.2(a). The four-fold symmetry parameter for a single pixel within this image is calculated as follows:

- (1) A single pixel within Figure 3.3.2(a) is chosen to calculate the four-fold symmetry parameter. Then, a local neighborhood around the pixel is identified for a particular length scale (*e.g.*, 300- μm x 300- μm in Figure 3.3.2) and the associated intensity image of this neighborhood is used for the four-fold symmetry filter (Figure 3.3.2(b)).
- (2) The intensity image (Figure 3.3.2(b)) is subsequently rotated by 90° three times to produce the images shown in Figures 3.3.2(c)-3.3.2(e).
- (3) A local average intensity image (Figure 3.3.2(f)) is calculated from the four rotated images in Figures 3.3.2(b)-3.3.2(e). When there are features within the local neighborhood that should not be taken into account for the four-fold symmetry parameter, the average intensity image may need to be corrected. Figure 3.3.2(g) is the result after accounting for these features (no effect in this example). How this technique accounts for these features is shown in Figure 3.3.5 and discussed later.
- (4) Figure 3.3.2(h) shows an image of the deviation at every pixel between the intensity values in Figure 3.3.2(g) and Figure 3.3.2(b). The l^2 -norm (square root of the sum of the squares of the pixels) is inverted to calculate the symmetry parameter of the local neighborhood for the single starting pixel.

To test the applicability of the four-fold symmetry filter to extracting dendrite core locations, the 1.4-mm x 1.4-mm blue (intermediate) image was selected from the serial slice. Three different neighborhood sizes were used to investigate the influence of neighborhood size on the results: 100, 200 and 300 μm . Figure 3.3.3 shows the resulting images for the four-fold symmetry filter using neighborhood sizes of 100 μm (a), 200 μm (b), and 300 μm (c). Visual comparison of the dendrite core locations in the original image (Figure 3.3.1, blue) with the four-fold filtered images shows that the intensity is high in the dendrite core locations. However, the intensity is also often high in the secondary arms and sometimes in the interdendritic area, so a simple threshold at any length scale may be inadequate for segmenting the dendrite core locations from these filtered images. The original intensity information can also be useful for detecting the correct symmetric features (*e.g.*, distinguishing four-fold symmetric dendritic regions from four-fold symmetric interdendritic regions). Also, notice that the eutectic particles in Figures 3.3.3(a)-3.3.3(c) are shown in black. This does not reflect an absence of four-fold symmetry in these particles; rather, the eutectic particles were previously segmented and are accounted for in the four-fold symmetry filter so they do not affect the extraction of the dendrite core locations.

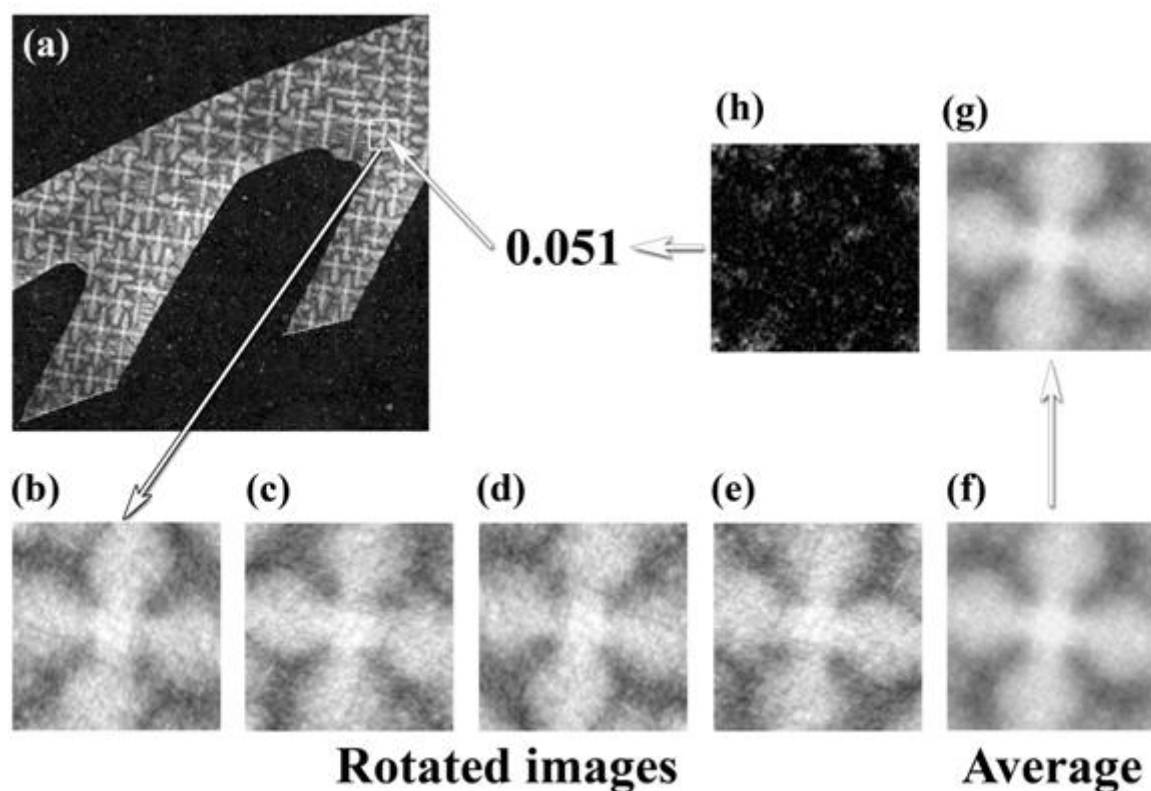


Figure 3.3.2. This schematic shows how a single pixel within the image is processed using the four-fold symmetry filter. A 300-μm x 300-μm local image (b) surrounding a single pixel within (a) is chosen and rotated in 90° increments to produce (c)-(e). Image (f) is the average of the four rotated images and (g) is the corrected average for the mount material and eutectic particles (not required here). Image (h) shows the deviation between image (g) and image (b). The inverse of the sum of the values in image (h) is the four-fold symmetry parameter for the starting pixel.

The technique was made more robust by segmenting the dendrite core locations with a vector-based segmentation approach using the four-fold symmetry parameters. In this manner, each pixel within the original image has a vector associated with it that reflects information from multiple length scales. For example, in this case, the four-fold symmetry parameters for local neighborhood sizes of 100, 150, 200, 250, and 300 μm were used to construct a vector-based image to help segment the dendrite cores. Then, the dimensionality of this vector-based image is reduced by taking the l^2 -norm of the vector within each pixel and multiplying by the original intensity image (to further reduce peaks in secondary/tertiary dendrite arms and interdendritic areas). Again, the intensity information of the original image is used to differentiate four-fold symmetry in the dendrite cores from that in the interdendritic regions.

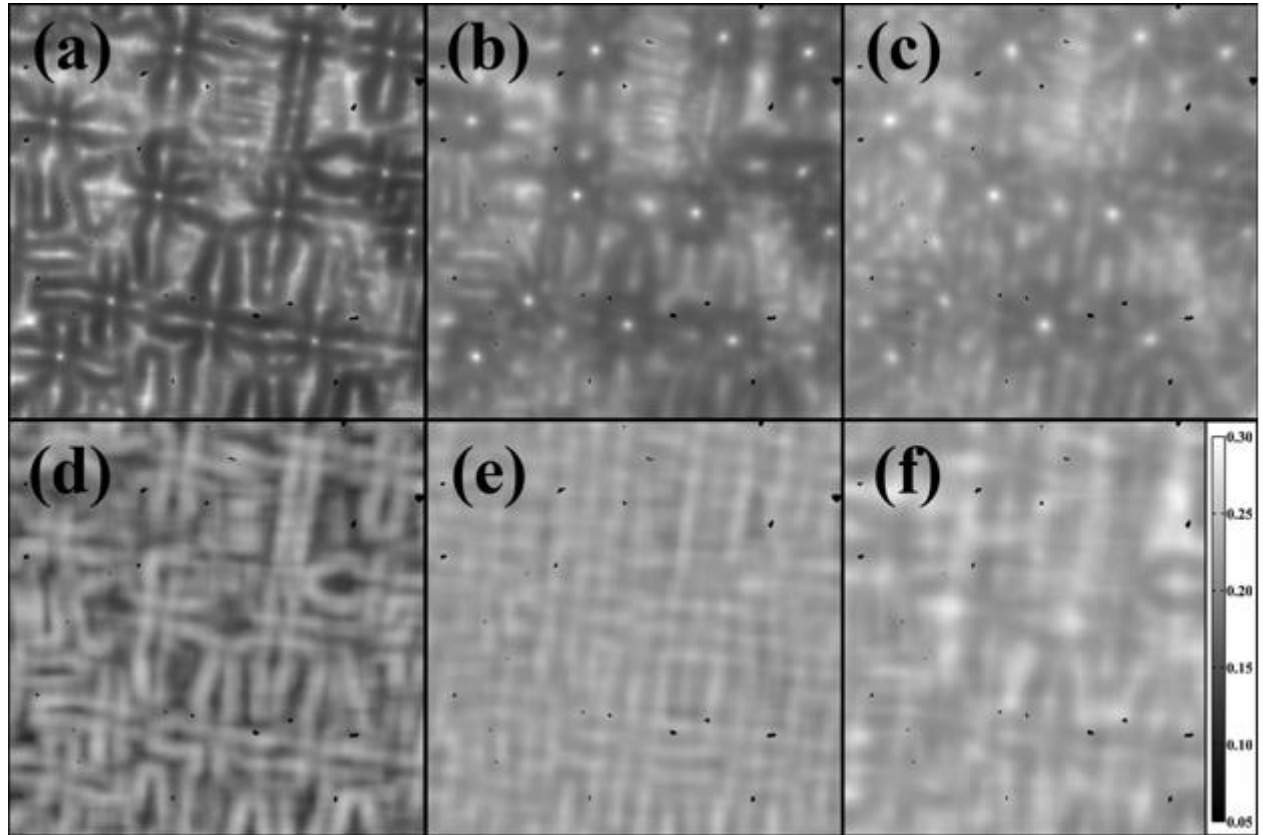


Figure 3.3.3. The four-fold symmetry filter was applied to the original intensity image (shown in blue in Figure 3.3.1). The resulting values from the symmetry filter are rescaled to form 8-bit images and are shown in (a), (b), and (c) using neighborhood sizes of $n = 100 \mu\text{m}$, $200 \mu\text{m}$, and $300 \mu\text{m}$, respectively. The corresponding weighting factor images for (a), (b), and (c) are shown in (d), (e), and (f), respectively.

Additionally, weighting the four-fold symmetry parameter at different length scales using the corresponding standard deviation of the local neighborhood intensities is important for smaller length scales where high four-fold symmetry parameters may reflect that the homogeneity of intensities within a local neighborhood rather than the actual four-fold symmetry (*e.g.*, the local region lies entirely within a dendrite arm). Figures 3.3.3(d)-3.3.3(f) show the weighting factors for the corresponding images in Figures 3.3.3(a)-3.3.3(c), using the standard deviations from neighborhood sizes of $100 \mu\text{m}$, $200 \mu\text{m}$, and $300 \mu\text{m}$, respectively. The values on the scale marker on the right-hand side of Figure 3.3.3(f) reflect the five different neighborhood sizes. The weighting factor for each pixel at each scale is simply the standard deviation for intensities within that neighborhood divided by the sum of standard deviations over all scales for that pixel. Notice that some of the high four-fold symmetry values in the $100 \mu\text{m}$ image (Figure 3.3.3(a))

have a low weighting factor (~ 0.05) in Figure 3.3.3(d), whereas the weighting factor would be 0.20 if all scales were weighted evenly. This desensitizes the vector-based image to high four-fold symmetry values due to similar intensities over a local neighborhood on a per pixel basis.

Figure 3.3.4 shows images from the vector-based segmentation. Figure 3.3.4(a) shows the single output image generated by combining the four-fold symmetry images with the weight factor images at the five neighborhood sizes. While many of the dendrite cores have high four-fold symmetry values, some interdendritic areas also have high four-fold symmetry values. Figure 3.3.4(b) multiplies Figure 3.3.4(a) by the original intensity image. If the background intensity changes significantly, the original intensity image may need to be leveled before this operation. Figure 3.3.4(c) shows the image after applying further image processing operations to help accentuate the peaks for detection. First, Gaussian smoothing is used to reduce noise within the image. Then, a morphological top hat filter is applied to enhance the peak definition.

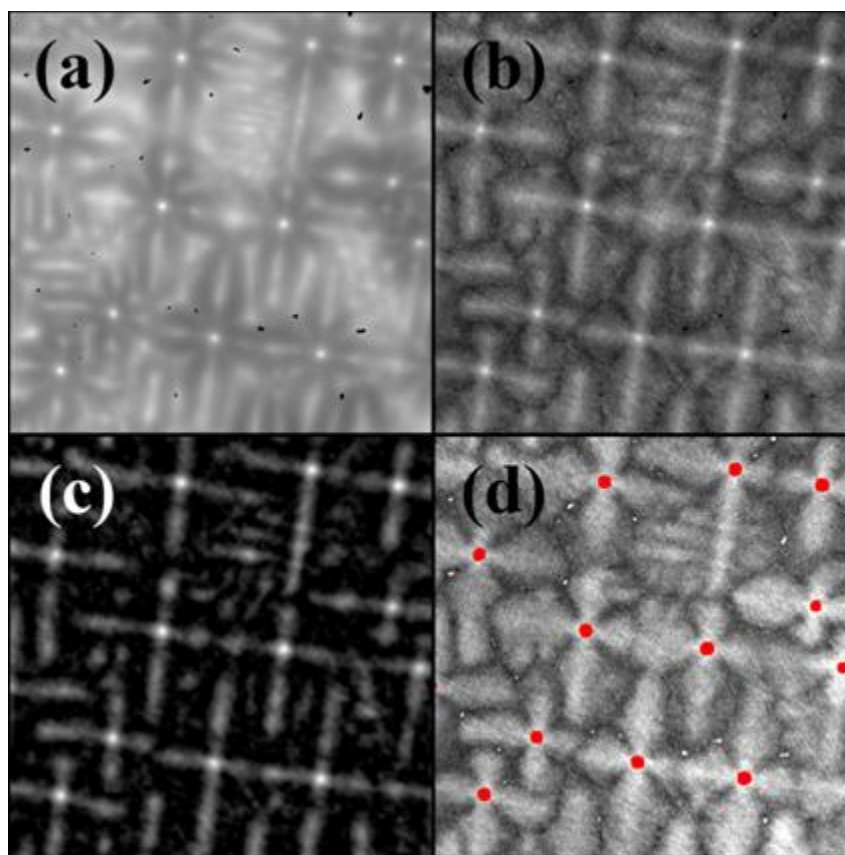


Figure 3.3.4. Image (a) was obtained using the four-fold symmetry and weighting factor images at five length scales (*e.g.*, see the images in Figure 3.3.3). After multiplying by the original intensity image (b), a further Gaussian and top hat operation are applied to produce the vector-based final image (c). A user-specified threshold parameter was applied to (c) and the segmented dendrite cores (red) are superimposed onto the original intensity image (d).

The resulting image from the multi-scale four-fold symmetry filter (Figure 3.3.4(c)) can now be segmented to extract the dendrite core locations. Prior to this point, the four-fold symmetry filters can operate in an automated fashion requiring no user intervention. While various automated segmentation methods exist [e.g., 31-32], this image is easily segmented using a user-defined threshold parameter. In this image, the range of user-defined intensity thresholds that correctly identified all dendrite core locations was quite large (range of 141-202 when this image was rescaled to an 8-bit image). Figure 3.3.4(d) superimposes the segmented dendrite core locations (in red) obtained using a threshold parameter of 142 onto the original intensity image. This technique identified all the dendrite cores while only requiring the manual manipulation of a single parameter (the threshold parameter).

Application to Complex Image with Edge Effects

Extending the four-fold symmetry filter to the large image in Figure 3.3.1 requires dealing with edge effects due to the mount material, though. For instance, in local neighborhoods that contain the mount material, the four-fold symmetry would be extremely low for a dendrite core near the boundary. Therefore, the mount material needs to be accounted for in the symmetry filter. Moreover, the eutectic particles can decrease the four-fold symmetry value in a similar way to the mount material. In prior work [26], the mount material and eutectic particles were segmented for 16 successive serial images that were spaced approximately 10 μm apart. As an example of how the four-fold symmetry filter is modified to account for edge effects, this same set of 6 x 6-mm images is used in this article.

Figure 3.3.5 shows a schematic of how a single pixel within the image is processed using the four-fold symmetry filter at a single length scale (300 x 300 μm). This schematic is similar to that in Figure 3.3.2, except that the mount material and eutectic particles are included in this region. The four-fold symmetry value for a single pixel within this image is calculated as follows:

- (1) A single pixel within Figure 3.3.5(a) is chosen and then a 300 x 300- μm intensity image centered about the pixel is used for the four-fold symmetry filter (Figure 3.3.5(b)). A complementary 300 x 300- μm binary image for Figure 3.3.5(b) that indicates pixels belonging to the mount material and eutectic particles (in black) is also shown in Figure 3.3.5(g). Additionally, the mount material and eutectic particles are given an intensity value of zero in Figure 3.3.5(b).
- (2) The intensity image (Figure 3.3.5(b)) and binary image (Figure 3.3.5(g)) are rotated by 90° three times to produce the images shown in Figures 3.3.5(c)-3.3.5(e) and Figures 3.3.5(h)-3.3.5(j), respectively.
- (3) The four rotated images in Figures 3.3.5(b)-3.3.5(e) and Figures 3.3.5(g)-3.3.5(j) are averaged to generate Figures 3.3.5(f) and 3.3.5(i), respectively. This, however, does not account for the mount material or eutectic particles in the rotated images. Figure 3.3.5(l) corrects the average intensity by accounting for pixels where the mount material and eutectic particles have contributed.
- (4) Figure 3.3.5(m) shows an image of the squared deviation at every pixel between the intensity values in Figure 3.3.5(l) and Figure 3.3.5(b). Next, the values in Figure

3.3.5(m) are summed for all pixels which are not mount material or eutectic particles (*i.e.*, all the white pixels in Figure 3.3.5(g)). The inverse of this value is the four-fold symmetry value for the single starting pixel.

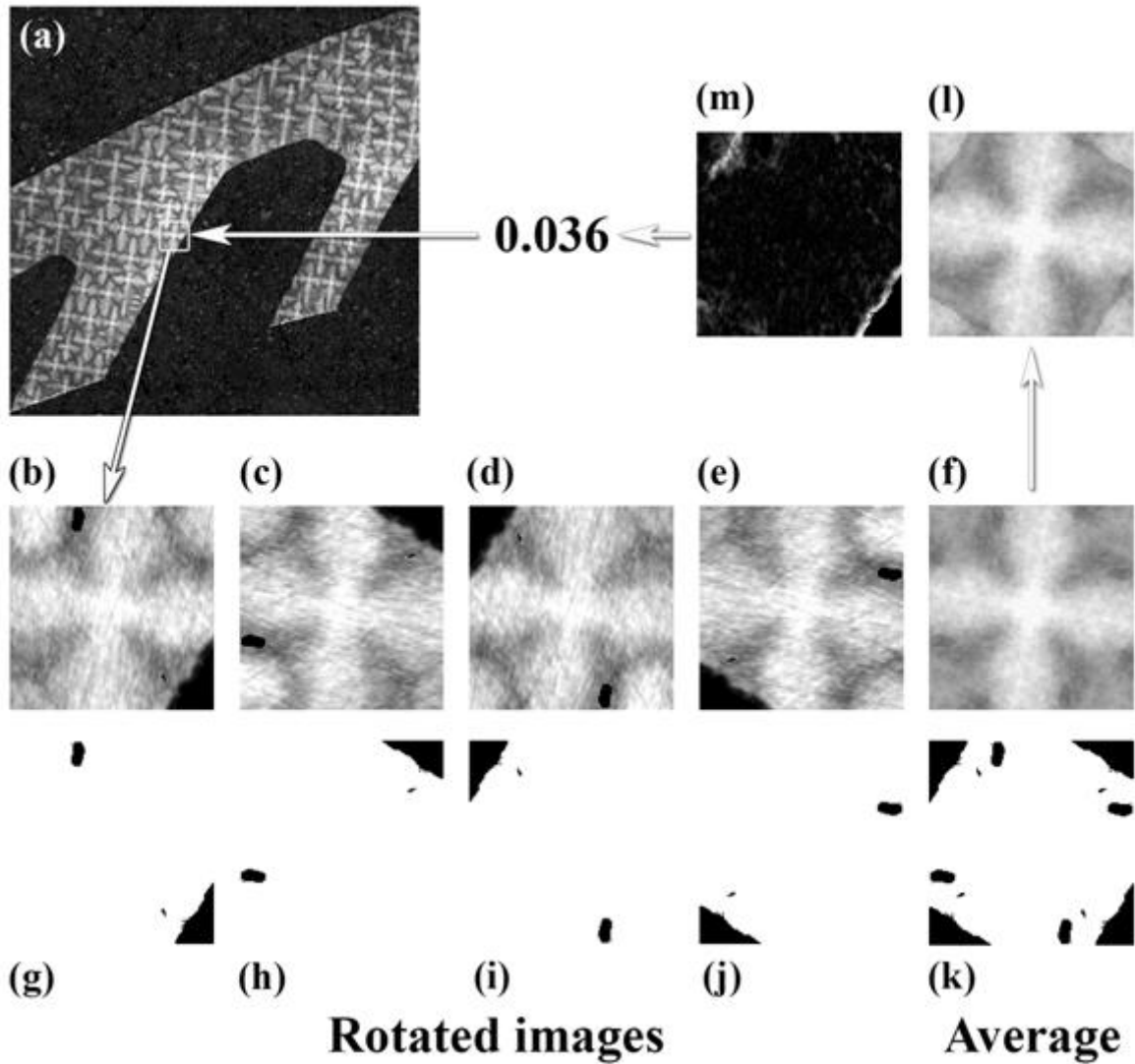


Figure 3.3.5. This schematic shows how a single pixel within the image is processed using the four-fold symmetry filter at a single length scale. A 300 x 300 μm neighborhood centered around a single pixel within (a) is chosen. Images (b)-(e) and (g)-(j) show the local image and its associated binary image (with mount and eutectic particles in black) for four 90° rotations. Images (f) and (g) are the average of the four rotated images. Image (l) corrects the average intensity for the mount material and eutectic particles, while image (m) shows the deviation

between image (l) and image (b). The inverse of the sum of the values in image (m) is the four-fold symmetry value for the starting pixel.

Figure 3.3.6(a) shows an example of one of the serial slices after applying the four-fold symmetry filter technique outlined in Figure 3.3.5 with the subsequent post-processing filters (Gaussian, top hat filters) as described previously. Figure 3.3.6(b) shows the original intensity image with the dendrite cores identified through a user-specified threshold parameter applied to Figure 3.3.8(a) (the red dots were enlarged slightly to show the dendrite core locations).

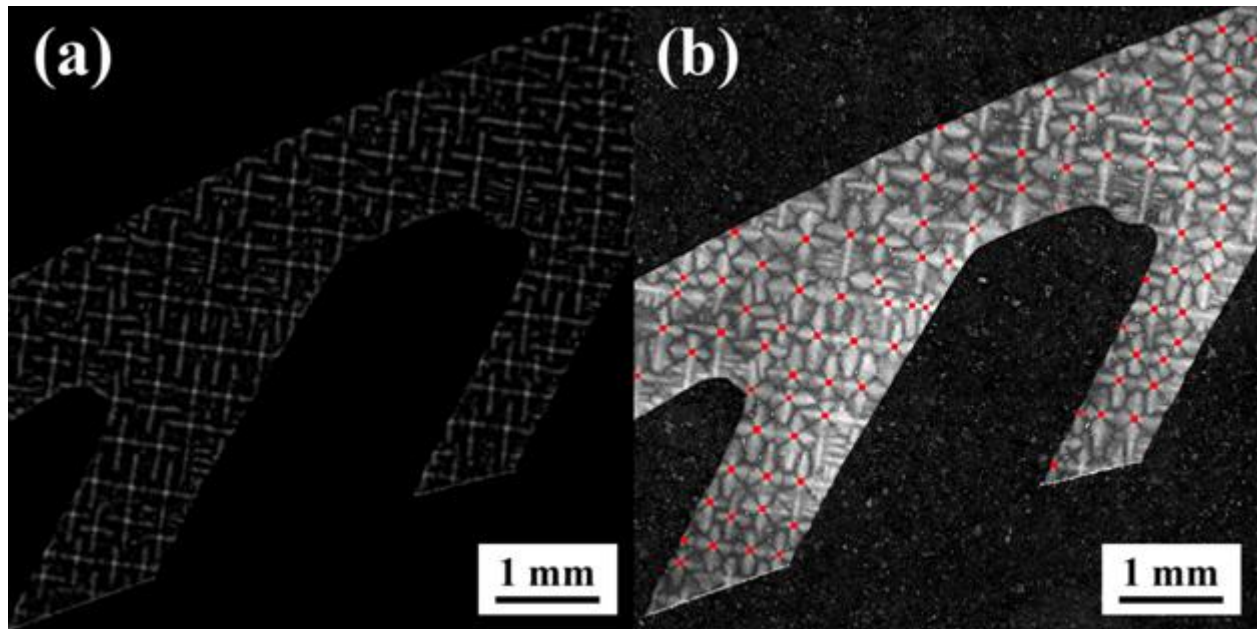


Figure 3.3.6. These images show an example of how the four-fold symmetry filter performs when applied to a 6-mm x 6-mm section of a serial slice. Figure 3.3.6(a) shows the vector-based final image and Figure 3.3.6(b) shows the original intensity image with the segmented dendrite cores (red) identified through a user-specified threshold parameter.

To assess the quality of this technique, the results of the automated symmetry-based technique were compared to the ground truth obtained from manual identification of the dendrite cores. The symmetry-based technique correctly identified 92 dendrite core locations in this image with only 1 area incorrectly identified as a dendrite core (secondary dendrite arm intersecting a tertiary arm near the mount material). Additionally, there was one dendrite core in the interior that was missed, but should have been detected. Several dendrite cores at the mount material/microstructure boundary were not identified, but might have been identified manually depending on the operator. Overall, the results of the symmetry-based technique are good considering the difficulty of accounting for confounding features within the image. As can be

observed from Figure 3.3.4(d), this technique does extremely well without these confounding features. The statistics from all 16 serial images show that, on average, 94 features were detected, of which 5.25 features were not dendrite cores (5.6%), and 6.31 dendrite cores were not detected (6.7%).

Improving Feature Extraction using Continuity Rules

The continuity of the dendritic cores from slice to slice can be exploited to improve extraction of dendrite core locations. A set of continuity rules may help locate missed dendrite cores and help discount incorrectly identified features. For instance, a dendrite core will typically appear on multiple slices. For missed dendrite cores, the adjacent slices may have detected dendrite cores, indicating that the missed dendrite core should probably be included. For incorrectly identified features, the adjacent slices may not have detected dendrite cores, indicating that the incorrectly identified feature is not a dendrite core.

An initial set of continuity rules was applied to the stack of 16 binary images generated using a manually-identified threshold parameter. First, the images obtained with the four-fold symmetry filter were aligned via rotation and translation using an autocorrelation technique¹. Then, the binary images were generated by (i) manually selecting a threshold parameter to segment the four-fold symmetry image for each slice, and (ii) replacing each segmented object² with a circle with radius c_1 . Then the following continuity rules were applied to improve the segmentation on individual binary images:

- **Minimum dendrite length.** The dendritic core will have a minimum length in the $\langle 001 \rangle$ direction of c_2 or greater. Therefore, this rule eliminates objects that may only appear on a few adjacent slices, but not any slices before or afterwards.
- **Minimum slice occurrence.** The dendritic cores appear on at least c_3 percent of the slices between the start and end of each dendrite. This rule eliminates objects that appear randomly over multiple slices spaced a distance c_2 or greater. This rule also adds dendrite cores to the binary serial images if they occur in a great enough frequency, assuming that they are bounded by the starting and ending slice of that particular dendrite core.
- **Minimum size threshold.** The dendritic cores grow vertically with respect to the aligned binary images and, hence, the circular objects should align fairly well. In general, this rule removes small artifacts with a size below c_4 that appear at the mount/material boundary.

¹ It is important to note that this will align the stack of images with the dendrite cores, not the fiducial markers in the mount. Subsequent re-alignment by the fiducial markers may be required in a later step.

² The term “object” is used to refer to a segmented area that may or may not be an actual dendrite core.

Applying these rules to a stack of serial images should eliminate most incorrectly segmented objects and add dendrite core locations to the slices where the four-fold symmetry filter generated a lower-intensity peak. To increase the accuracy of these rules, the operator may manually subtract segmented objects and add dendrite cores to establish a “ground truth” image every so many slices. For this stack of serial images, a “ground truth” image was generated for the first and last slice and the following parameters were used: $c_1 = 13$ pixels, $c_2 = 50 \mu\text{m}$, $c_3 = 25\%$, $c_4 = 400$ pixels.

Figure 3.3.7 examines how these continuity rules combine image information from multiple slices to improve the dendrite core extraction. Figure 3.3.7(a) shows the segmented objects (black) from all 16 slices on one image. Figure 3.3.7(b) shows the 70 objects that appear on all 16 slices. Since all of these objects are dendrite cores, this subfigure indicates that the dendrite cores in the interior of the blade are the easiest to segment. Note that over 70% of the dendrite cores were easily segmented on all 16 slices. As was observed in Figure 3.3.4(d), images with a low density of confounding features should have higher dendrite core detection rates. Figure 3.3.7(c) shows the objects eliminated by the continuity rules. Almost all of the objects eliminated were at the mount/microstructure boundary, although a few were in regions where the dendrite growth direction changed. Three of the deleted objects are circled in red to show that these may have been manually identified as dendrite cores at the mount/microstructure boundary; these have also been circled in the image in Figure 3.3.7(d). Figure 3.3.7(d) shows the modified extraction of the dendrite core locations using the continuity rules. The four-fold symmetry filter with the continuity rules does an effective job of extracting most dendrite cores. The blue circles in this subfigure represent dendrite cores that should have been detected, but were not detected due to inadequate image pre-processing. The problem responsible for detecting these dendrite cores is shown in Figures 3.3.8(e)-3.3.8(h) and is discussed later.

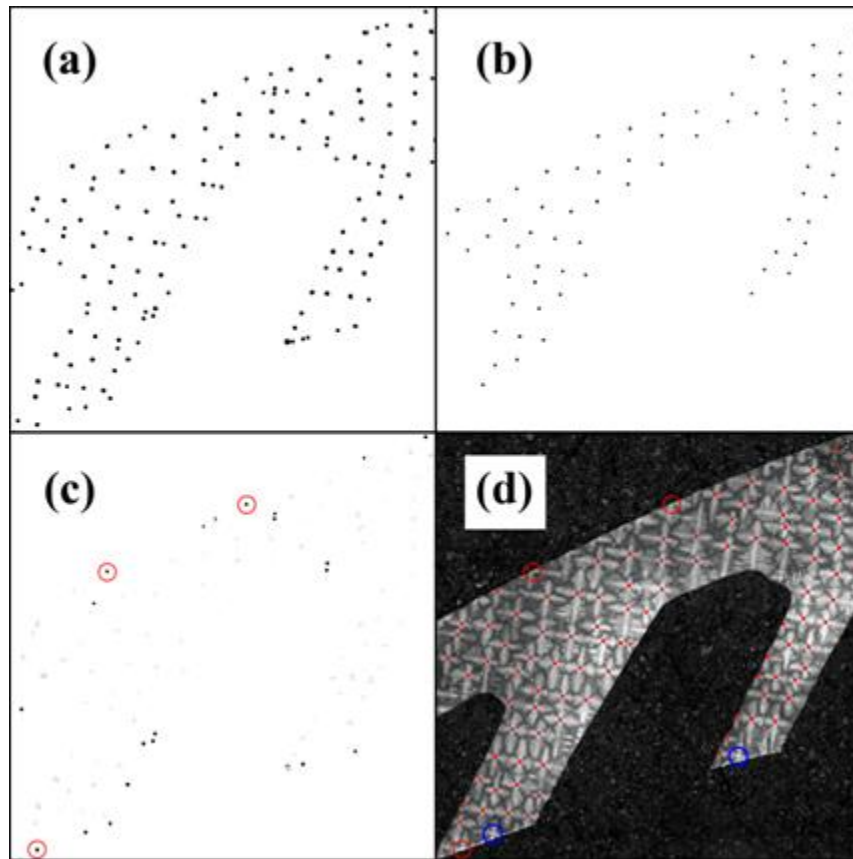


Figure 3.3.7. These images show the effect of applying continuity rules to combine image information from multiple slices. Figure 3.3.7(a) shows the segmented objects (black) from all 16 slices, Figure 3.3.7(b) shows the 70 objects that appear on all 16 slices, Figure 3.3.7(c) shows the objects eliminated by the continuity rules, and Figure 3.3.7(d) shows the modified extraction of the dendrite core locations using the continuity rules.

Current Problems / Potential improvements

This symmetry-based technique can considerably reduce the amount of time spent manually identifying all dendrite cores within a serial image the size of Figure 3.3.1 or larger. However, at this point, this technique can still be improved. Several problems were encountered when using this technique to identify dendrite cores in a single crystal turbine blade. Figure 3.3.8 shows some examples where the current technique has problems and where modifications can lead to potential improvements. These are left for future work, but would be essential for fully automating this process to construct the 3D dendrite core structure.

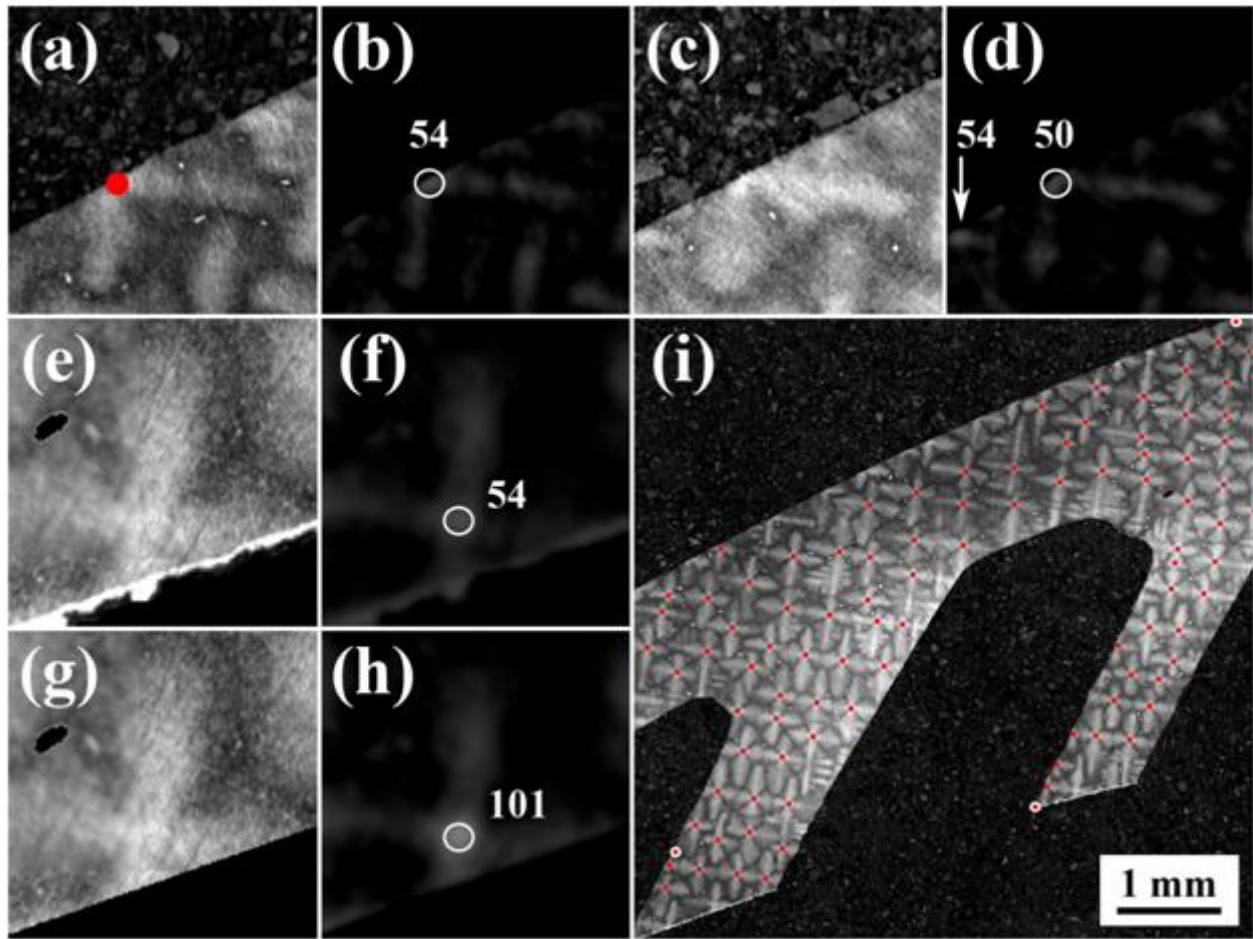


Figure 3.3.8. These images show examples of some problems as well as potential improvements to the current technique. Figures 3.3.8(a) and 3.3.8(c) show example images of dendrite cores at the mount/microstructure boundary and the difficulty with segmenting the dendrite core from the four-fold symmetry images (Figures 3.3.8(b) and 3.3.8(d), respectively). Figures 3.3.8(e) and 3.3.8(g) show how improving segmentation of the mount material can impact the four-fold symmetry value (in Figures 3.3.8(f) and 3.3.8(h), respectively). Figure 3.3.8(i) shows an example of automated selection of the threshold parameter for segmenting dendrite cores using a “ground truth” image from an adjacent slice.

Figures 3.3.8(a) and 3.3.8(c) show images on nearby slices, on which the dendrite core is detected on one and not on the other. Figures 3.3.8(b) and 3.3.8(d) show the complementary four-fold symmetry filtered images to Figures 3.3.8(a) and 3.3.8(c), where the maximum intensity in the dendrite cores was 54 and 50, respectively. However, in Figure 3.3.8(d), the white arrow points to a region with a higher intensity for this image (54), which would mean that an incorrect object would be identified prior to identifying the dendrite core at the boundary. Additionally, these subfigures illustrate the problem with identifying cores at the boundary – at

what point do the dendrite arms cease to have a core? In many cases, the intersection of the dendrite arms (the dendrite core) is right on the mount/microstructure boundary, or appears to be a little outside the boundary. While this is a problem with repeatability from slice to slice, modifying parameters within the continuity rules or adding new continuity rules may help to better identify dendrite cores at the boundaries.

The input image quality certainly affects the output of the four-fold symmetry technique. Improvements in the four-fold symmetry technique can be realized by reducing scratches and increasing intensity contrast within the serial intensity images through either experimental methodology or subsequent image processing techniques. Additionally, this technique uses the segmented mount material and eutectic particles. Improving the segmentation of either of these features will improve the results presented in this article.

One example of how improving segmentation would improve the results is shown in Figures 3.3.8(e) and 3.3.8(g). This dendrite core lies near the mount/microstructure boundary and was not identified on any of the slices with this technique. In both subfigures, the mount material and eutectic particles have been segmented and are indicated by black pixels. The difference between these figures is that in Figure 3.3.8(g), the segmented mount material was modified to remove the white pixels on the bottom edge of the microstructure (a remnant of the EDM file cut through the interior of the blade). The corresponding four-fold symmetry images are shown in Figure 3.3.8(f) and 3.3.8(h). The maximum intensity value for the dendrite core was increased by 87% in Figure 3.3.8(h), assuring detection of the dendrite core.

Reducing the amount of time spent manually selecting a threshold parameter to segment the four-fold symmetry filtered serial images would also improve the current technique. A potential method for automating this is to establish a “ground truth” image for the first slice and then automate the selection of this threshold parameter on subsequent adjacent slices by optimizing a penalty function. This penalty function can be based on the number correctly identified and the number incorrectly identified. Once the penalty function for the adjacent slice is optimized, this segmentation can then be used to optimize segmentation on the next slice. In this manner, all slices after the first slice can be automatically segmented using a penalty function. An example of maximizing a penalty function (number of correct minus the number incorrect) to automate segmentation is shown in Figure 3.3.8(i), where 91 dendrite cores are correctly identified and 3 objects are false positives.

CONCLUSION

This article discusses an automated technique for extraction of the spatial locations of dendrite cores from serial images taken a production turbine blade composed of a heat-treated single crystal Ni-based superalloy. The technique incorporates image information over multiple length scales and exploits the four-fold symmetry of the dendrites when viewed down the $\langle 001 \rangle$ growth direction. Additional rules take advantage of the continuity of the dendrites from slice to slice to help exclude segmentation artifacts and improve dendrite core segmentation. Automated techniques that operate on symmetric features can be a valuable tool for quantitatively characterizing material microstructures.

REFERENCES

- [1] J.E. Spowart, Scripta Materialia 55 (2006) 5-10.
- [2] J.E. Spowart, H.M. Mullens, B.T. Pachula, JOM 55(10) (2003) 35-37.
- [3] J. Alkemper, P.W. Voorhees, Journal of Microscopy 201 (2001) 388-394.
- [4] M.D. Uchic, M. De Graef, R. Wheeler, D.M. Dimiduk, Ultramicroscopy, in press.
- [5] Groeber, Ghosh, Haley, Uchic, Dimiduk, Materials Characterization 57 (2006) 259-273.
- [6] W. Xu, M. Ferry, N. Mateescu, J.M. Cairney, F.J. Humphreys, Materials Characterization 58 (2007) 961-967.
- [7] W. Xu, M. Ferry, J.M. Cairney, F.J. Humphreys, Acta Materialia 55 (2007) 5157-5167.
- [8] B.J. Inkson, M. Mulvihill, G. Mobus, Scripta Materialia 45 (2001) 753-758.
- [9] J. Madison, J.E. Spowart, D.J. Rowenhorst, T.M. Pollock, JOM July (2008) 26-30.
- [10] J. Madison, J.E. Spowart, D.J. Rowenhorst, J. Fiedler, T.M. Pollock, Superalloys Conference Proceedings (2008) 881-888.
- [11] J.L. Fife, P.W. Voorhees, Acta Materialia 57 (2009) 2418-2428.
- [12] R. Mendoza, J. Alkemper, P.W. Voorhees, Metallurgical and Materials Transactions A 34 (2003) 481-489.
- [13] D. Kammer, P.W. Voorhees, Acta Materialia 54 (2006) 1549-1558.
- [14] D. Kammer, R. Mendoza, P.W. Voorhees, Scripta Materialia 55 (2006) 17-22.
- [15] M. Li, S. Ghosh, T.N. Rouns, H. Weiland, O. Richmond, W. Hunt, Materials Characterization 41 (1998) 81-95.
- [16] M. Li, S. Ghosh, O. Richmond, H. Weiland, T.N. Rouns, MSE 265 (1999) 153-173.
- [17] M.V. Kral, G. Spanos, Acta Materialia 47 (1999) 711-724.
- [18] M.V. Kral, M.A. Mangan, G. Spanos, R.O. Rosenberg, Materials Characterization 45 (2000) 17-23.
- [19] A.C. Lewis, J.F. Bingert, D.J. Rowenhorst, A. Gupta, A.B. Geltmacher, G. Spanos, MSE 418 (2006) 11-18.
- [20] D.J. Rowenhorst, A. Gupta, C.R. Feng, G. Spanos, Scripta Materialia 55 (2006) 11-16.
- [21] B. Maruyama, J.E. Spowart, D.J. Hooper, H.M. Mullens, A.M. Druma, C. Druma, *et al.*, Scripta Materialia 54 (2006) 1709-1713.
- [22] A.C. Lund, P.W. Voorhees, Philosophical Magazine 83 (2003) 1719-1733.
- [23] A.C. Lund, P.W. Voorhees, Acta Materialia 50 (2002) 2085-2098.
- [24] R.S. Sidhu, N. Chawla, Materials Characterization 52 (2004) 225-230.
- [25] S.G. Lee, A.M. Gokhale, A. Sreeranganathan, MSE A 427 (2006) 92-98.
- [26] M.A. Tschopp, M.A. Groeber, R. Farringher, J.P. Simmons, A.H. Rosenberger, C. Woodward, MSMSE, in review.
- [27] S. Ghosh, J. Bai, P. Raghavan, Mechanics of Materials 39 (2007) 241-266.
- [28] M. Groeber, R. Farringer, D. Dimiduk, C. Woodward, *et al.*, unpublished research.
- [29] Russ, J.C., *The Image Processing Handbook*, 5th Edition (Boca Raton, FL, CRC Press, 2007).
- [30] Gonzalez, R.C., Woods, R.E., *Digital Image Processing*, 2nd Edition (Upper Saddle River, NJ, Prentice-Hall, 2002).
- [31] J.P. Simmons, P. Chuang, M.L. Comer, M. Uchic, J.E. Spowart, M. De Graef, MSMSE 17 (2009) 025002.
- [32] E.B. Gulsoy, M. De Graef, *Microscopy & MicroAnalysis*, 15(S2) (2009) 606CD

3.4. Automated Identification and Characterization of Secondary & Tertiary γ' Precipitates in Nickel-based Superalloys

The use of different electron loss edges in energy filtered transmission electron microscopy (EFTEM) has allowed researchers to capture images of the morphology and size of precipitates in nickel-based superalloys. In this subsection, we discuss a computational methodology for automated detection of secondary and tertiary γ' precipitates in EFTEM images. The optimum parameters for the automated region growing technique were identified using a combination of visual inspection and intensity information from the EFTEM images. The microstructural statistics obtained from the segmented γ' precipitates agreed with those of the manually segmented precipitates. Then, automated segmented precipitates are used to extract microstructural information about the distributions of equivalent diameters of 656 tertiary precipitates along with the distances to the nearest secondary precipitates. The significance of this technique is its ability to automate segmentation of precipitates in a reproducible manner for acquiring microstructural statistics that relate to both processing and properties.

INTRODUCTION

The underlying γ' precipitate structure in nickel-based superalloys plays a commanding role in the mechanical behavior of these alloys at high temperatures [1-3]. Previous work [4, 5] has shown that changes in processing can result in large changes in high temperature mechanical properties, such as creep and fatigue. Therefore, it is vital to be able to characterize the statistics related to γ' precipitates in these alloys to assess how influence of various processing conditions. Previous work by some of the present authors has shown that the use of automated image processing techniques are helpful in segmenting microstructure features that drive many of the strengthening mechanisms in titanium and nickel base super alloys [6-8]. Additionally, Tiley *et al.* [6] and others [9, 10] have shown that energy filtered transmission electron microscopy (EFTEM) is the state of the art technique for imaging γ' precipitates.

While much effort has been expended to refine techniques for imaging γ' precipitates in EFTEM images, the analysis of these images is also very important and in many cases can be the bottleneck of the process. Manual identification of the precipitate structure is very time-intensive and may not be reproducible between researchers. Automating the segmentation process for secondary and tertiary γ' precipitates is required to accurately compare the influence of processing on the underlying γ' structure. Reliable assessment of microstructural statistics related to the precipitate size distributions and distances between precipitates is critical for models that predict precipitate microstructure evolution and mechanical properties.

In this subsection, we present an *automated* technique for detecting secondary and tertiary γ' precipitates in EFTEM images of nickel-based superalloys. First, we briefly describe the processing history for the nickel-based superalloy and the acquisition process for the EFTEM images. Second, the automated technique used to identify the γ' precipitates is described. Third, several key parameters used in the automated technique are examined and optimized. Last, this automated technique is used to segment the secondary and tertiary γ' precipitates in eight EFTEM images and calculate the associated microstructural statistics. The significance of this technique is its ability to automate segmentation of precipitates in a reproducible manner for acquiring microstructural statistics that relate to both processing and properties.

EXPERIMENTAL METHODOLOGY

A nickel-based superalloy sample (Rene88DT) was cut from a forged disc developed under a Defense Advanced Research Projects Agency funded effort [11]. The sample was solutionized at 1050° C to dissolve primary γ' and then water quenched and subsequently aged at 760°C for 25 hours to produce a fine dispersion of uni-modal γ' precipitates. From earlier work, it is known that the Co and Cr preferentially segregate to the matrix material [6]. The Al, Nb, Ti, and Ni elements segregate to the ordered γ' . Samples were cut and polished to produce TEM foils with a 50-nm thickness. The samples were imaged on a Technai FEI 200-kV TEM using a Gatan Imaging Filter. Previous work found that the Chromium edge in EFTEM images provided the best gamma prime precipitate contrast for quantifying precipitate sizes and area fractions [12]. In contrast to that work, this work uses 30 precipitates from Cr edge EFTEM images to find the optimum parameters for an automated segmentation technique.

Figure 3.4.1 shows images of eight secondary (1-8) and eight tertiary (9-16) γ' precipitates extracted from EFTEM images that were slow cooled. Several problems with segmenting the γ' precipitates are apparent from Figure 3.4.1, *e.g.*, the morphology of the secondary precipitates, the changes in intensity within the precipitates, the intensity gradient at the boundaries, and a low level of noise. Some of the intensity changes within the secondary precipitates are typically due to a low volume fraction of the precipitate within the thin film, *i.e.*, during preparation, the TEM foil barely sliced through the precipitate in some locations (*e.g.*, the upper right corner of the precipitate in image 3). While the tertiary precipitates are all spherical in shape, the particles selected included some precipitates that would be difficult to manually segment (*e.g.*, image 15) and even some overlapping particles (*e.g.*, image 16).

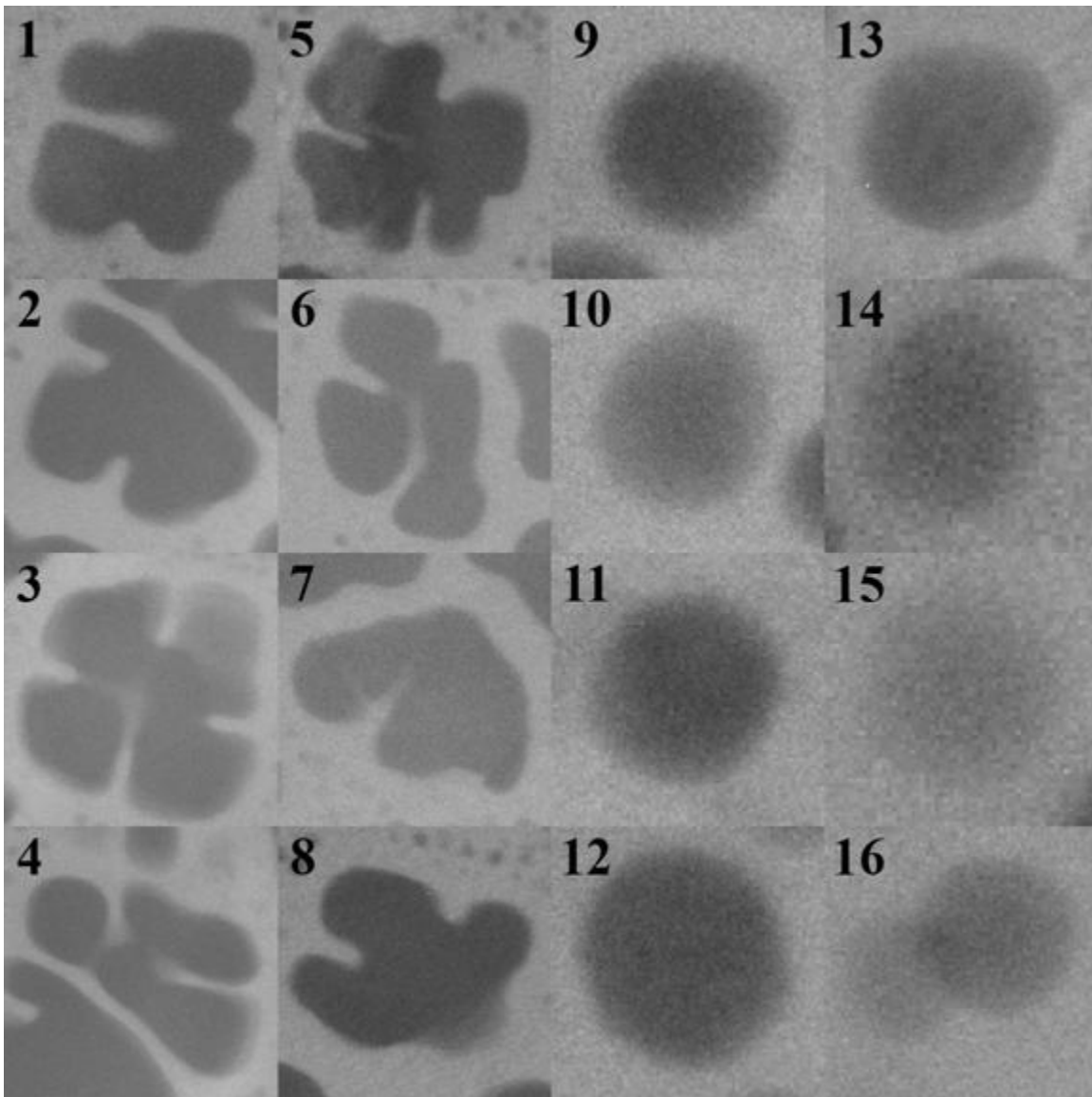


Figure 3.4.1. Images showing the variations in precipitate morphology for primary (1-8) and secondary (9-16) γ' precipitates.

AUTOMATED SEGMENTATION METHODOLOGY

While classical image processing techniques [13, 14] for segmenting image data have certain advantages, there are some limitations of using these techniques as well. For instance, a classical approach to image processing consists of two steps [15]: (1) an enhancement step, in which the intensity difference between the features of interest and the background are amplified through the application of filters and transforms, and (2) a segmentation step, in which the features of interest are extracted from the subsequent image. As Simmons and colleagues [15] point out, it

is unrealistic to expect one segmentation technique to work on the vast number of materials microstructures. Here, we have used the region growing process to segment the γ' precipitates. Region growing algorithms are widely used in medical imaging applications [e.g., 16-18] and should have the ability to even segment γ' precipitates in EFTEM images with poor contrast.

Region growing is a fundamental segmentation technique in image processing [13, 14]. The basic procedure for region growing is to start with a “seed” point and grow the region by adding neighboring pixels that have properties similar to the seed (e.g., similar intensity). The region grows based on a similarity criteria and stops growth when no more neighboring pixels satisfy this criteria. For example, the growth criterion is often based on the intensity difference between the neighboring pixel and the average intensity of the region. For this example, a threshold parameter can be used for the stopping criterion; when the intensity difference for all neighboring pixels is above this threshold, growth of the region stops. This “naïve” method can be used to segment the γ' precipitates, but with a few disadvantages:

1. The perimeter of the segmented particle can be very rough due to inherent noise within the image. In reality, though, the surface energy of the γ' precipitates will act to minimize the region perimeter. While median or Gaussian filters can be used to reduce the noise within the EFTEM images, these methods will also blur the edges of the particle, making it difficult to accurately segment the particle boundaries.
2. The threshold parameter used for a stopping criterion may need to be changed to accurately segment different particles. Additionally, this threshold parameter may not be obvious based on visual observation of the region boundary, *i.e.*, the precipitate interface has a gradual intensity slope and multiple threshold parameters may appear to approximate the region boundary.

We addressed these disadvantages to create a fully automated region growing technique for segmenting the γ' precipitates. First, to discourage non-spherical growth with the region growing technique, the addition process was modified to include a weighting factor that is a function of the local density of region pixels. To implement this, the intensity difference is calculated for each pixel neighboring the region. However, instead of adding the pixel with the closest intensity value, the intensity difference for each pixel is multiplied by a weighting factor function and the pixel with the lowest value is added. In this research, the weighting factor function is given by

$$w(n) = \text{ceil}\left(\frac{e^c}{e^n}\right),$$

where n is the number of neighbors belonging to the region in a local neighborhood centered around each pixel and the constant c normalizes the weighting function so that the value of $w(c)=1$. The ceiling function is used so that only pixels with a number of neighbors below c are adversely weighted. By multiplying this weighting function by the intensity difference for each pixel, this places a lower probability of adding a pixel surrounded by a small number of pixels belonging to the region.

Second, the stopping criterion of the “naïve” region growing was automated to select a threshold parameter for each precipitate in an unsupervised manner. This is accomplished by incrementally increasing the threshold parameter for the region growing algorithm and finding the threshold parameter that maximizes a penalty function. In this work, the penalty function is the intensity difference between mean intensities from the “inner” and “outer” regions. For instance, the “inner” region can represent all pixels within the region and the “outer” region can represent the bordering pixels just outside the region. The critical threshold parameter maximizes the penalty function and results in the optimum segmentation for the precipitate.

Figure 3.4.2 illustrates how the automated stopping criterion works for a typical γ' precipitate. First, Figure 3.4.2(a) shows the region size (pixels) as a function of the threshold parameter selected for a seed point within the γ' precipitate. The size of the region increases as the threshold parameter increases, as shown in the accompanying images (where the perimeter pixels for the segmented γ' precipitate is shown in red on the original image). After a period of fast growth to the boundary, further increases in the threshold parameter result in only minor increases to the region size. This illustrates the difficulty with choosing a threshold parameter based on visual observation alone. With only minimal changes to the region size for higher threshold parameters, at what threshold is the particle accurately segmented?

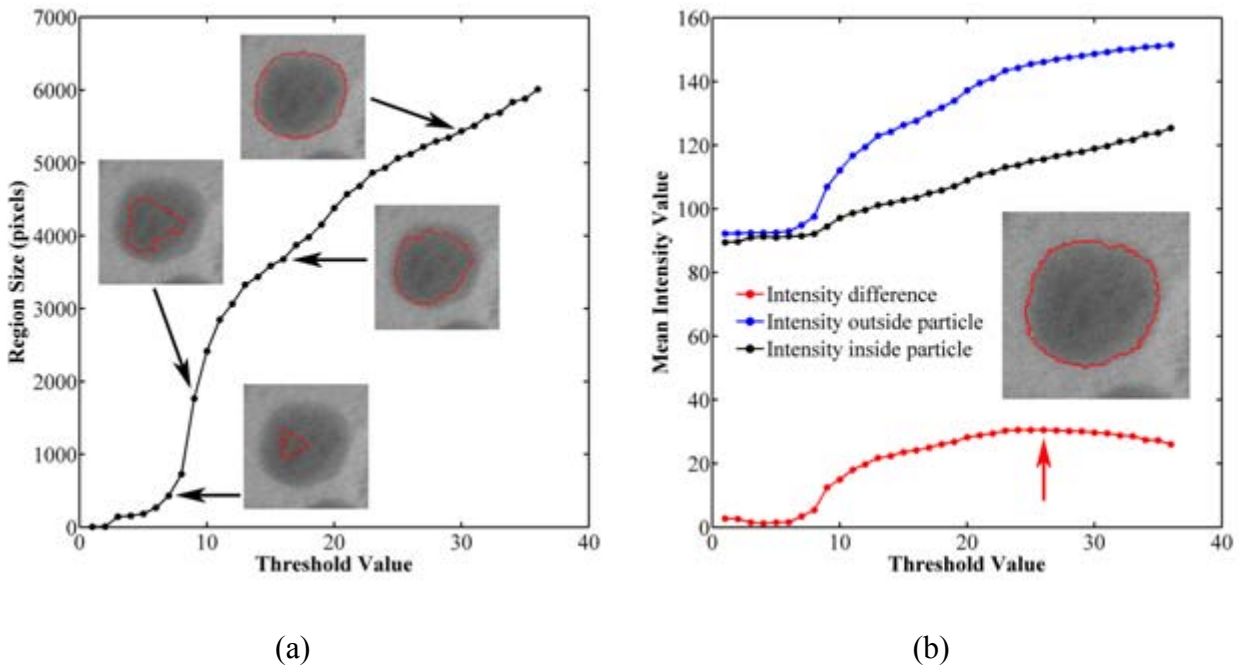


Figure 3.4.2. (a) Plot showing the region size as a function of the stopping threshold parameter. (b) Plot showing the mean intensity for the region, the area just outside the region, and the intensity difference between the two areas as a function of the stopping threshold parameter. The arrow and image correspond to the region with the maximum intensity difference, which is used for the automated region growing stopping criterion.

To answer this question, Figure 3.4.2(b) shows the mean intensity of the region, the mean intensity of the neighboring pixels, and the intensity difference between these two areas as a function of the threshold parameter for the same γ' precipitate. Recall that the maximum intensity difference (red) is the stopping criterion. For small threshold parameters, the intensity of the area outside the region is approximately equivalent to the intensity of the area inside the region, *i.e.*, many of the pixels outside the region belong to the γ' precipitate. The abrupt increase in the intensity difference coincides with the region growing near the precipitate interface, as can be seen in Figure 3.4.3(a). Again, recall that the optimum segmentation of the γ' precipitate is defined as the threshold parameter that yields the maximum intensity difference between these two areas, as denoted by the red arrow. In this automated manner, this routine quantitatively delineates the γ' precipitate interface based on the intensity gradient across the interface. The image in Figure 3.4.3(b) shows the original image with the perimeter pixels for the segmented γ' precipitate in red.

There are several potential parameters that could be used to tune the results of the region growing algorithm. For instance, the calculation of the intensity difference requires a border width (pixels) used for calculating the mean intensity of the outer region. Additionally, the calculation of the region's mean intensity can use pixels from the entire region or just pixels from the outer border of the region. Moreover, the local density weighting function contains two parameters: the constant c and the size of the local neighborhood ($m \times m$). These parameters will be investigated next. A combination of both visual inspection and quantitative comparison of the intensity difference for different segmented particles will be used to find the optimum parameters for segmenting secondary and tertiary γ' precipitates from EFTEM images.

SEGMENTATION OPTIMIZATION RESULTS

Influence of intensity difference calculation

The first parameter that was investigated was the width of the border just outside the region. Multiple gamma prime precipitates were segmented using seven different widths (in pixels): 1, 2, 3, 4, 5, 6, and 7. Additionally, the mean intensity of the region was calculated using (i) the entire region and (ii) the outer boundary layer of the region. For these calculations, the values of the local density weighting function parameters were $c = 9$ and $m = 5$. Figure 3.4.3 shows an example of how these factors influence the particle segmentation. For the sake of brevity, only two different widths are used along with the two methods used for calculating the region mean intensity. The numbers 2' and 7' refer to the border width in pixels, while the letters i' and ii' refer to the method for calculating the region mean intensity. From Figure 3.4.3, a few trends are apparent through visual observation and supporting quantitative results:

1. As the width of the border used for the mean intensity outside the region is increased, the segmented precipitate size decreases. However, this trend is drastically reduced or eliminated by using method ii' (the inner border) to calculate the region intensity.
2. For method i', which uses the entire region to calculate the inner mean intensity, the stopping criterion misses the precipitate interface and allows the region to grow into

- the surrounding area, as evident in cases 2i and 7i. Additionally, this method does an inadequate job of capturing certain geometric features in the primary γ' precipitates (shown by red arrows).
3. For method `_ii`, which uses the outer boundary layer of the region to calculate the inner mean intensity, the stopping criterion appears to work well.

Based on these findings, method `_ii` is the optimum method for segmentation of the precipitates in this study. The width of the border has less of an influence for this method, so a width of 7 pixels will be used as the optimum border width parameter.

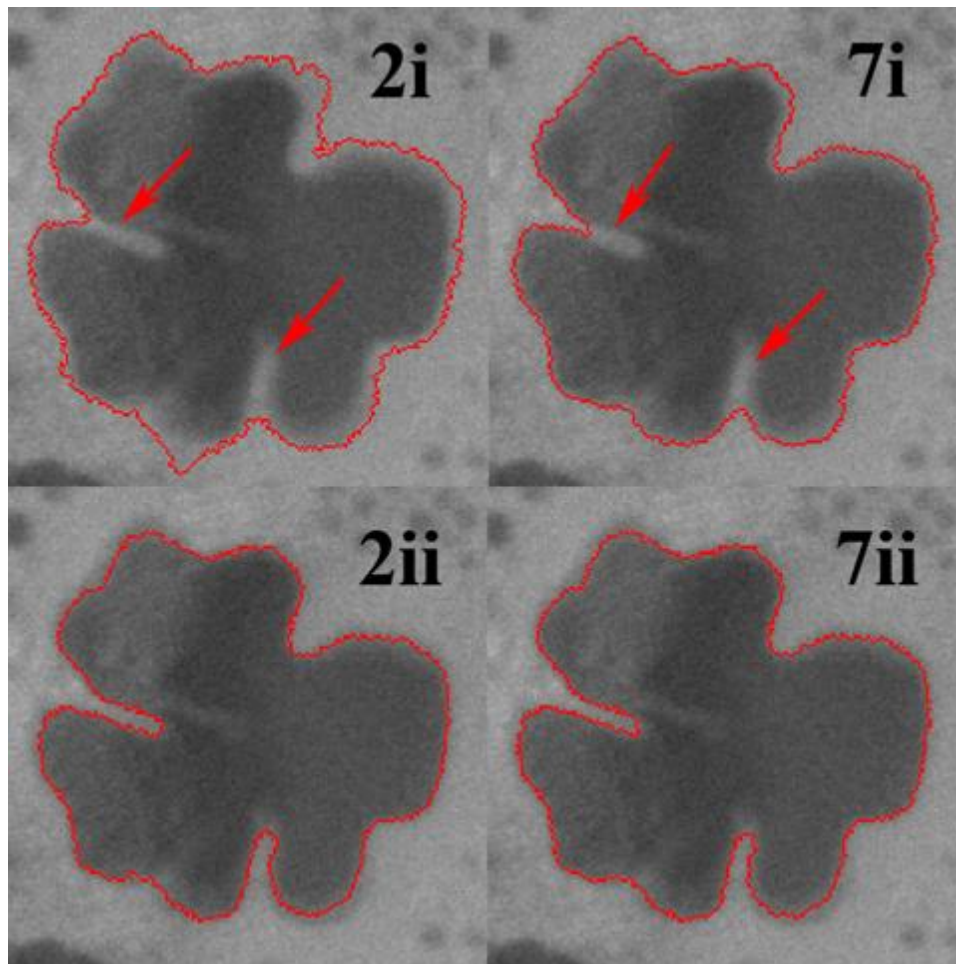


Figure 3.4.3. Images showing how the width of the border used in the mean intensity calculation and the choice of method for calculating the region mean intensity influences the segmentation of a secondary γ' precipitate. The notation refers to the border width (*i.e.*, the numbers 2 and 7 are the border width in pixels) and the two methods for calculating the region

mean intensity, *i.e.*, (i) using pixels from the entire region or (ii) just using pixels from the outer border of the region (using the same aforementioned border width).

Influence of local density weighting function parameters

The second parameter investigated was the influence of the local density weighting function. The optimum border width and method for calculating the intensity difference determined previously was used for this study. All 30 γ' precipitates were segmented using different values of m and c , which are listed in Table 3.4.1. Recall that c normalizes the weighting function, so that a density of region pixels equal to or greater than c within the $m \times m$ local neighborhood is not adversely weighted. Therefore, the parameter value of $m/c = 3/1$ does not adversely weight any pixels (*i.e.*, the local density weighting function does not influence the region growing technique, $w(n) = 1$ for all pixels). Table 1 lists the average percentage change (rounded to the nearest percent) in area and perimeter for the 15 secondary and 15 tertiary γ' precipitates for the m/c parameter combinations. The percentage change in area and perimeter is calculated by comparing the statistics for the m/c combination of each precipitate with those of the $m/c = 3/1$ combination. The weighting function parameters have little effect on the precipitate area, but a large effect on the perimeter measurement for the γ' precipitates. The precipitate perimeter decreases as c is increased for a fixed neighborhood size (m).

Table 3.4.1. The percent change in the area, perimeter, and equivalent diameter measurements for the secondary/tertiary γ' precipitates when compared to region growing unbiased by the weighting function ($m/c = 3/1$).

m	c	Secondary γ' Area Change	Tertiary γ' Area Change	Secondary γ' Perimeter Change	Tertiary γ' Perimeter Change
3	1	Segmentation is unbiased by local density weighting function			
3	2	0	+ 1%	-8 %	-17 %
3	3	0	+ 2%	-14 %	-26 %
3	4	- 1%	0	-27 %	-39 %
3	5	-1%	+ 1%	-28 %	-40 %
5	3	0	0	0	-2 %
5	5	0	0	-2 %	-6 %
5	7	0	0	-5 %	-14 %
5	9	0	+ 2%	-11 %	-25 %
5	11	-1%	0	-26 %	-39 %
7	5	0	0	0	0
7	9	0	0	0	-2 %
7	13	0	0	-2 %	-6 %
7	17	0	+ 1%	-7 %	-17 %
7	21	0	+ 1%	-17 %	-32 %

Figure 3.4.4 illustrates how the m/c parameters influence the segmentation of a tertiary γ' precipitate. The perimeter of the segmented region is shown by red pixels on the original intensity image. First, the region starts to grow in a faceted manner as m/c^2 approaches 0.5 (images at the far right in Figure 3.4.4). This growth is due to the region growing algorithm adversely weighting all pixels that do not have at least 50% of their pixels in a local neighborhood, *i.e.*, the growth is dominated more by local density of region pixels than the intensity of the added pixels. This type of growth is inadequate for capturing the morphology of the precipitates. Moreover, for low values of c , the region can grow in a fingering manner with a jagged interface (*i.e.*, low percentage change in the perimeter lengths in Table 3.4.1). Therefore, a high value of c is ideal for growing a region with a smooth interface (compared to low c values) as long as faceted growth is avoided. From this analysis, the optimum parameters for region growing are m/c values of 5/9 or 7/21.

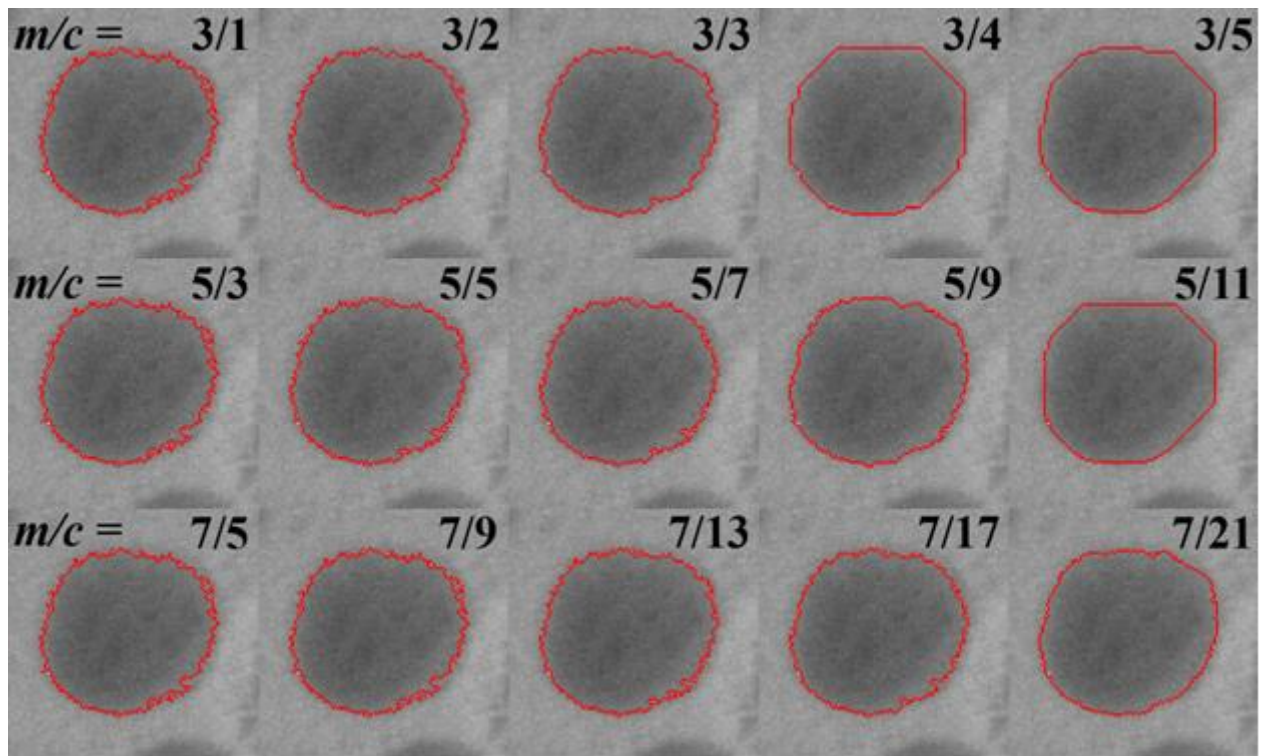


Figure 3.4.4. Images showing the influence of the local density weighting function parameters on the segmentation of a tertiary γ' precipitate. The parameters c and m refer to a normalization constant c for the weighting function and the size of the local neighborhood ($m \times m$), respectively.

Influence of initial seed location

The third area to be investigated is the initial location of the seed point. In the previous examples, the lowest intensity (darkest) pixel within the precipitate was selected as the seed point. Based on the initial segmentation using the lowest intensity pixel, 250 random pixels within the precipitate were selected as starting seed points. The optimum parameters determined previously were used for this study. After all 250 regions were grown, the statistics were analyzed.

Figure 3.4.5 shows all of the random seed points on the original intensity image. The color of the seed points denote the area of the region grown from that seed relative to the area of the region grown from the lowest intensity pixel. Of the 250 regions, 191 of the regions were equal to (red), 38 were less than (green), and 21 were greater than (blue) the region grown using the lowest intensity seed point. The spatial location and intensity of the seed point made a difference in the final segmented region. First, seed points selected on the exterior of the precipitate have an increased chance of deviating from the segmentation produced using interior seed points. This effect is mainly influenced by the intensity difference in the interface region. For example, the region in the lower right of the precipitate in Figure 3.4.5 has a higher mean intensity (lighter) than the rest of the precipitate and is closer to the intensity of the surrounding matrix. Therefore, many of the seed points within this region had a higher or lower region area than seed points selected in the darker regions of the precipitate. Based on these findings, seed points that accentuate the intensity difference between the precipitate and the matrix should be selected for the region growing technique, *i.e.*, the darkest pixel in a dark particle or the lightest pixel in a light particle.

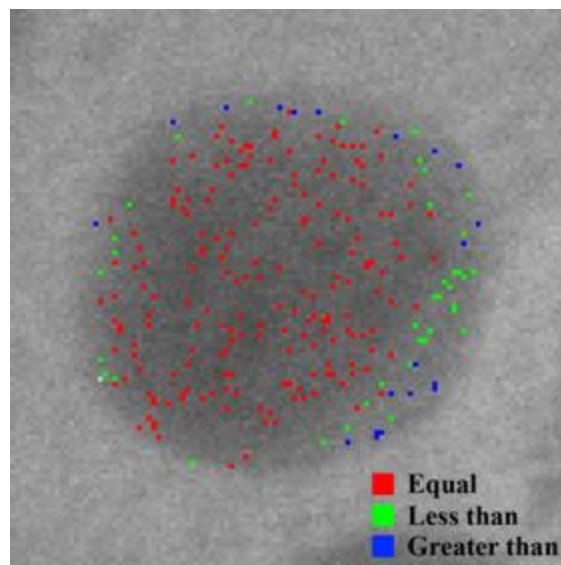


Figure 3.4.5. Images showing the intensity image of the tertiary γ' precipitate along with the 250 random seed point locations. The colors correspond to the size of the segmented region relative to the region grown using the lowest intensity (darkest) seed point.

Validation

Using the optimum parameters determined earlier, the initial precipitates were segmented using the region growing algorithm. Figure 3.4.6 shows the original precipitates from Figure 3.4.1 with the perimeter of the segmented region shown by the red pixels. For both the secondary and tertiary γ' precipitates, a visual comparison of the segmented regions with the intensity images shows good agreement. The region growing technique was even adequate at segmenting some of the more difficult precipitates, *e.g.*, secondary precipitates with complex morphologies (1, 3, 4, 5, & 6) and a high intensity contrast within the precipitate (3 & 5) as well as tertiary precipitates that had very diffuse interfaces with intensities very near to the surrounding matrix (14, 15, & 16).

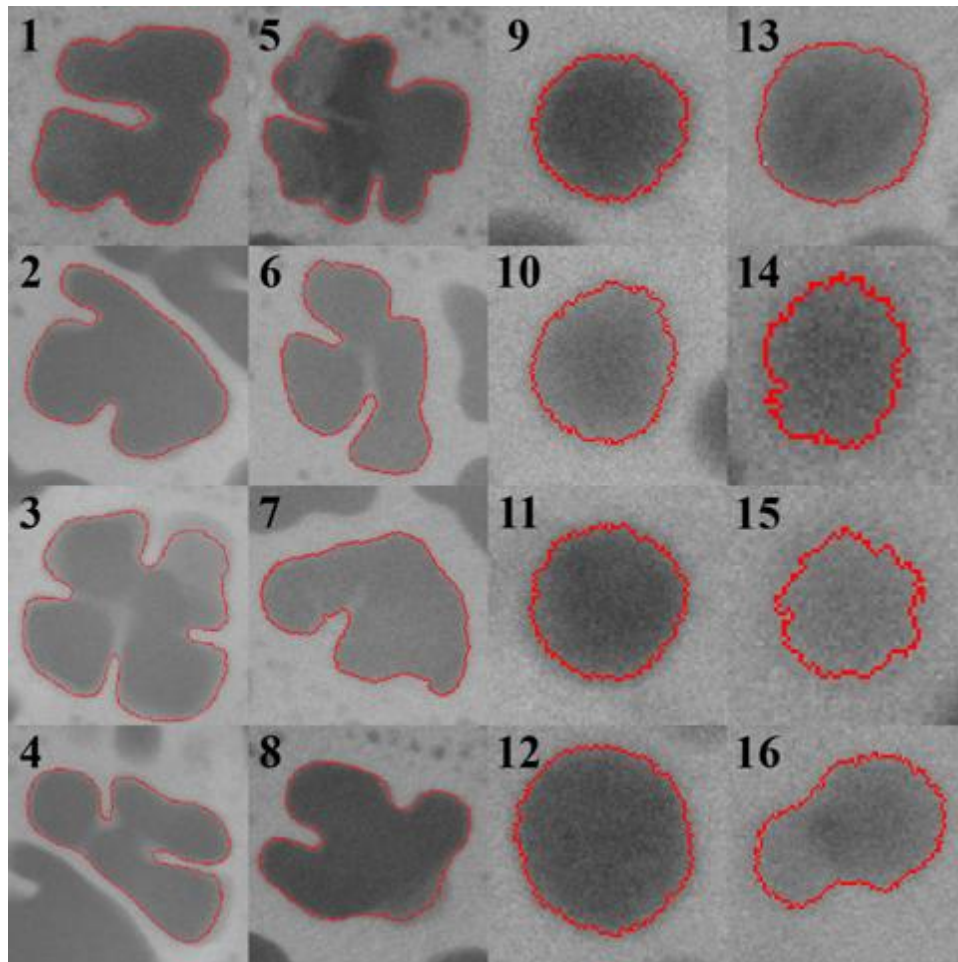


Figure 3.4.6. Images showing the segmentation of the region growing technique with the optimum parameters (border width of 7 pixels, method `_ir`, $m/c = 5/9$) for variations in precipitate morphology for primary (1-8) and secondary (9-16) γ' precipitates.

Additionally, 50 secondary and tertiary γ' precipitates were selected to compare the difference between manual and automated segmentation. All of the particles were segmented using the region growing technique with the optimum parameters. The results are shown in Figure 3.4.7, which plots the area obtained via manual segmentation against the area obtained via the region growing technique. The 45° line indicates a 1:1 correlation of the areas. The areas found with the region growing technique are, on average, 14% smaller than those same precipitates segmented manually (*i.e.*, 7% smaller equivalent diameter). The inlaid images show several secondary and tertiary γ' precipitates along with the perimeter of precipitates identified with manual (blue) and automated (red) segmentation techniques. In this instance, manual segmentation tended to capture very light intensity differences in the interface region between the γ' precipitate and the γ matrix. However, in some cases, this method may actually capture some of the γ matrix pixels as well. Moreover, the results obtained using manual segmentation are highly user-dependent. In contrast to the manual segmentation, the automated region growing technique captures the precipitate and its interface based on a quantitative metric (the intensity difference) in a reproducible manner. In the event that the region growing technique should be tuned to the manual segmentation, the penalty function can be modified.

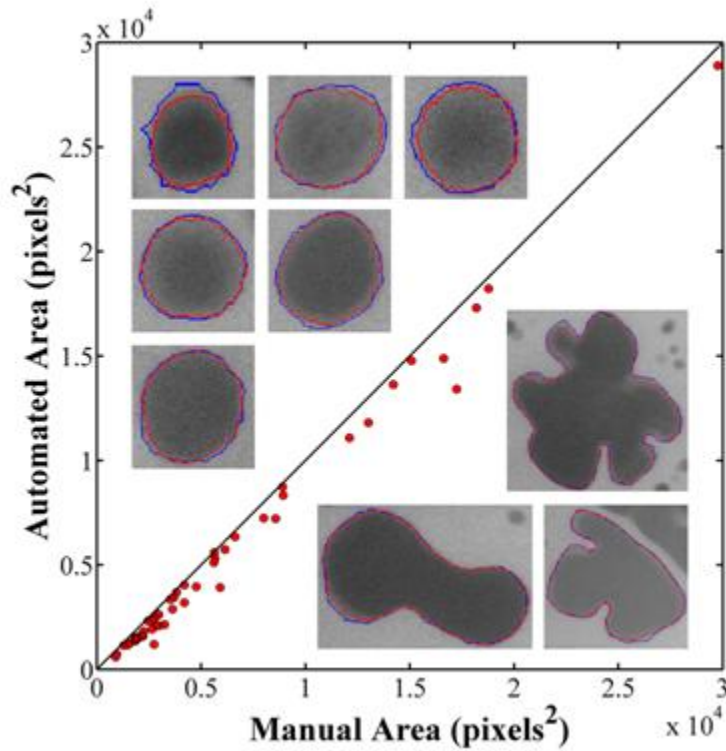
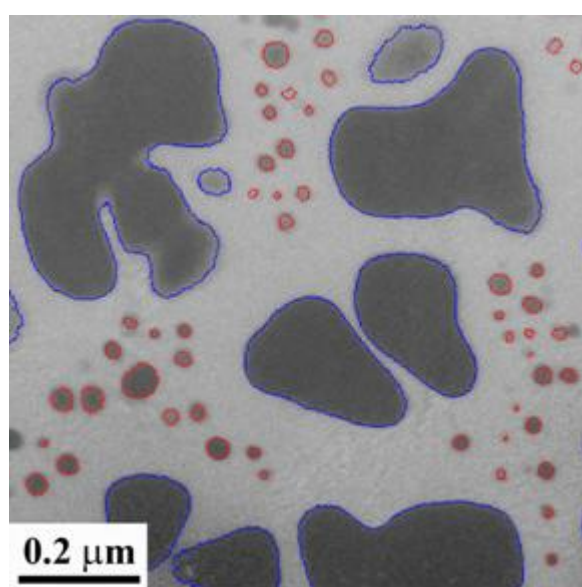


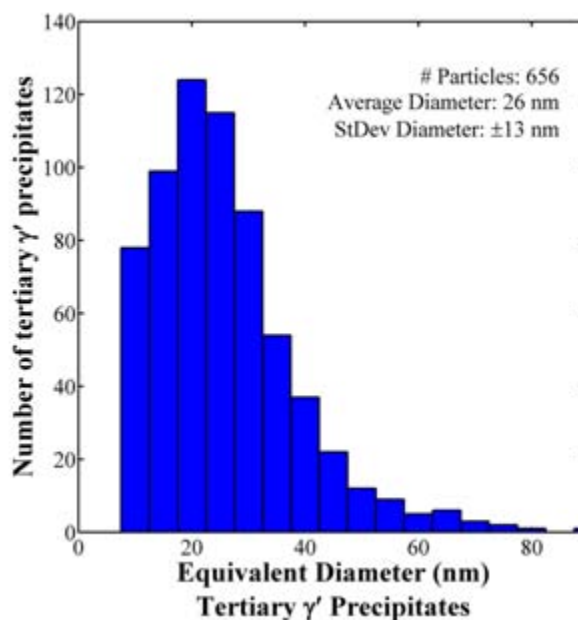
Figure 3.4.7. Plot comparing the area of 50 manually segmented precipitates versus the area of these same precipitates segmented with the region growing algorithm. The images show examples of some of the secondary and tertiary precipitates with the perimeter of the manually and automated precipitates shown in blue and red, respectively.

PRECIPITATE STATISTICS RESULTS

The secondary and tertiary γ' precipitates can now be segmented using the automated region growing technique to extract microstructural statistics from the EFTEM images. Eight EFTEM images from a sample that was slow cooled after aging for 200 hours were examined because of the presence of both secondary and tertiary γ' precipitates within the microstructure. Figure 3.4.8(a) shows an example of one of the original intensity EFTEM images with the perimeters of the segmented secondary and tertiary γ' precipitates in blue and red, respectively. A number of microstructural statistics (*e.g.*, area, equivalent diameter, perimeter, etc.) can now be extracted from the segmented precipitates. Figure 3.4.8(b) shows an example of the distribution of equivalent diameters (nm) for the 656 tertiary γ' precipitates segmented from these images. The equivalent diameter for the tertiary γ' precipitates was chosen as an example statistic, because most of the tertiary γ' precipitates are spherical for this processing condition (unlike the secondary γ' precipitates). On average, the tertiary γ' precipitates have an equivalent diameter of 26 nm and the distribution is lognormal. For this microstructure, the secondary γ' precipitate statistics are not easily obtained since unconnected segments of secondary γ' precipitates within the EFTEM image can actually be part of the same secondary precipitate. Several examples of this can be observed within Figure 3.4.8(a). Therefore, a distribution of equivalent diameter for the secondary precipitates is not shown here; care should be used when using 2D statistics to describe 3D precipitates of complex morphology.



(a)



(b)

Figure 3.4.8. (a) Intensity image with segmented secondary (blue) and tertiary (red) γ' precipitates using the automated technique. (b) Histogram assembled from multiple EFTEM images, which shows the distribution of equivalent diameters (nm) for 656 tertiary γ' precipitates. The average equivalent diameter is 26 nm \pm 13 nm.

Another characteristic statistic that can be directly tied to the processing history of the microstructure is the nearest neighbor distances between precipitates. Again, the nearest neighbor distances between secondary γ' precipitates from 2D images are skewed in that they may not represent the closest distance between precipitates, but rather the closest distance between branches of the same precipitate (see Figure 3.4.8(a)). Of particular interest is the nearest neighbor distance between the secondary and tertiary γ' precipitates. For each tertiary γ' precipitate, the distance to the nearest secondary γ' precipitate was calculated. Here, the distance is calculated as the minimum distance from the segmented boundary of the tertiary precipitate to the boundary of the secondary precipitate. Figure 3.4.9 shows the distribution of nearest neighbor distances for the 656 tertiary γ' precipitates. The average nearest neighbor distance was 94 nm. Taking into account the average equivalent diameter of the tertiary γ' precipitates, the average distance to the centroid of the tertiary precipitate (ideally where nucleation begins) is approximately 107 nm.

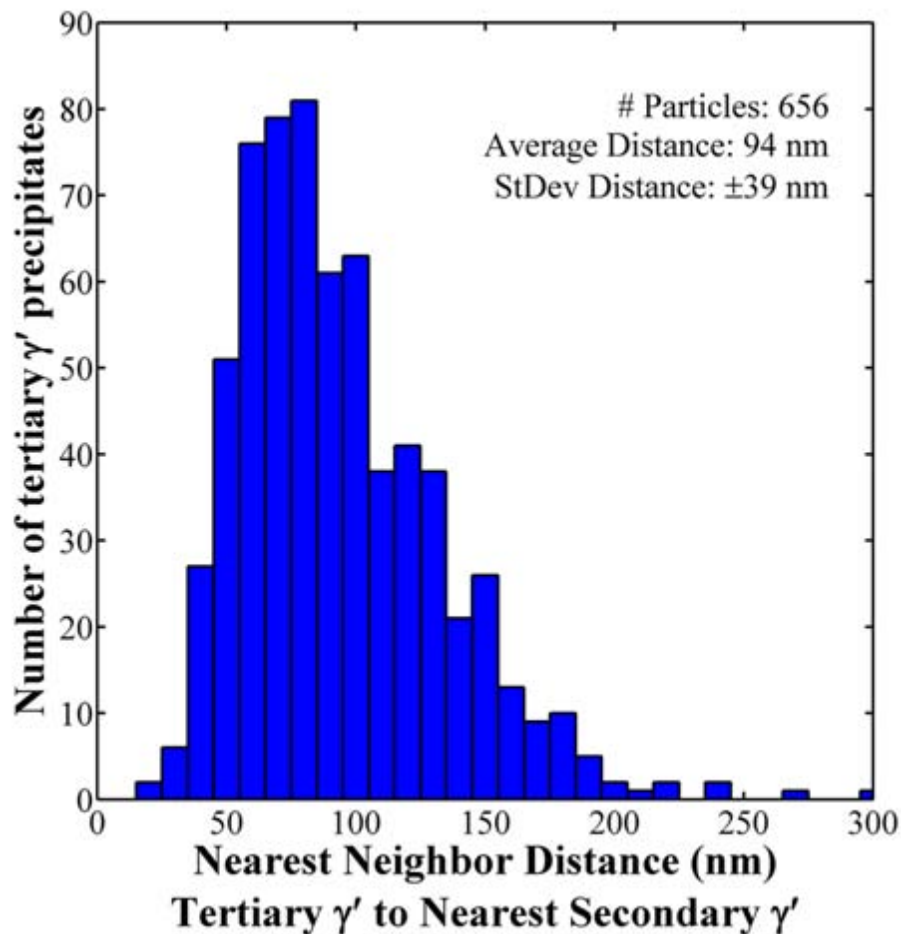


Figure 3.4.8. Histogram showing the distribution of nearest neighbor distances (nm) for 656 tertiary γ' precipitates to the nearest secondary γ' precipitates. The average nearest neighbor distance is 94 nm \pm 39 nm.

Interestingly, the distribution also quantitatively captures several effects within the microstructure. First, the low occurrence of tertiary precipitates within 50 nm of the secondary precipitates (~8%) reflects that there is a zone around the secondary precipitates in which tertiary precipitates do not grow. This may result from the segregation of elements within the vicinity of the boundary [6, 10]. The width of this zone has important implications for Ni-based superalloys, because the spatial distribution of γ' precipitates impacts the overall mechanical properties.

Second, the highest or extreme value of the nearest neighbor distance (306 nm) may indicate the spacing of the secondary γ' precipitates. That is, there are no tertiary γ' precipitates greater than this distance because within a certain distance from the nearest secondary precipitate (~612 nm) the chemical composition is adequate for another secondary γ' precipitate to form. In this respect, the extreme value statistics of the nearest neighbor distances can give some insight into the maximum spacing of secondary γ' precipitates. In previous work, the distances between precipitates have been calculated using the equivalent diameter of the precipitates. Clearly, considering the tortuous morphology of the secondary γ' precipitates, the present technique for measuring nearest neighbor distances provides a much more accurate estimation of these distances, as well.

The ability to gather statistical information on both secondary and tertiary precipitates provides a great tool for the modeling community that has relied heavily on limited analysis of small particle populations. This has been driven by the labor-intensive manual techniques used to segment images with difficult intensity gradients across particle boundaries. The future of characterizing γ' precipitates in Ni-based superalloys relies not only on better techniques for imaging, but also better techniques for segmenting large numbers of γ' precipitates in an automated manner.

Conclusions

In this work, we discuss a computational methodology for automated detection of secondary and tertiary γ' precipitates in energy filtered transmission electron microscopy (EFTEM) images. Several important parameters for the automated region growing technique were investigated using a combination of visual inspection and intensity information from the EFTEM images. These parameters were related to the method used for calculating the stopping criterion, the local density weighting function, and the seed point selection method. After optimizing these parameters, the microstructural statistics obtained from the γ' precipitates segmented with the automated technique were compared with the same precipitates segmented manually. On average, the results show that the precipitate area (equivalent diameter) obtained using the automated technique is approximately 14% (7%) lower than that of the same precipitates segmented manually. The automated region growing technique presented here is suitable for detecting secondary and tertiary γ' precipitates of complex morphology and varying intensity contrast in a reproducible manner.

This technique was then used to segment the secondary and tertiary γ' precipitates from EFTEM images of a single crystal nickel-based superalloy that was slow cooled after aging for 200 hours.

The segmented precipitates were used to calculate average/extreme microstructural statistics for this processing condition. In addition to calculating the distribution of tertiary precipitate equivalent diameters, the distribution of distances from 656 tertiary precipitates to the nearest secondary precipitates was calculated. The extreme values of the distribution shows that the majority of tertiary γ' precipitates are located greater than 50 nm and less than 300 nm from the secondary γ' precipitate surfaces for this processing condition. The significance of this technique is its ability to automate segmentation of precipitates in a reproducible manner for acquiring microstructure statistics that relate to both processing and properties.

References

- [1] Reed R.C., *The Superalloys Fundamentals and Applications*, (Cambridge, UK, Cambridge University Press, 2006).
- [2] Telesman J., Kantzos P., Gayda J., Bonacuse PJ, Prescenzi A., Superalloys 2004, Warrendale PA, TMS Publications (2004), p.215.
- [3] Stoloff N.S., Superalloys II, New York, John Wiley (1987) p. 61.
- [4] Sondhi SK., Dyson BF, and McLean, Acta Materialia, Vol 52 (2000) p. 1761.
- [5] Fahrman M., Hermann W., Fahrman E., Boegli A., Pollock T.M., and Sockel H.G., Mater. Sci and Eng., A271 (1991) p. 122.
- [6] Tiley J., Viswanathan G.B., Srinivasan R., Banerjee R., Dimiduk D.M., and Fraser H.L., Acta Materialia, Vol 57 (2009) p. 2538-2549.
- [7] Tiley J., Searles T., Lee S., Kar S., Banerjee R., Russ J.C., Fraser H.L., Mat. Science and Eng A, 372 (2004) p. 191-198.
- [8] Collins P.C., Welk B., Searles T., Tiley J., Russ J.C., Fraser H.L., Mat. Science and Eng A, 508 (2009) p. 174-182.
- [9] Viswanathan G.B., Sarosi P.M., Henry M.F., Whitis D.D., Milligan W.W., and Mills M.J., Acta Materialia 53 (2005) p. 3041.
- [10] Sarosi P.M., Viswanathan G.B., Whitis D.D., Mills M.J., Ultramicroscopy 103 (2003) p. 83.
- [11] Little Jr. J.W., Pettie R.G., Schirra J.J., Cowles B.A., Holmes R.A., Russ S.M., Materials damage prognosis, Warrendale PA, TMS Publications (2005) p. 23.
- [12] Srinivasan R., Banerjee R., Hwang J.Y., Viswanathan G.B., Tiley J., Dimiduk D.M., Fraser H.L., Physical Review Letters 102 (2009) 086101.
- [13] Russ, J.C., *The Image Processing Handbook*, 5th Edition (Boca Raton, FL, CRC Press, 2007).
- [14] Gonzalez, R.C., Woods, R.E., *Digital Image Processing*, 2nd Edition (Upper Saddle River, NJ, Prentice-Hall, 2002).
- [15] Simmons, J.P., Chuang, P., Comer, M., Spowart, J.E., Uchic, M.D., De Graef, M., MSMSE 17 (2009) 025002.
- [16] Law, T.S., Heng, P.A., Medical Imaging 2000: Image Processing, Kenneth Hanson (Editor), Proceedings of SPIE, 3979 (2000) 906-916.
- [17] Pohle, R., Toennies, K.D., Medical Imaging 2001: Image Processing, Milan Sonka, Kenneth Hanson (Editor), Proceedings of SPIE, 4322 (2001) 1337-1346.
- [18] M. del Fresno, M. Vénere, A. Clausse, *Computerized Medical Imaging and Graphics*, 33 (2009) 369-376.

3.5. Multiscale characterization of orthotropic microstructures

Computer-generated 2D microstructures of varying second phase area fraction (5–30%), aspect ratio (1–16) and degree of alignment (where the reinforcement major-axis orientation is random, perfectly aligned or semi-aligned) are analyzed via the isotropic and directional forms of the computationally efficient multi-scale analysis of area fractions (MSAAF) technique. The impact of these microstructure parameters on the representative volume element (RVE) necessary to characterize a microstructure is ascertained with variations in isotropic and directional homogeneous length scales, derivative quantities of the MSAAF technique. Analysis of these results produces empirical expressions for the directional homogeneous length scale as a function of area fraction and aspect ratio for the limiting cases of random and ‘perfect’ second phase alignment. Generally, particle alignment is observed to increase the aspect ratio of a microstructure’s RVE—a trend amplified by higher reinforcement aspect ratios and lower area fractions. Particle alignment also decreases the absolute size of such an element by reducing the directional homogeneous length scales transverse to the axis of alignment. Periodic boundary conditions on the perimeter of the synthetic microstructures are used to characterize the error in the MSAAF technique via multiple instantiations of the same microstructure, which further indicates that the statistical variation in the directional homogeneous length scale (measured by the directional MSAAF technique) can be an order of magnitude less than the variation in the isotropic homogeneous length scale (measured by the isotropic MSAAF technique).

INTRODUCTION

When assessing structure–property relationships for various materials, it is necessary to define a representative length scale or volume element for characterization or simulation to avoid misleading predictions of macroscopic deformation or transport behavior. Likewise, a model or material sample must have sufficient resolution to capture the phenomena of interest. Ideally, a component-sized material model or sample should have the highest resolution possible; however, practical limitations on experimental and computational resources bound the extent and resolution of material models.

The balance between these two often competing needs of extent and resolution has been an underlying theme of numerous studies regarding characterization of heterogeneous materials. Researchers have focused on developing techniques for determining representative length scales for the extent of microstructures based on area fraction or volume fraction [1–4]; such approaches have shown sensitivity to microstructure clustering and, in fact, are excellent metrics for characterizing this property. The inverse problem of segmenting a microstructure to varying length scales (homogenizing) has also been pursued as a route for identifying the critical length scale at which macroscopic properties are controlled by shorter length scale features; these features are often associated with second phase clustering, its absence, or contribution to percolation [5–8]. In fact, recent advances in multi-scale modeling have emerged due to the ability to homogenize some regions while considering the local behavior in others; such

techniques incorporate various length scales associated with the microstructure and its local properties in their formulation [9, 10].

The correlation between critical length scales in the microstructure and the inherent mechanical behavior of heterogeneous microstructures has been examined in numerous computational and experimental studies. For example, Spowart [11] predicted that clustering of reinforcement particles in an Al–27.5%SiC metal–matrix composite has a noticeable effect on the yield strength and an even stronger effect on strain hardening, even though the same level of clustering has only a weak effect on the elastic modulus. These results indicate that each aspect of mechanical behavior is controlled by a different representative length scale in the microstructure and, consequently, that representative volume elements (RVEs) of increasing size were necessary to characterize elastic modulus, yield strength and strain-hardening, respectively. Additionally, Borbely *et al* [2] measured the local volume fractions in an Al–20%Al₂O₃ metal–matrix composite through 3D microtomography to define a microstructure correlation length and, hence, a geometric RVE for this material. Further simulations of elastic and plastic behavior with various window sizes showed that the RVE necessary to obtain accurate effective plastic properties was approximately twice the size of the RVE needed to obtain equally accurate effective elastic properties. Moreover, the influence of second phase distribution on damage accumulation and fracture has also been characterized by numerous authors in various materials, *e.g.* [12–14]. In their seminal work on crack deflection around second phase inclusions in a brittle matrix, Faber and Evans analyzed and experimentally verified that a clustered second phase distribution—as defined by a divergence from a uniform distribution for a given volume fraction—significantly increased fracture resistance in ceramic–matrix composites by increasing the degree of crack deflection and crack twist [12, 13]. The clustering of particles is associated with a critical length scale for fracture. In experiments relating to ductile fracture, Wilks analyzed second phase inclusions in a ductile matrix and found that deformation processing decreased the size of the RVE in an Al–25%SiC composite; the smaller RVE correlated with (i) an increase in interparticle separation due to cluster breakdown, (ii) a larger length scale with respect to the ductile fracture process and (iii) a substantial increase in fracture toughness [14]. Finite element simulations of microstructure domains reconstructed from experimental images of multi-phase materials have also provided insight into plasticity, damage evolution and the fracture process [15–19]. In all of these experiments and simulations, the length scale of the underlying microstructure plays a commanding role in the mechanical behavior of the material.

Therefore, it is important to have a consistent methodology for characterizing the critical length scales within heterogeneous materials. The focus of this work is the effect of second phase anisotropy on critical length scales and the corresponding RVE size. Orthotropic (aligned) microstructures are very common in materials where deformation processing has been imposed or directional synthesis routes have been pursued [14]. These microstructures constitute a sound basis for analyzing limiting bounds on anisotropic length-scale effects. Moreover, such microstructures represent a basis for analyzing microstructures with several preferred directions of alignment (*e.g.* precipitated microstructures with preferred orientation relationships) or more generalized anisotropy. In this work, we investigate the interaction between length-scale effects and second phase orthotropy through applying the isotropic and directional forms of the multi-

scale analysis of area fractions (MSAAF) technique [1, 20] to computer-generated two-dimensional microstructure images containing ellipsoidal particles of varying aspect ratio, area fraction and propensity for alignment.

Methodology

Synthetic microstructure conditions

Synthetic microstructures were generated with the factors and factor levels summarized in Table 3.5.1. The four area fractions (A_f) and five aspect ratios (AR) were chosen to give a wide range and sufficiently resolved gradient in microstructure characteristics for the subsequent analyses. The orientation distributions studied include limiting conditions where all particles are aligned vertically (90°), all particles are randomly oriented (random), and an intermediary factor level ($90^\circ \pm 20^\circ$) that reflects orientations normally distributed about 90° with a standard deviation of 20° . In all, 60 distinct synthetic microstructures (conditions) were studied corresponding to the permutation of these factors.

Table 3.5.1. The test matrix for these simulations.

Factor	Factor levels				
Volume fraction	5%	10%	20%	30%	
Aspect ratio	1	2	4	8	16
Orientation distribution	90°	$90^\circ \pm 20^\circ$	Random		

Synthetic microstructure generation

Each synthetic microstructure condition was generated via a simple procedure, similar to the random sequential adsorption (RSA) technique, *e.g.* [21, 22]. First, particle dimensions (in pixels³) were calculated for each aspect ratio along with the number of particles necessary to obtain the prescribed area fraction. In order to mitigate any unintended effect of particle size distribution, particle size (area) was kept constant through successively higher area fractions; the details of this effect will be considered in future work as a subset of the more general interaction of microstructure anisotropy and particle polydispersivity. Particle orientation was then randomly sampled from the predetermined orientation distribution while the coordinates of the particle centroid were determined via a random number generator. The influence of boundary effects on particle placement was mitigated by imposing periodic boundary conditions on the vertical and horizontal edges of the microstructure domain; particles that extend beyond the image bounds were wrapped back onto the opposite side of the image. Analytic criteria were used to reject overlapping particles. Particle placement proceeded until the specified area fraction

³ In these synthetic microstructures, absolute length scale is arbitrary; since features dimensioned in pixels may seem unphysical, the reader may wish to consider a scale of 1 pixel = $1\mu\text{m}$.

was obtained. Resulting microstructures contained a minimum of 4000 particles and were of 4096×4096 pixels in extent.

Sample regions from each synthetic microstructure condition as a function of AR and A_f are depicted in Figure 3.5.1. The general influence of each considered orientation distribution on a high area fraction ($A_f = 30\%$), high aspect ratio ($AR = 16$) microstructure is shown in Figure 3.5.2. Notice in these two figures that particles with similar orientations cluster at higher area fractions and aspect ratios. This effect can be correlated with the variation in jamming threshold [23] for such microstructures and indicates that the distribution of particle centroids may not be truly random, due to the stochastic nature of particle placement.

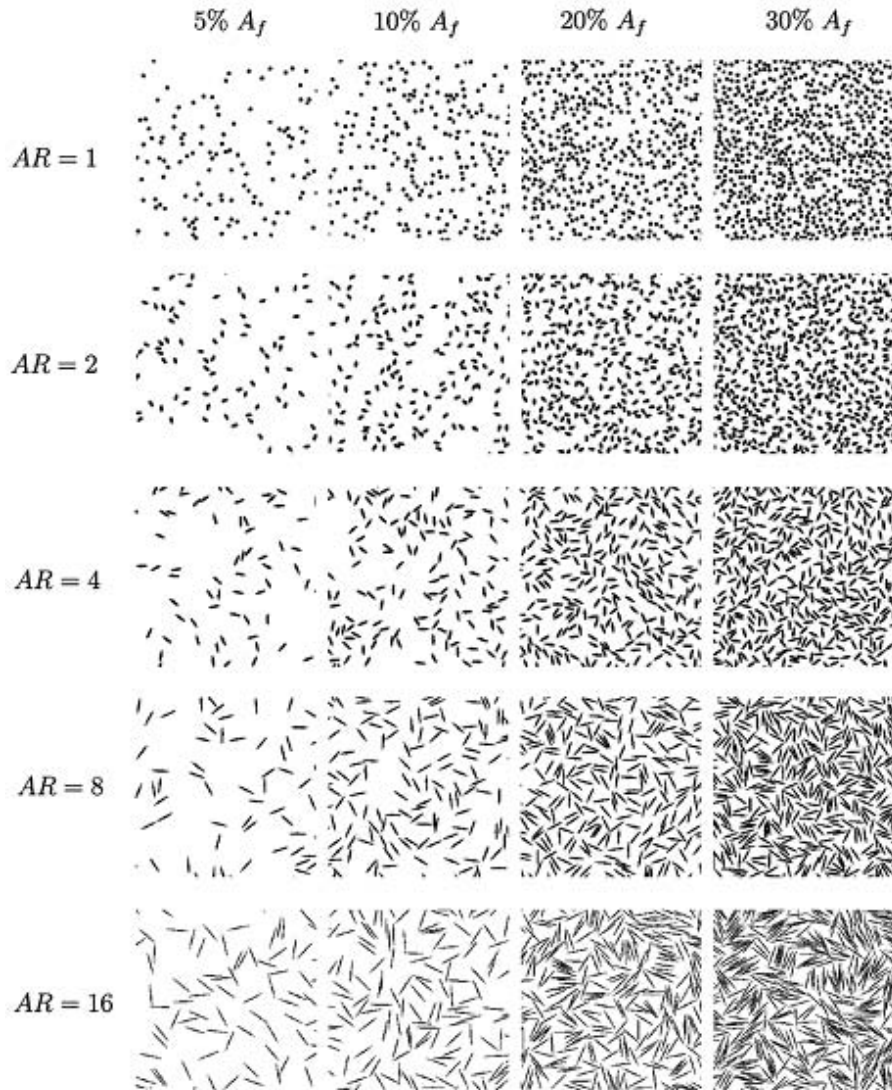


Figure 3.5.1. All synthetic microstructure conditions for randomly oriented particles displayed as a function of aspect ratio (AR) and area fraction (A_f).

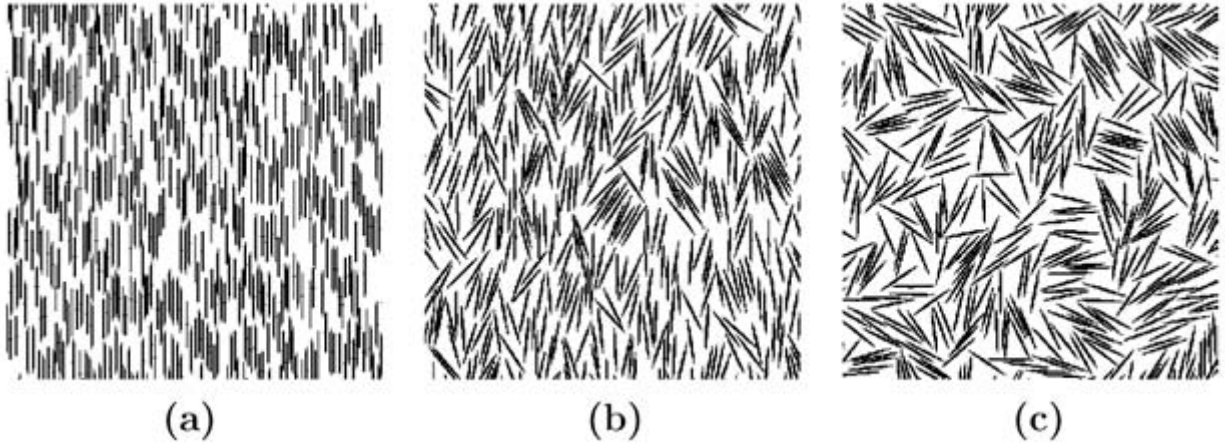


Figure 3.5.2. The influence of orientation distribution on synthetic microstructures containing 30% area fraction second phase with a 16:1 aspect ratio. The 512×512 subimages show the alignment of particles in the (a) 90° , (b) $90^\circ \pm 20^\circ$ and (c) random orientation distributions.

Multi-scale characterization

Isotropic microstructures. The homogeneous length scale (L_H) was developed to determine a representative length scale for a particular microstructure based on the variations in area fraction of a second phase as a function of length scale (Q) [1]. Qualitatively, L_H for a particular microstructure is the length scale at which the variation between each sub-region becomes statistically indistinguishable from a larger area of material. In other words, L_H is the minimum length scale necessary to construct a volume element representative of a particular microstructure to a given degree of statistical confidence, typically selected to be 99.0% in the isotropic case.

The homogeneous length scale of a real or synthetic microstructure can be quantified by a technique termed the multi-scale analysis of area fractions (MSAAF) [1]. In this method, a digitized microstructure is re-sampled at various resolutions (corresponding to various length scales, Q_n) to determine the area fraction of a particular sub-region. Take for example, the first column of images in Figure 3.5.3, where an initial microstructure is subdivided into 3 lower resolutions/length scales: Q_1 , Q_2 , Q_3 . After subdivision, the effective area fraction (A_f) is assigned to each sub-region, visually depicted as a gray level in Figure 3.5.3. By using all sub-regions available at a chosen length scale, an average area fraction and standard deviation (σ_{A_f}) in area fraction is determined for that Q_n . Though the average area fraction over all sub-regions for a particular length scale will not change with length scale, the standard deviation over all sub-regions will.

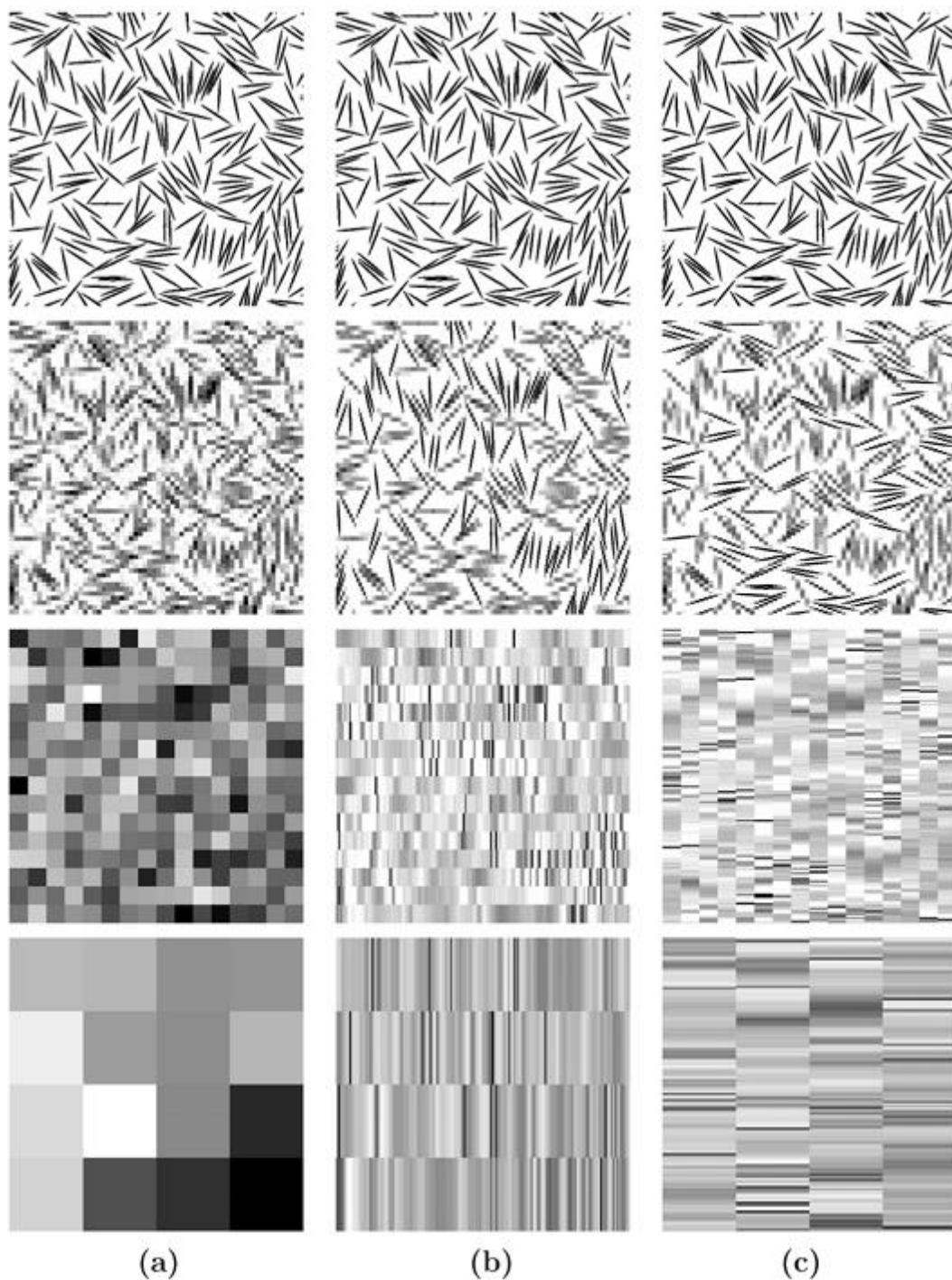


Figure 3.5.3. Evolution of the density area fraction of second phase (depicted by gray level) as a function of length scale Q according to the (a) isotropic MSAAF technique, as well as the directional technique applied in the (b) vertical and (c) horizontal directions for the synthesized 20% A_{F-16AR} microstructure.

Consequently, the principal result of this technique is a plot depicting the evolution of the coefficient of variation (ψ)—the ratio of standard deviation in second phase area fraction to the global area fraction, σ_{Af} / A_f —as a function of Q . Such a plot for the 20%A_f-16AR condition is depicted in Figure 3.5.4. When this plot decreases to a specified level of confidence (ψ), the corresponding Q is termed the homogeneous length scale (L_H). Differences in homogeneity between isotropic microstructures can be characterized using a value of L_H for each microstructure at a predetermined level of confidence [1]. For this reason, we use the isotropic MSAAF analysis of synthetic microstructures to characterize homogeneity with the 1% homogeneous length scale, $L_H(0.01)$, *i.e.* the scale at which the variation in microstructure sub-region area fraction becomes less than 1% ($\psi \leq 0.01$).

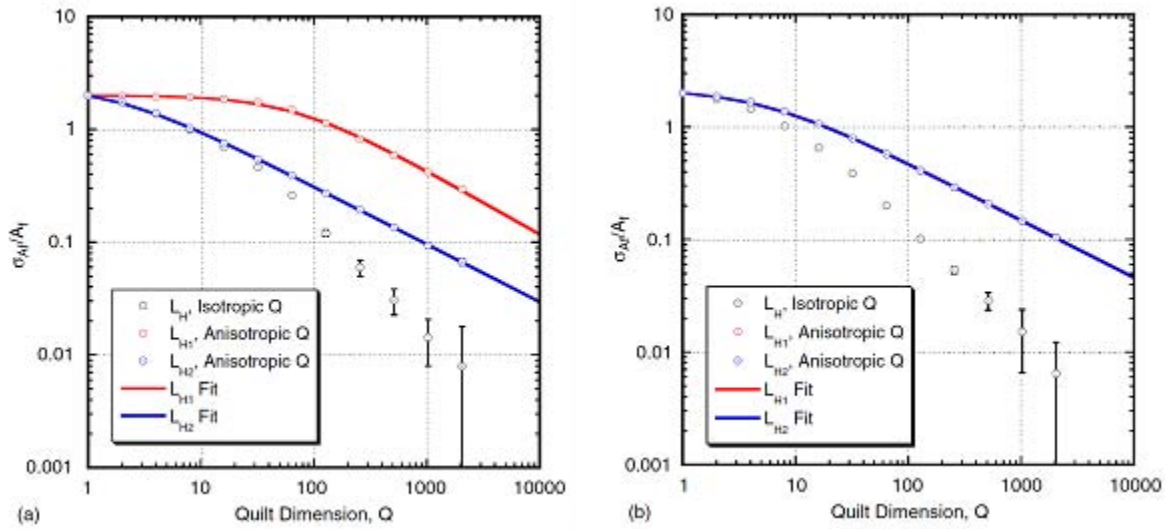


Figure 3.5.4. Isotropic and directional MSAAF plots for the synthesized 20%A_f-16AR microstructure with (a) aligned particles and (b) randomly oriented particles.

Anisotropic microstructures. When studying an area of material that is both anisotropic and inhomogeneous, it is useful to logically extend the concept of the homogeneous length scale by measuring the *directional* variation in *linear* area fraction as a function of length scale to compute a *directional homogeneous length scale*, L_{Hn} , where n is an integer index (valued from 1–3 for a three-dimensional microstructure) denoting a principal particular (orthogonal) direction in the material [20]. Only a simple modification to the MSAAF technique is required to obtain values of L_{Hn} from plane sections of a material. As shown in the second and third columns of Figure 3.5.3, rather than subdividing the microstructure into square elements, each line of pixels is subdivided into a number of strips for each corresponding length scale of interest (Q_n). The variation in area fraction of each of these strips used to generate directional MSAAF plots (also depicted for the 20%A_f-16AR in Figure 3.5.4) to determine the orthogonal 10% ($\psi = 0.1$) homogeneous length scales, L_{H1} (vertical) and L_{H2} (horizontal). A value of $\psi = 0.1$ (*i.e.* 90% confidence) is chosen due to practical limitations on the sizes of images that can typically be obtained either experimentally or by simulation.

For all synthetic microstructure conditions resulting from the permutations of the factors in Table 3.5.1, the MSAAF technique and its directional counterpart were used to assess the influence of these factors on L_H , L_{H1} and L_{H2} . Since the synthetic microstructure images are periodic, multiple instantiations of the same microstructure were sampled (by re-centering the image) to characterize the inherent variation in the isotropic and directional MSAAF techniques. To this end, 30 distinct instantiations of the same synthetic microstructure were used to calculate error values (three standard deviations) at each length scale considered in the MSAAF analysis, as also depicted by the error bars in Figure 3.5.4.

Results and discussion

Isotropic and directional MSAAF results

The isotropic homogeneous length scale, $L_H(0.01)$, for different area fractions and aspect ratios of aligned particles (90° orientation distribution) is depicted in Figure 3.5.5. First, as expected from previous work [14], there is a general decrease in L_H with increasing second phase area fraction. Second, there is seemingly no monotonic correlation between $L_H(0.01)$ and aspect ratio. Strongly contributing to this absence of correlation is the broad variation in $L_H(0.01)$ between different instantiations of each microstructure that often overlaps with adjacent conditions.

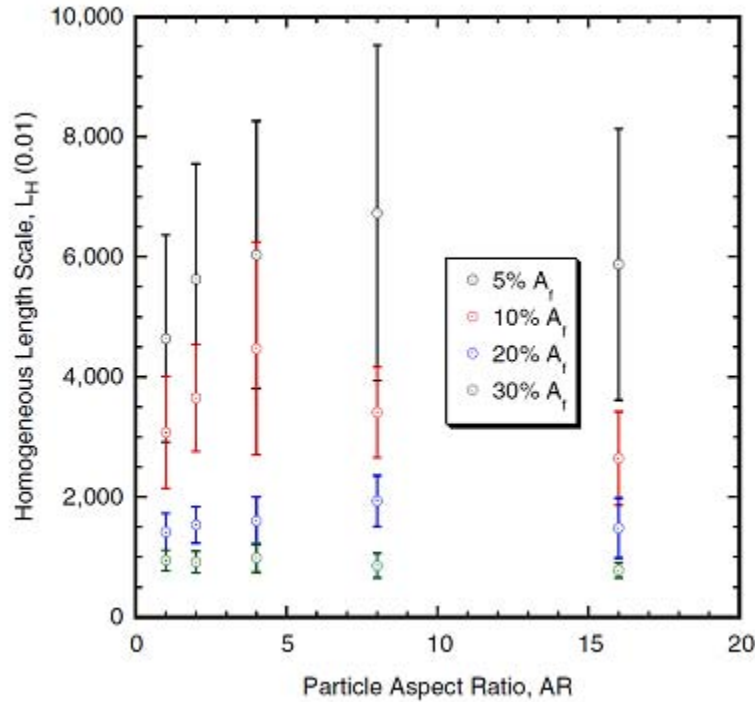


Figure 3.5.5. Isotropic homogeneous length scale, $L_H(0.01)$, as a function of second phase aspect ratio and area fraction for aligned (90° orientation distribution) particles; error bars represent the 3σ deviation from 30 instantiations of each condition.

Directional homogeneous length scales $L_{H1}(0.1)$ and $L_{H2}(0.1)$ for the aligned microstructures (90° orientation distributions) are depicted in Figures 3.5.6(a) and (b), respectively. Here, trends with both area fraction and aspect ratio are apparent. Again, the inverse relationship between homogeneous length scale and area fraction is clear. However, the directional length scale along the axis of alignment (L_{H1}) increases with aspect ratio while the opposite trend is observed in the transverse (L_{H2}) direction.

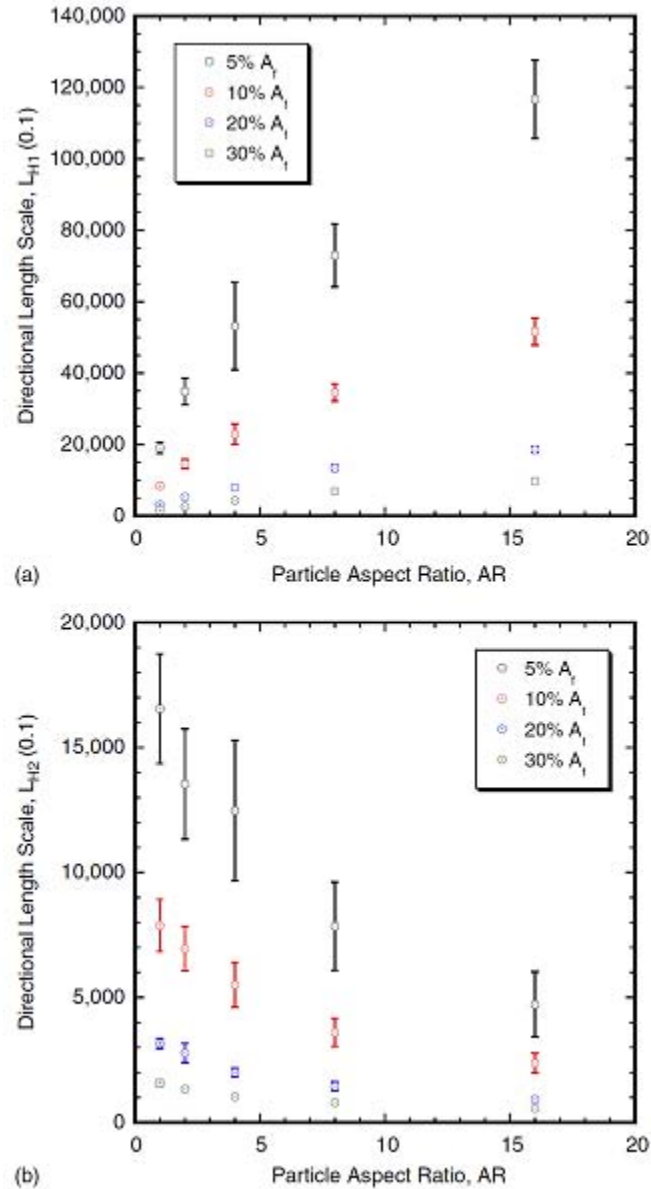


Figure 3.5.6. Directional homogeneous length scales, (a) $L_{H1}(0.1)$ and (b) $L_{H2}(0.1)$, as a function of second phase aspect ratio and area fraction for aligned (90° orientation distribution) particles.

Comparing Figures 3.5.5 and 6 clearly indicates that for the isotropic MSAAF technique, error in L_H measurement can be significant when comparing orthotropic microstructures. This is due in part to the $(m - 1)$ character of the standard deviation in area fraction used to compute \bar{L} , where m is the number of sub-regions; at large length scales, this deviation can influence the measurement of L_H . In contrast, the variation at each length scale resulting from the directional MSAAF technique is quite small since even at the largest length scale there are still 4096 sub-regions; the different length scales more accurately capture the contribution of orthotropy in the microstructure. For this reason, the coefficient of variation terms that used only 1 or 4 sub-regions were dropped when calculating the isotropic L_H to avoid including spurious values of L_H .

The effect of orientation distribution on the directional homogeneous length scales as a function of aspect ratio for the synthetic microstructures containing 30% A_f second phase is captured in Figure 3.5.7. As expected, there is no difference in directional length scales for the random condition. However, the increasing propensity for second phase alignment increases the separation of these orthogonal length scales by increasing L_{H1} and decreasing L_{H2} . This trend is characteristic of the other second phase area fractions as well.

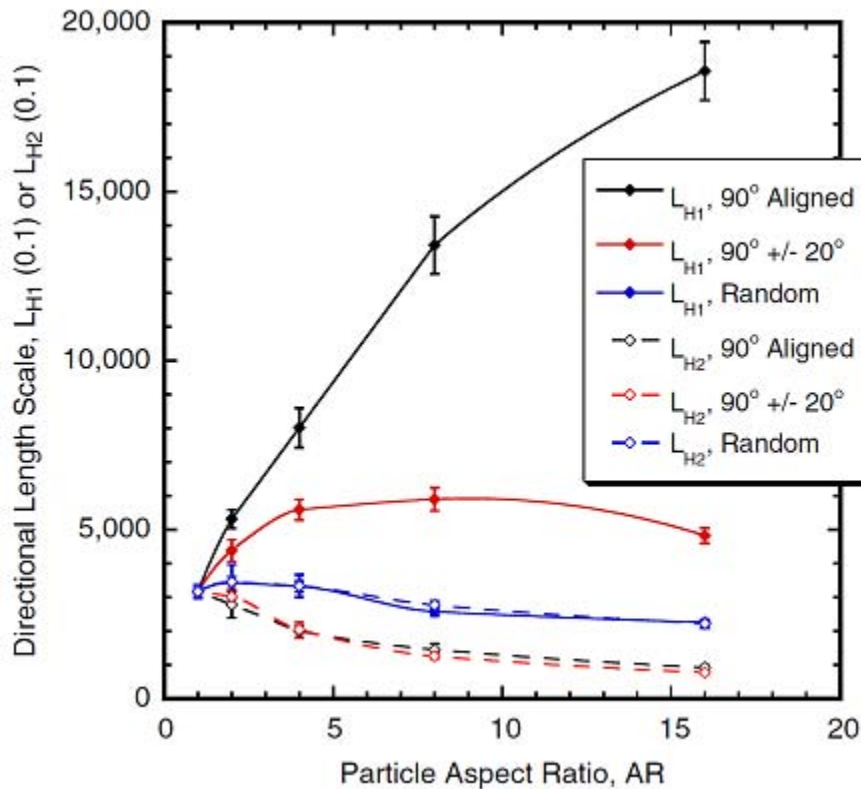


Figure 3.5.7. Directional homogeneous length scales, $L_{H1}(0.1)$ and $L_{H2}(0.1)$, as a function of second phase aspect ratio for random, semi-aligned and aligned (90° orientation distribution) particles in a 30% A_f microstructure.

Model for homogeneous length scales in orthotropic microstructure

MSAAF data have previously been fit [1] to an equation of the form

$$\psi(A_f) = \frac{1}{\sqrt{A_f / (1 - A_f) + \alpha Q^{*-2\xi}}} \quad (1)$$

where α is a geometric factor related to particle size and area fraction, ξ is the slope of the long length-scale portion of the MSAAF plot and Q^* is the discretized length scale (in pixels) [1]. In order to understand the effect of microstructure factors on homogeneous length scales, least squares fits to Equation (1) were used to characterize the behavior of α and ξ for each synthetic microstructure condition. During such fits, it was observed that while $Q^* = Q$ fits MSAAF curves where α is small, large α values require $Q^* = Q-1$. This is simply due to the discretized nature of the image, *i.e.* the lower limit on Q is 1 pixel. This modification reflects that at a length scale of $Q = 1$, the coefficient of variation is entirely dependent on second phase area fraction (*i.e.*, $\psi(A_f) = \sqrt{(1 - A_f) / A_f}$). Use of this transformation for any α fully reconciles the short and long length-scale MSAAF behaviors originally proposed by Spowart *et al* [1] and greatly improves the fit of Equation (1) to MSAAF results, suggesting that the relationship

$$\psi(A_f) = \frac{1}{\sqrt{A_f / (1 - A_f) + \alpha (Q - 1)^{-2\xi}}} \quad (2)$$

is more universal for discrete data than Equation (1), particularly at short length scales.

The solid lines for the directional MSAAF plots shown in Figure 3.5.4 are typical of fitting Equation (2) to MSAAF results for all synthetic microstructure. Over all conditions $\xi_{\text{isotropic}} \approx -1$ and $\xi_{\text{directional}} \approx -0.5$, indicating that ξ is insensitive to all considered microstructure factors, as well as the method (isotropic or directional) used for characterizing homogeneity. On the other hand, α varied significantly with second phase area fraction, aspect ratio and degree of alignment. Moreover, it has previously been shown [1, 11] that ξ can vary significantly with degree of clustering, although this was not studied in the present effort. Figure 3.5.8 shows the evolution of α as a function of second phase area fraction and aspect ratio for the (a) random orientation distribution and the ‘perfectly’ aligned orientation distribution in the (b) L_{H1} and (c) L_{H2} directions.

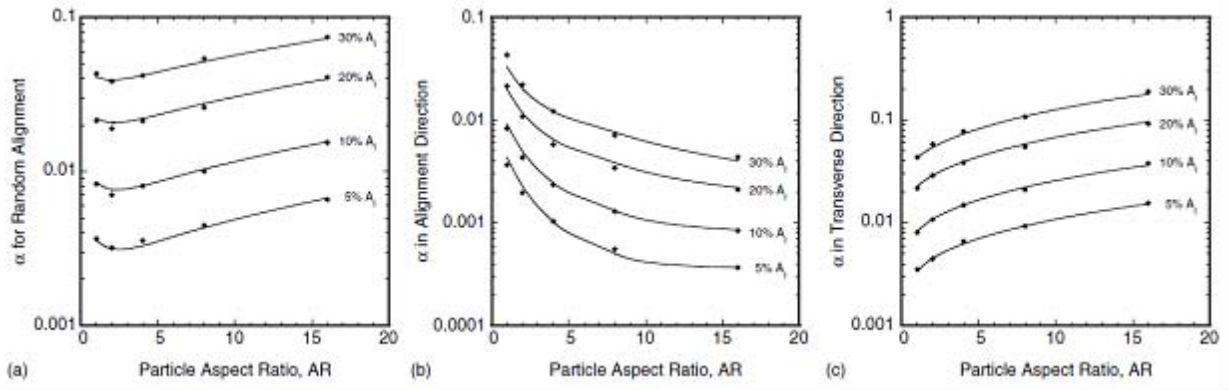


Figure 3.5.8. Evolution of the parameter α as a function of second phase area fraction and aspect ratio for (a) random and ‘perfectly’ aligned (90°) orientation distributions in the (b) $L_{H1}(0.1)$ and (c) $L_{H2}(0.1)$ directions.

Inspecting the results for the random, partially aligned ($90^\circ \pm 20^\circ$) and ‘perfectly’ aligned (90°) conditions showed that α obeys a relationship of the form

$$\alpha = A_f \left[c_0 + c_1 A_f + c_2 A_f AR + c_3 AR + c_4 \frac{1}{AR} \right] \quad (3)$$

where c_n are constants that are tabulated in Table 3.5.2 for each orientation distribution considered in this study. The quality of the fit from these coefficients to the calculated α values is depicted in Figures 3.5.8(a)–(c) by the solid lines.

Table 3.5.2. Coefficients for the model of Equation (3) for each directional homogeneous length scale, (a) L_{H1} and (b) L_{H2} as a function of second phase aspect ratio and area fraction for aligned (90° orientation distribution) particles.

Orientation	c_0	c_1	c_2	c_3	c_4
Random, L_{H1}	0.0201	0.2491	0.0117	0.0056	0.0327
Random, L_{H2}	0.0190	0.2682	0.0096	0.0058	0.0303
$90^\circ \pm 20^\circ$ Aligned, L_{H1}	−0.0049	0.1613	−0.0010	0.0024	0.0733
$90^\circ \pm 20^\circ$ Transverse, L_{H2}	0.0512	0.2267	0.0569	0.0090	−0.0066
90° Aligned, L_{H1}	−0.0091	0.0983	−0.0046	0.0006	0.0895
90° Transverse, L_{H2}	0.0583	0.2488	0.0570	0.0119	−0.0183

Implications for RVEs size in orthotropic materials

If it is assumed that $\zeta = -0.5$, then Equation (2) can be rearranged such that L_H , L_{H1} and L_{H2} can be characterized by a relationship of the form

$$L_{Hn}^\psi = \frac{1}{\alpha} \left[\frac{1}{\psi^2} - \frac{A_f}{1 - A_f} \right] + 1 \cong \frac{1}{\alpha} \left[\frac{1}{\psi^2} - \frac{A_f}{1 - A_f} \right] \quad (4)$$

where the index n of Equation (4) is 1, 2 or 3 depending on the principal direction in the microstructure. Such an expression can then be used to estimate the size of a RVE for the considered orthotropic microstructures as a function of the second phase volume fraction (V_f), aspect ratio, and desired level of confidence (ψ), *i.e.*

$$V_{RVE}^\psi = L_{H1}^\psi L_{H2}^\psi L_{H3}^\psi = \frac{1}{\alpha_1 \alpha_2 \alpha_3} \left[\frac{1}{\psi^2} - \frac{V_f}{1 - V_f} \right]^3 \quad (5)$$

If symmetry is maintained about the axis of alignment (the 1 direction) and the second phase is needle-shaped not disc-shaped, then $\alpha_2 = \alpha_3$ and the size of the RVE necessary to characterize the three-dimensional variants of the orthotropic microstructures can be determined as a function of the factors considered in this work. To that end, Figures 3.5.9(a)–(c) capture the effect of second phase volume fraction and aspect ratio on RVE size for the (a) random, (b) $90^\circ \pm 20^\circ$ and (c) ‘perfectly’ (90°) aligned orientation distributions.

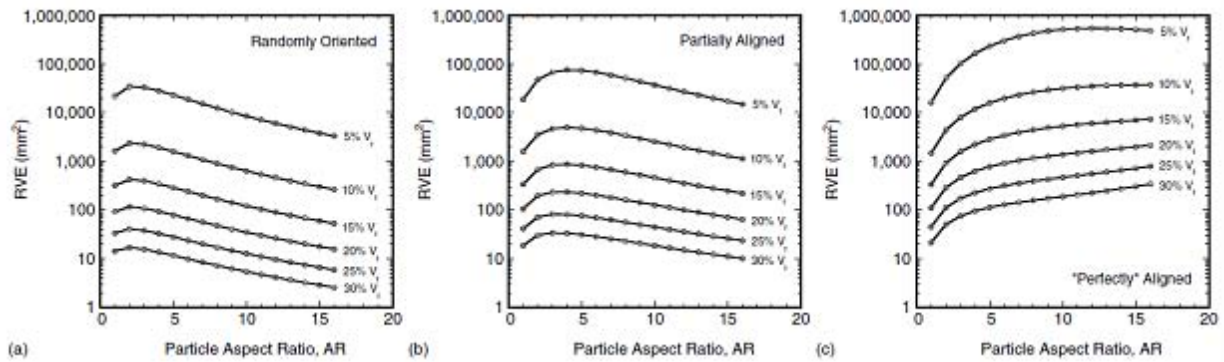


Figure 3.5.9. Effect of second phase area volume fraction (V_f) and aspect ratio (AR) on two-dimensional RVE size for the (a) random, (b) $90^\circ \pm 20^\circ$ and (c) ‘perfectly’ (90°) aligned orientation distributions.

Discussion

There are a few caveats of the 2D synthetic microstructures generated in this work. The random placement of particles may not be entirely representative of extrusion or directional synthesis processing. For example, the nearest neighbor separation could contract during extrusion in addition to second phase alignment or there could be alignment of second phase centroids in addition to the orientation of the principal axis. In this respect, the methodology for generating synthetic microstructures could be altered to better represent the microstructure within a specific material processed in a specific manner, *i.e.* two-point correlation functions of experimental microstructures could be used to generate statistically similar synthetic microstructures [24–30]. Additionally, there are many aspects of microstructures in real materials that have not been explored in the current work, *i.e.* particle morphology (in addition to aspect ratio), particle size distribution and particle clustering (spatial distribution), to name a few. We leave these microstructure-specific aspects of second phase particles for future work.

Nevertheless, by controlling the second phase particle alignment, aspect ratio, and area fraction when generating the 2D periodic synthetic microstructures, the following work illuminates how the computationally efficient MSAAF technique can be used for understanding the inherent alignment of second phase particles in *experimental* images. The two microstructure parameters, α and ξ , used for fitting Equation (2) represent the evolution of the variation in area fraction as a function of length scale. The directional and homogeneous length scales from the MSAAF technique signify a quantitative metric for characterizing the representative length scale or volume element for a given microstructure. The significance of this work is that the analysis of experimental images with the MSAAF technique can be compared and interpreted based on the results of various synthetic microstructures examined in this work.

Future work will encompass generating 3D periodic synthetic microstructures with second phase particles of known sizes, aspect ratios, and orientations; analyzing 2D orthogonal slices may help our understanding of how quantitative information informed from 2D orthogonal slices relate to the known 3D structure. This will test the validity of stereological assumptions often employed for relating 2D microstructural information 3D volumes [31]. Additional work will concentrate on generating synthetic microstructures with various degrees of particle clustering to improve our understanding of how clustering impacts the representative length scales of realistic microstructures. Also, as shown in this work, the directional length scale indicates alignment (or non-alignment) in a particular direction; by applying the directional MSAAF technique along multiple orientations, the associated alignment texture of second phase particles within a microstructure image can be easily ascertained.

Summary

In this work, synthetic two-phase microstructures with known area fractions, aspect ratios and orientations of second phase particles were generated to probe the effects of orthotropy on metrics used to measure representative length scales: the isotropic and directional homogeneous length scales calculated from the MSAAF technique. The prime result of this work is a template

for determining the representative length scale (and volume) of microstructure in a given 2D section as a function of specific microstructure factors (area fraction, aspect ratio, alignment propensity). Ancillary results of this work are:

- (i) The calculated standard deviation (error) from 30 instantiations of each periodic synthetic microstructure is substantially lower for directional homogeneous length scales when compared with the isotropic homogeneous length scale. This is attributable to the number of constituent subdivisions of an image at larger length scales. Therefore, to avoid this deviation the extent of the domain must be large compared with the representative length scale being measured; this is especially important for the isotropic MSAAF technique.
- (ii) The directional MSAAF technique is useful for characterizing the relative alignment of second phase particles in the synthetic microstructures generated. The deviation between the directional length scales in two orthogonal directions increases as a function of particle alignment and aspect ratio. The homogeneous and directional length scales increase with decreasing area fraction of particles.

This work shows how the isotropic and directional MSAAF techniques can help quantitatively characterize orthotropic microstructures with second phase particles of varying alignments.

References

- [1] Spowart J E, Maruyama B and Miracle D B 2001 Multi-scale characterization of spatially heterogeneous systems: implications for discontinuously reinforced metal–matrix composite microstructures *Mater. Sci. Eng. A* **307** 51–66
- [2] Borbely A, Kenesei P and Biermann H 2006 Estimation of the effective properties of particle-reinforced metal matrix composites from microtomographic reconstructions *Acta Mater.* **54** 2735–44
- [3] Lu B and Torquato S 1990 Local volume fraction fluctuations in heterogeneous media *J. Chem. Phys.* **93** 3452–9
- [4] Quintanilla J and Torquato S 1997 Local volume fraction fluctuations in random media *J. Chem. Phys.* **106** 2741–51
- [5] Li M, Ghosh S, Richmond O, Weiland H and Rouns T N 1999 Three dimensional characterization and modeling of particle reinforced metal matrix composites: Pt I. Quantitative description of microstructural morphology *Mater. Sci. Eng. A* **265** 153–73
- [6] Li M, Ghosh S, Richmond O, Weiland H and Rouns T N 1999 Three dimensional characterization and modeling of particle reinforced metal matrix composites: II. Damage characterization *Mater. Sci. Eng. A* **266** 221–40
- [7] Louis P and Gokhale A M 1996 Computer simulation of spatial arrangement and connectivity of particles in three-dimensional microstructure: application to model electrical conductivity of polymer matrix composite *Acta Mater.* **44** 1519–28
- [8] Shan Z and Gokhale A M 2002 Representative volume element for non-uniform microstructure *Comput. Mater. Sci.* **24** 361–79
- [9] Ghosh S, Valiveti DM, Harris S J and Boileau J 2006 A domain partitioning based pre-processor for multi-scale modelling of cast aluminium alloys *Modelling Simul. Mater. Sci. Eng.* **14** 1363–96

- [10] Valiveti DM and Ghosh S 2007 Morphology based domain partitioning of multi-phase materials: a preprocessor for multi-scale modelling *Int. J. Numer. Meth. Eng.* **69** 1717–54
- [11] Spowart J E 2006 Microstructural characterization and modeling of discontinuously-reinforced aluminum composites *Mater. Sci. Eng. A* **425** 225–37
- [12] Faber K and Evans A 1983 Crack deflection process: I. Theory *Acta Metall.* **31** 565–76
- [13] Faber K and Evans A 1983 Crack deflection process: II. Experiment *Acta Metall.* **31** 577–84
- [14] Wilks G B 2007 Influence of reinforcement homogeneity on the deformation and fracture of a discontinuously reinforced aluminum matrix composite *PhD Thesis* Pennsylvania State University
- [15] Kumar H, Briant C L and Curtin W A 2006 Using microstructure reconstruction to model mechanical behavior in complex microstructures *Mech. Mater.* **38** 818–32
- [16] Ghosh S, Bai J and Raghavan P 2007 Concurrent multi-level model for damage evolution in microstructurally debonded composites *Mech. Mater.* **39** 241–66
- [17] Yang S and Gokhale A M 1999 Application of image processing for simulation of mechanical response of multi-length scale microstructures of engineering alloys *Metall. Mater. Trans. A* **30** 2369–81
- [18] Shan Z and Gokhale A M 2001 Micromechanics of complex three-dimensional microstructures *Acta Mater.* **49** 2001–15
- [19] Ayyar A and Chawla N 2006 Microstructure-based modeling of crack growth in particle reinforced composites *Compos. Sci. Technol.* **66** 1980–94
- [20] Tewari A, Gokhale A M, Spowart J E and Miracle D B 2004 Quantitative characterization of spatial clustering in three-dimensional microstructures using two-point correlation functions *Acta Mater.* **52** 307–19
- [21] Cadilhe A, Araujo N A M and Privman V 2007 Random sequential adsorption: from continuum to lattice and pre-patterned substrates *J. Phys.: Condens. Matter* **19** 065124
- [22] Buryachenko VA, Pagano NJ, Kim RY and Spowart J E 2003 Quantitative description and numerical simulation of random microstructures of composites and their effective elastic moduli *Int. J. Solids Struct.* **40** 47–72
- [23] Hinrichsen E L, Feder J and Jossang T 1986 Geometry of random sequential adsorption *J. Stat. Phys.* **44** 793–822
- [24] Singh H, Gokhale A M, Mao Y and Spowart J E 2006 Computer simulations of realistic microstructures of discontinuously reinforced aluminum alloy (DRA) composites *Acta Mater.* **54** 2131–43
- [25] Singh H, Mao Y, Sreeranganathan A and Gokhale A M 2006 Application of digital image processing for implementation of complex realistic particle shapes/morphologies in computer simulated heterogeneous microstructures *Modelling Simul. Mater. Sci. Eng.* **14** 351–63
- [26] Sheehan N and Torquato S 2001 Generating microstructures with specified correlation functions *J. Appl. Phys.* **89** 53–60
- [27] Yeong C L Y and Torquato S 1998 Reconstructing random media *Phys. Rev. E* **57** 495–506
- [28] Yeong C L Y and Torquato S 1998 Reconstructing random media: II. Three-dimensional media from two-dimensional cuts *Phys. Rev. E* **58** 224–33
- [29] JiaoY, Stillinger FHand Torquato S 2007 Modeling heterogeneous materials via two-point correlation functions: basic principles *Phys. Rev. E* **76** 031110
- [30] JiaoY, Stillinger FHand Torquato S 2008 Modeling heterogeneous materials via two-point correlation functions: II. Algorithmic details and applications *Phys. Rev. E* **77** 031135
- [31] Underwood E E 1970 *Quantitative Stereology* (Reading, MA: Addison-Wesley)

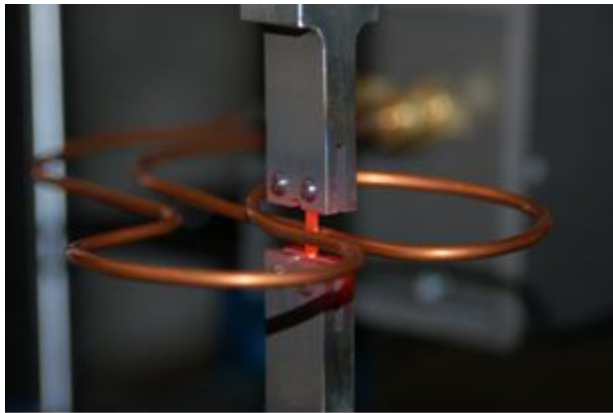
3.6. Setup of a miniature specimen apparatus

The motivation for this work is that the smaller section thicknesses in turbine blades may cause different creep properties than test specimens machined from thicker slabs. This requires a test apparatus that can perform creep and fatigue experiments at temperatures up to 1200°C. A number of subtasks need to be performed to setup a test machine capable of testing miniature specimens.

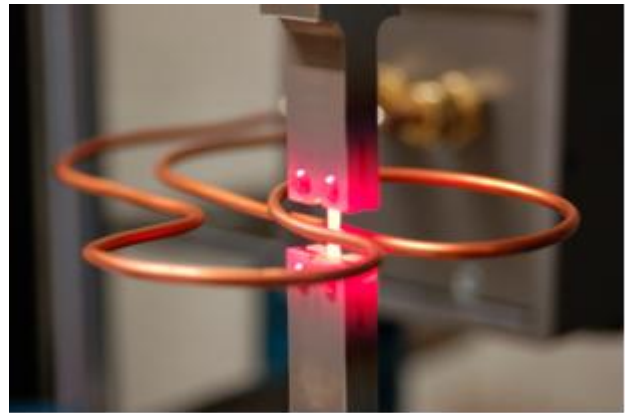
Completed Subtasks

1. Initial setup
 - a. Hydraulic lines were installed for the final location of the apparatus.
 - b. The MTS 858 Material Testing System with MTS Model 359 load unit was ordered for this particular set of experiments. A table with anti-vibration pads for the legs was used to support the test apparatus.
2. Specimen grips
 - a. **Grips.** Grips were machined from a Ni-based superalloy material.
 - b. **Pins.** The specimen will be pin loaded with two pins on both ends. The pins may be exposed to high temperatures as well, so these were also machined from a Ni-based superalloy material.
 - c. **Grip cooling.** A copper block was machined to cool the grips with cooling water. The block is in two halves and can be adjusted to attach to the grips at any location.
3. Machine alignment
 - a. **Instrumented alignment specimen.** Aluminum alignment specimen with a longer and wider gauge section was machined. The width of this specimen was increased to accommodate a sufficient number of strain gauges. The length of the specimen was increased following finite element modeling of the alignment specimen design. Small strain gauges were attached to an alignment specimen.
 - b. **Anti-rotation device.** An anti-rotation device was machined and attached to the MTS machine prior to alignment. This device attaches to a precision machined rod and the actuator. The device is locked to the actuator, but is allowed to slide along the rod, keeping the actuator from any lateral movements or rotations that would adversely affect alignment.
4. Temperature Measurement/Control
 - a. **Heating Unit.** The Ameritherm HotShot (2kW) induction heating unit is being used with a coil design complemented by a flux concentrator. A stage with x-y translation has also been attached to the induction heating unit to allow for repeatable positioning of the induction coils with respect to the specimen.
 - b. **Heating Unit Coil.** A butterfly coil design with 3/16" OD copper tubing and the flux concentrator material locally heated the specimen to >1200°C while the grip material stayed at ~500°C.

- c. **Pyrometer.** A one-color pyrometer is currently being used for temperature measurement of the specimens during coil design.
 - d. **Temperature calibration.** S-type thermocouples were welded to a test specimen to measure the temperature profile across the gage length. Minor fluctuations in temperature (on the order of 5-25°C across the gage length) within the hot zone of the induction coil still need to be fixed.
 - e. **Temperature feedback loop.** The one-color pyrometer was linked with process controller for controlling the temperature output of the induction heating unit. A process controller that accepts, controls, and retransmits a 4-20 mA signal was installed. The loop works well, but relies on the temperature from the pyrometer being the correct temperature.
5. Strain Measurement/Control
- a. **Non-contact interferometry.** Dantec Dynamics was contacted about an on-site demonstration of their Q-300 speckle pattern interferometer on our test apparatus. This would allow non-contact measurement of the 3-dimensional strains on a sample area of 1x1 mm² and larger. Unfortunately, following a full-field displacement meeting on Feb 28th, it was decided that the capability of Dantec's systems and other "state of the art" image correlation systems isn't sufficient for our specimen size and the high temperatures.
 - b. **Extensometers.** High temperature extensometers can contact the specimen from the side for strain measurement. The current butterfly design of the coils creates an unobstructed face for the extensometer to contact the gage section of the specimen. The LVDT extensometers need to be calibrated.
6. Stress Measurement
- a. **Load cell.** The load cell for the unit was calibrated.
7. Specimen preparation.
- a. **Bulk slab specimens.** The miniature specimens for testing were machined from a bulk slab that was oriented such that the [001] dendritic growth direction is along the length of the specimen and the lateral faces of the specimen are the [010] and [100] directions. The directions were measured using the Laue x-ray with the help of Jay Tiley and Paul Shade.



(a)



(b)

Figure 3.6.1. Images of the butterfly coil design locally heating the test specimen. Figure 3.6.1(b) shows that while this coil design heats the specimen efficiently, it also heats the grips over time.

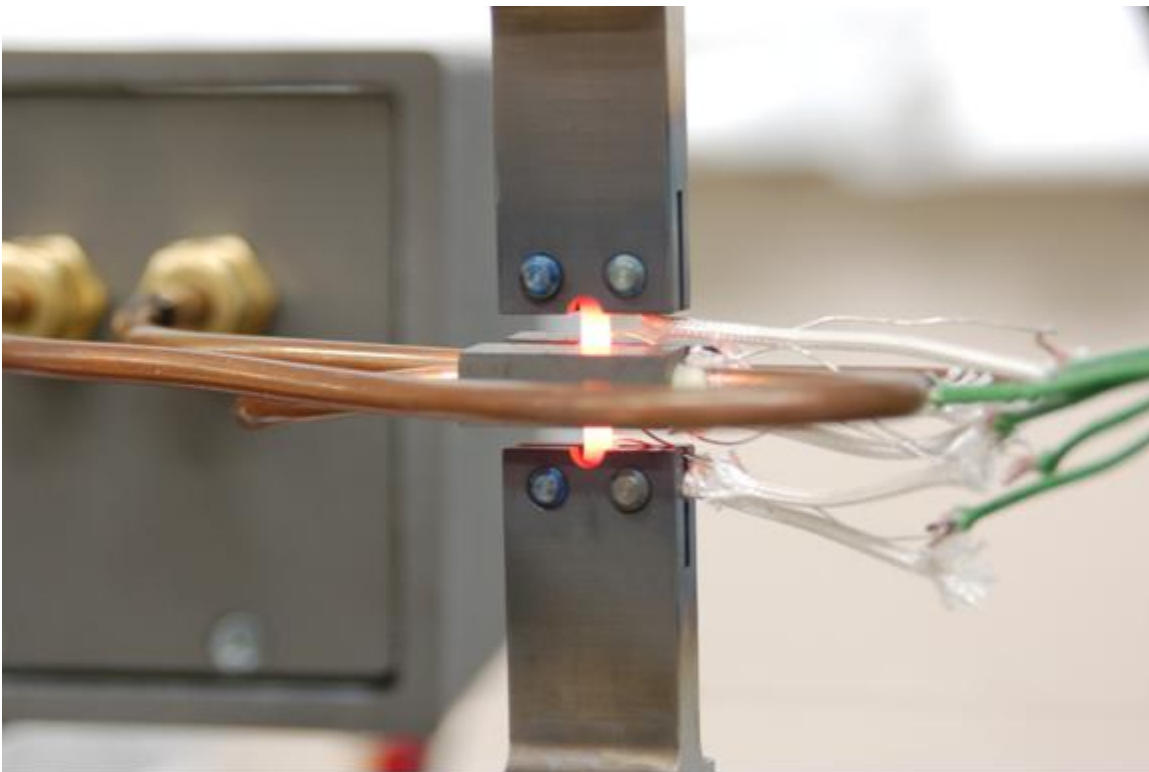


Figure 3.6.2. Images of the butterfly coil design with the flux concentrator locally heating a test specimen with five thermocouples instrumented along the gage section.

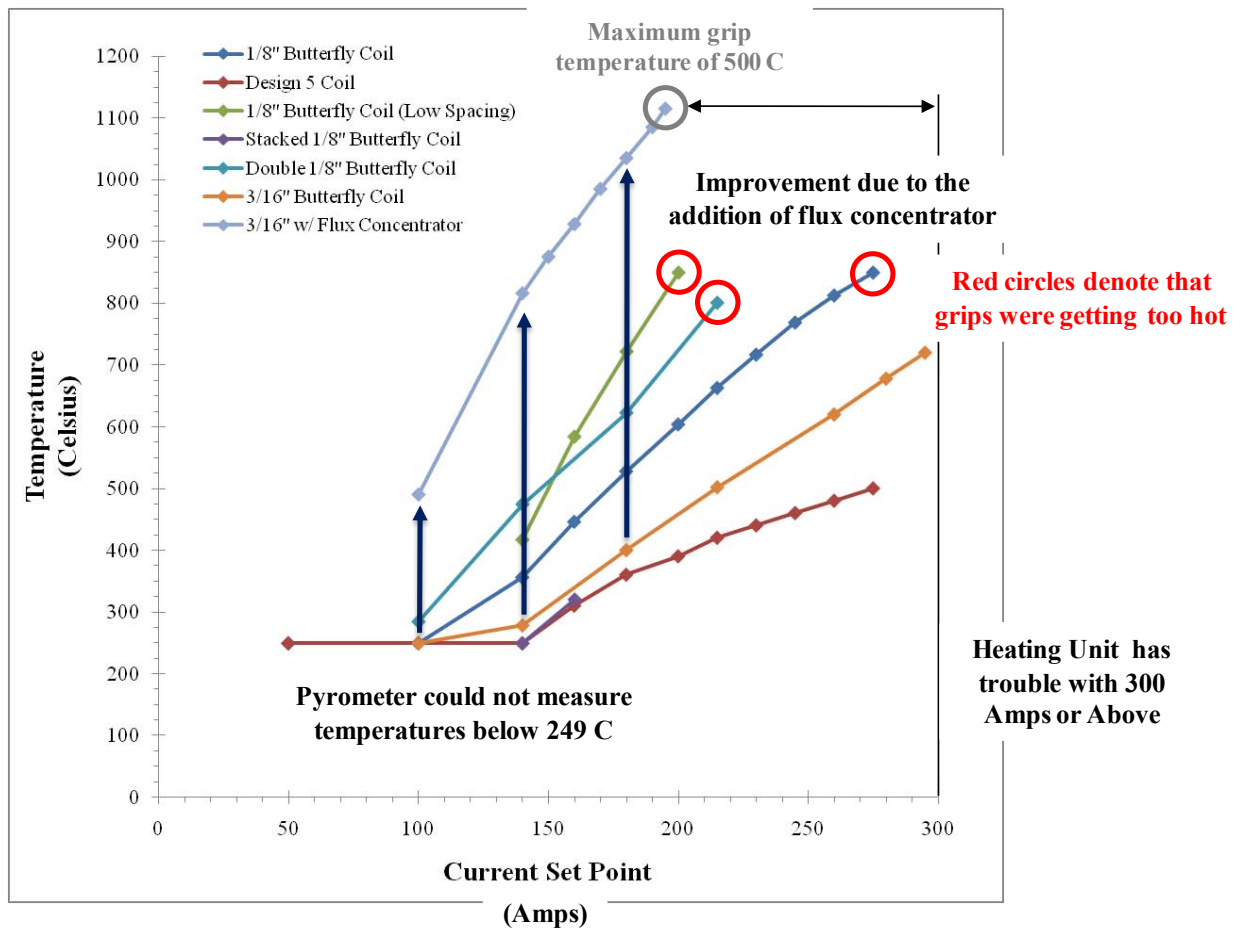


Figure 3.6.3. Graph showing a comparison of various coil designs. The biggest increase in performance was due to the addition of the flux concentrator to the coil.

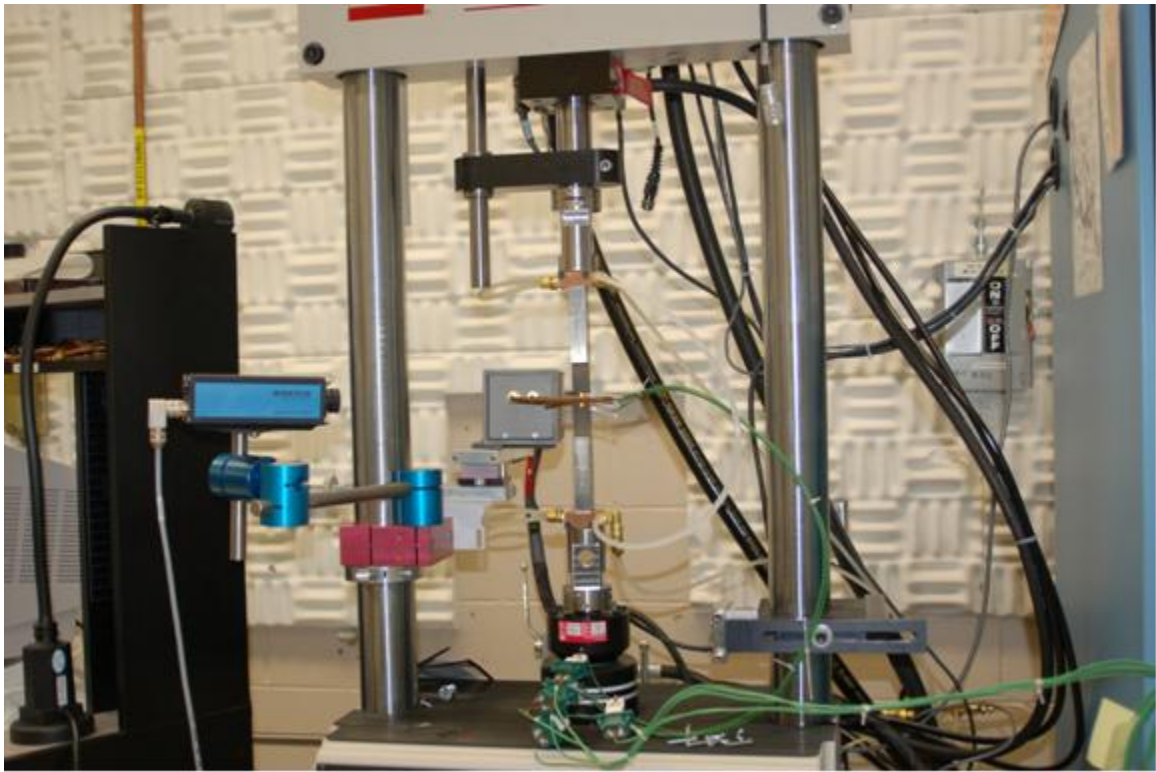


Figure 3.6.4. Images of the miniature test apparatus with one-color pyrometer (left, blue), induction heating unit and coils, grips, anti-rotation device, and copper cooling blocks for the grips. In the lower right hand side, the brackets for the extensometer is also visible.

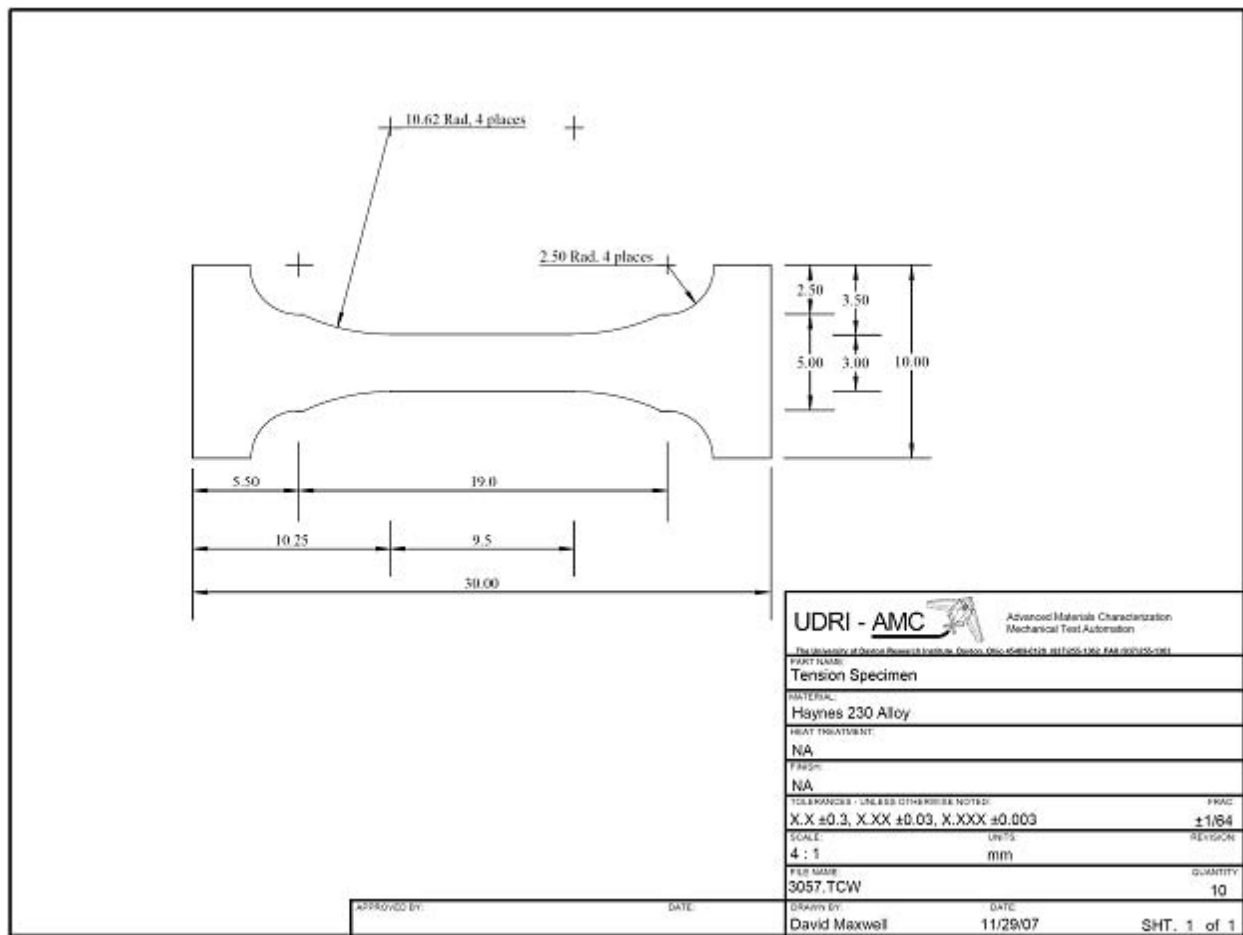


Figure 3.6.5. CAD drawing for the final specimen design (David Maxwell).

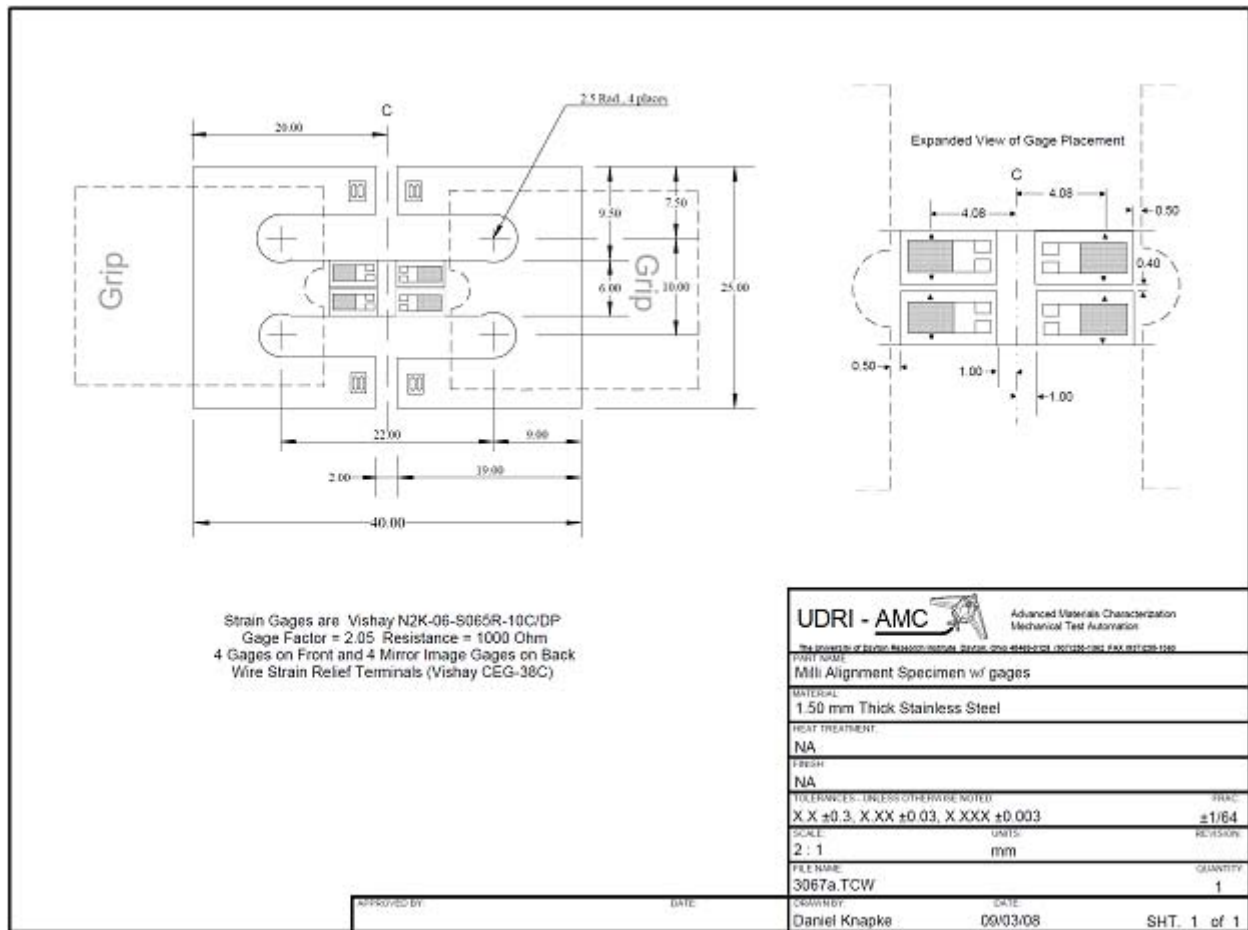


Figure 3.6.6. CAD drawing for the placement of the strain gauges on the alignment specimen (Daniel Knapke).

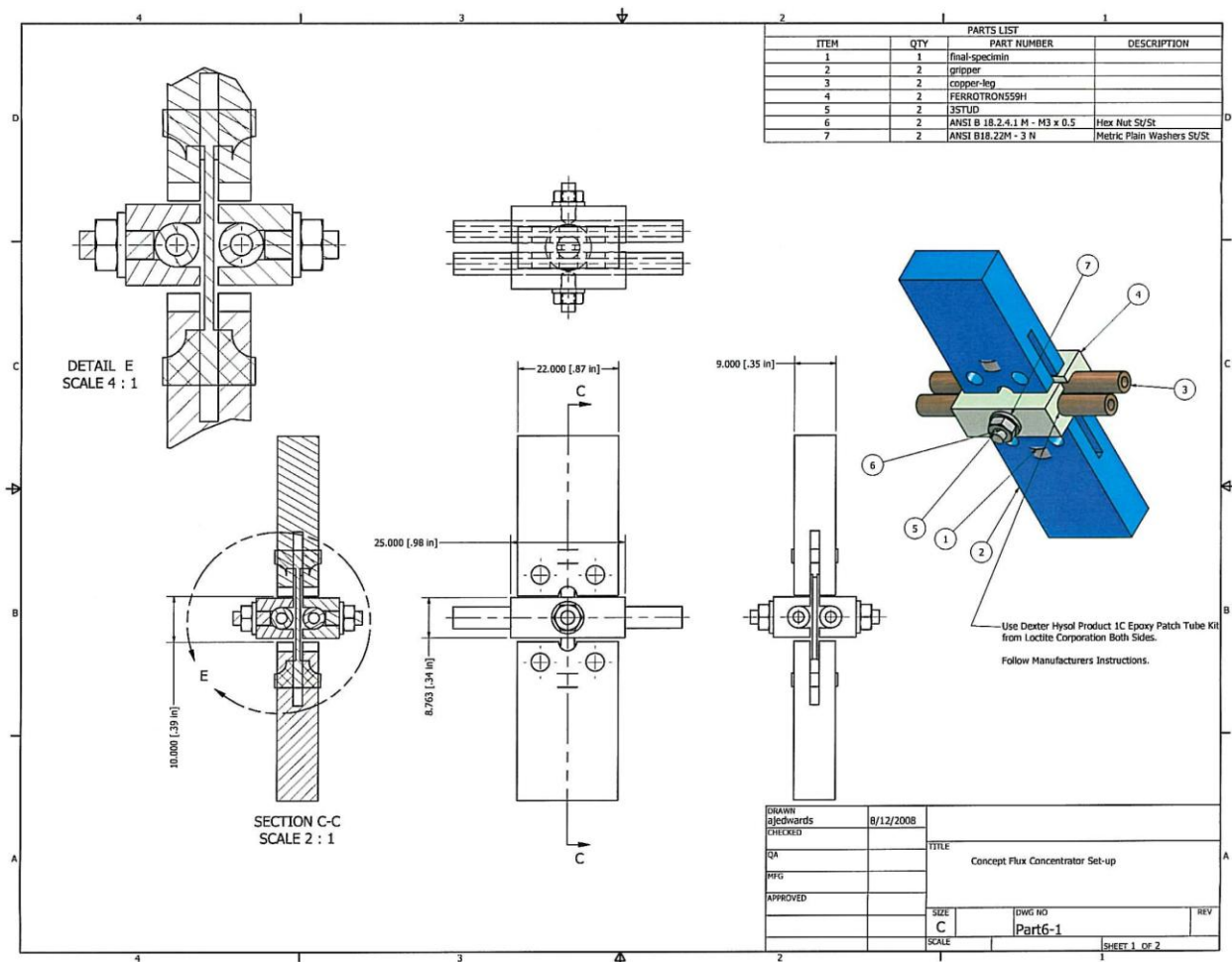


Figure 3.6.7. CAD drawing for the flux concentrator (Fluxtrol).

4 Conclusions

This report focuses on two research areas critical to better understanding high temperature mechanical behavior in single crystal nickel-based superalloys, which are commonly used materials for turbine blades that lie within the hot section (1200°C) of the engine. The first research area detailed in this report was the high temperature mechanical properties (creep, fatigue) of single crystal nickel-based superalloys. The second research area detailed in this report was the detection and characterization of microstructural features that may be important for models that aim to describe how damage progresses in single crystal Ni-based superalloys. The ability to use the information stemming from these research areas in concurrent multiscale damage mechanics models may greatly enhance the engineering of single crystal Ni-based superalloys.